ELSEVIER

Recent progress in phosphorus based anode materials for lithium/sodium ion batteries

Weili Liu, Hanqian Zhi, Xuebin Yu*

Department of Materials Science, Fudan University, Shanghai 200433, China

A B S T R A C T

Phosphorus has aroused growing concern as a promising anode material for both lithium and sodium ion batteries, owning to its high theoretical capacity and appropriately low redox potential. However, the poor electronic conductivity and large volume expansion of phosphorus during cycling lead to low electrochemical activity and unstable cyclability, which limits its practical application. Recently, various nanostructured phosphorus based anodes, which efficiently restrained the pulverization and supplied faster reaction kinetics, have been developed to solve these issues. This review aims to summarize the major progress of nanostructured phosphorus based electrode materials for lithium/sodium ion batteries. We first examine the most widely-used design strategy of compositing phosphorus with various carbon materials, ranging from 0D particles, 1D tubes or fibers, 2D sheets to 3D frameworks. And then, the progress of various metal phosphides and their composites is discussed, which mainly include Sn-P phosphides, Ni-P phosphides, Cu-P phosphides, Fe-P phosphides, Co-P phosphides, etc., and their composites. This is followed by a comparison of different compositing methods, which involve in preparing phosphorus-carbon composites and nanostructured metal phosphides or their composites. Finally, the challenges and perspectives regarding the phosphorus based anode materials are proposed.

1. Introduction

Energy issues have attracted great attentions during the past decade due to growing energy demand, exhausting refined fossil fuels and serious environmental issues caused by their usage. Various new and clean energy sources, i.e., solar, wind, hydro, tidal, and geothermal energies, are emerging rapidly. Therefore, a large-scale energy storage system is urgently required to store these renewable energies into the electrical grid to realize the peak shift. Lithium ion batteries (LIBs) have been presenting great promise, due to their fascinating characteristics, such as high energy conversion efficiency, stable cyclability, simple maintenance, adaptable power and energy features for different grid functions [1].

LIBs have been extensively used as the common power sources in the market of portable electronics since Sony realized their first commercial launch in early 1990s [2–4]. LIB technology has been experiencing great progress and commercialization in mid-size applications such as hybrid electric vehicles (HEVs) and electric vehicles (EVs) applications. Moreover, lots of grid-scale LIBs prototypes (approximately tens of megawatt-hours), used for storing renewable energy sources, have emerged on the market [5–7]. However, the growing cost of LIBs due to the finite lithium resources ($\approx 0.0065\%$ as shown in Fig. 1a) would ultimately fail to satisfy the ever-increasing industrial demand, especially for HEVs, EVs, and large-scale renewable energy storage [8–10].

Alternatively, sodium ion batteries (NIBs) have attracted great attentions with the ever-growing demand for advanced rechargeable batteries, assigned to the abundance of sodium resources ($\approx 2.74\%$ as shown in Fig. 1a). Theoretically speaking, Na is heavier than Li, and NIBs may have a lower energy density than LIBs. However, the energy penalty is small because sodium has a suitable potential of -2.71 V (vs SHE). Therefore NIBs are much more suitable to a large grid stationary application, where the low cost and long cycle life of the batteries are more important for a whole system [11].

The electrochemical properties of the electrode materials are vital to the important performance characteristics of battery such as specific capacity and operation voltage. Therefore, the major challenge in advancing LIB and NIB technology lies in finding good electrode materials. However, the specific capacities of most cathode materials are low and it is difficult to greatly increase their specific capacities. The application of cathode materials with high redox potentials is also limited by the electrolyte which decomposes at high potentials.

---

a

b

Capacity(mAh/g)

c

Capacity(mAh/g)
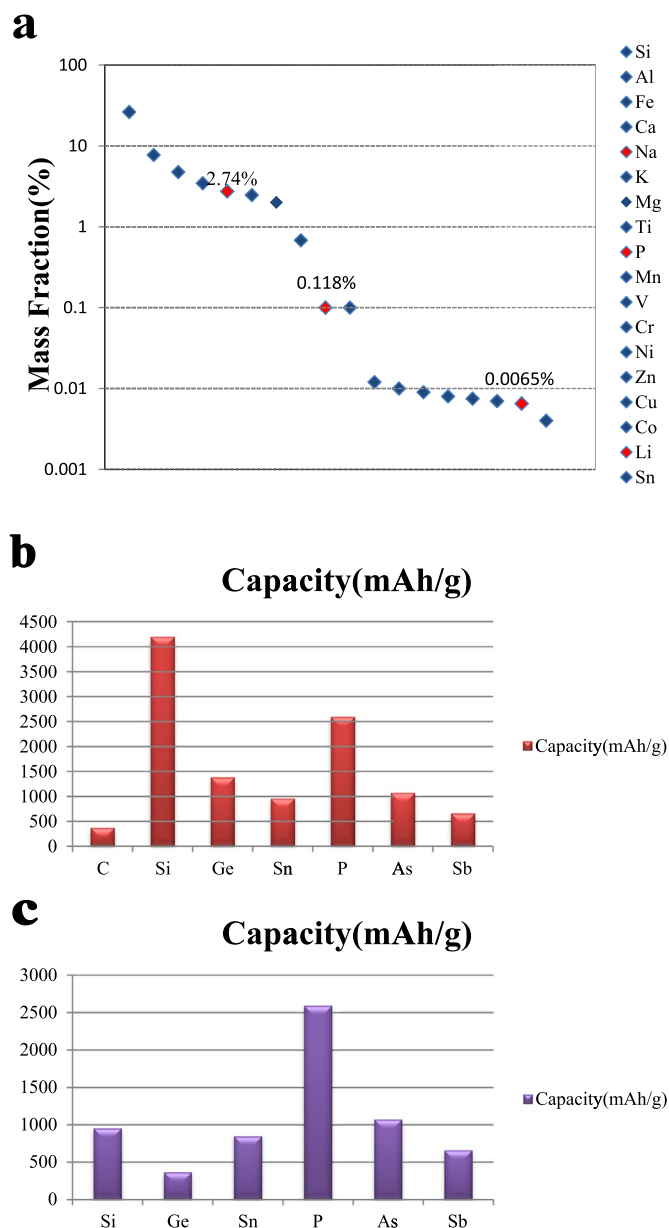
Fig. 1. (a) Elemental abundance in the earth's crust. (b) Theoretical specific capacity of the C, Si, Ge, Sn, P, As and Sb elements for LIBs; (c) Theoretical specific capacity of the Si, Ge, Sn, P, As and Sb elements for NIBs.

Therefore, it is a desiring approach to develop anode materials which own high specific capacities and relatively low redox potentials. Using conversion chemistry such as alloying materials is one of most used strategy for storing a large number of ions. Si-based material is the representative example, for which 4.4 Li can react with one Si to form Li-Si alloy, providing the highest theoretical specific capacity of 4200 mA h/g among LIB anode materials (Fig. 1**b**) [12–15]. However, for NIBs, it can store only one Na per Si, delivering a theoretical specific capacity of 954 mA h/g [16–18]. While phosphorus can not only react electrochemically with lithium to form Li_3P, but also store three Na at attractive potentials with a high theoretical specific capacity of 2596 mAh/g, which significantly exceeds that of any other NIB anode presently available (Fig. 1**c**) [19–30]. In addition, phosphorus has the advantages of low cost, abundance ($\approx 0.118\%$ in Fig. 1**a**) and easy availability, which provide great potential for its practical applications for LIBs and NIBs.

In this review, we will present the recent advances in phosphorus based anodes for LIBs/NIBs, with a focus on phosphorus carbon composites and metal phosphides or their composites. This article covers the development of new promising phosphorus based anodes for LIBs/NIBs, lithium-storage mechanisms of metal phosphides and many efforts to enhance the electrochemical performance of phosphorus based anodes. In addition, methods for the synthesis of phosphorus-carbon composites and metal phosphides or their composites are summarized. Finally, the challenges and opportunities for the phosphorus based anodes of LIBs/NIBs are suggested.

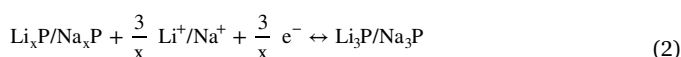## 2. Phosphorus based anodes for LIBs/NIBs

As an element of the fifth group in the periodic table, phosphorus possesses four main allotropes: white phosphorus, red phosphorus, violet phosphorus and black phosphorus (Fig. 2**a**) [31]. White phosphorus is volatile and toxic, and it bursts into flames if exposed to the natural atmosphere, enabling it unsuitable for electrode materials. Violet phosphorus has been rarely investigated in the past decades. However, its 2D layered violet phosphorene has drawn increasing research interest recently [32,33]. Alternatively, red phosphorus and black phosphorus have been studied commonly as the anode materials because they are chemically stable at room temperature and atmosphere. Red phosphorus is commercially available with ease, but its low conductivity ($\sim 10^{-14}$ S/cm) results in poor reversibility of electrochemical reaction. Crystalline black phosphorus as anode materials shows substantially improved reversibility relative to red phosphorus (Fig. 2**b**) [19]. However, due to the nature of poor electronic conductivity of phosphorus, there is a far way between its experimental capacity and theoretical value. It has been demonstrated that the conductivity of phosphorus based electrode can be improved by doping red phosphorus with iodine, and the electrodes for LIBs exhibited much higher specific capacity (1868 mA h/g at the second cycle) and much longer cycling life (1562 mA h/g at 520 mA/g after 150 cycles) than that of red phosphorus, even than black phosphorus Fig. 2**c**) [34]. However, the electrochemical performance of most phosphorus based electrodes has been improved by forming different type of phosphorus carbon composites and metal phosphides or their composites as discussed in the following sections.

2.1. Phosphorus carbon composites

The intrinsic outstanding conductivity and diversity in architecture of carbon material make it the most popular material preferred for phosphorus based anodes. Various strategies have been developed to realize a perfect compositing between phosphorus and carbon materials. Carbon materials can be summed as particles, e.g., carbon black and graphite [19,25,31,35–41]; one-dimensional materials, e.g., nanotubes and nanofibers [42–49]; two-dimensional materials, e.g., graphene and reduced graphene oxide [53–64]; and three-dimensional materials, e.g., aerogels and mesoporous carbon [65–70,74]. In this section we will give a summary of the recent progress in phosphorus carbon composites.

2.1.1. Lithium/sodium-storage mechanism

The general reactions of phosphorus carbon composites with lithium/sodium are summarized as follows:

$$P + xLi^+/Na^+ + xe^- \leftrightarrow Li_xP/Na_xP \tag{1}$$

$$Li_xP/Na_xP + \frac{3}{x}\, Li^+/Na^+ + \frac{3}{x}\, e^- \leftrightarrow Li_3P/Na_3P \tag{2}$$

During lithiation/sodiation process, phosphorus reacts with lithium/sodium to form the compounds of Li_xP/Na_xP, with the final products of Li_3P/Na_3P. The delithiation/desodiation process involves a stepwise lithium/sodium ion extraction from the fully lithiated/sodiatied Li_3P/Na_3P, corresponding to several plateaus in voltage profile, as well as the several cathodic peaks in the cyclic voltammogram.
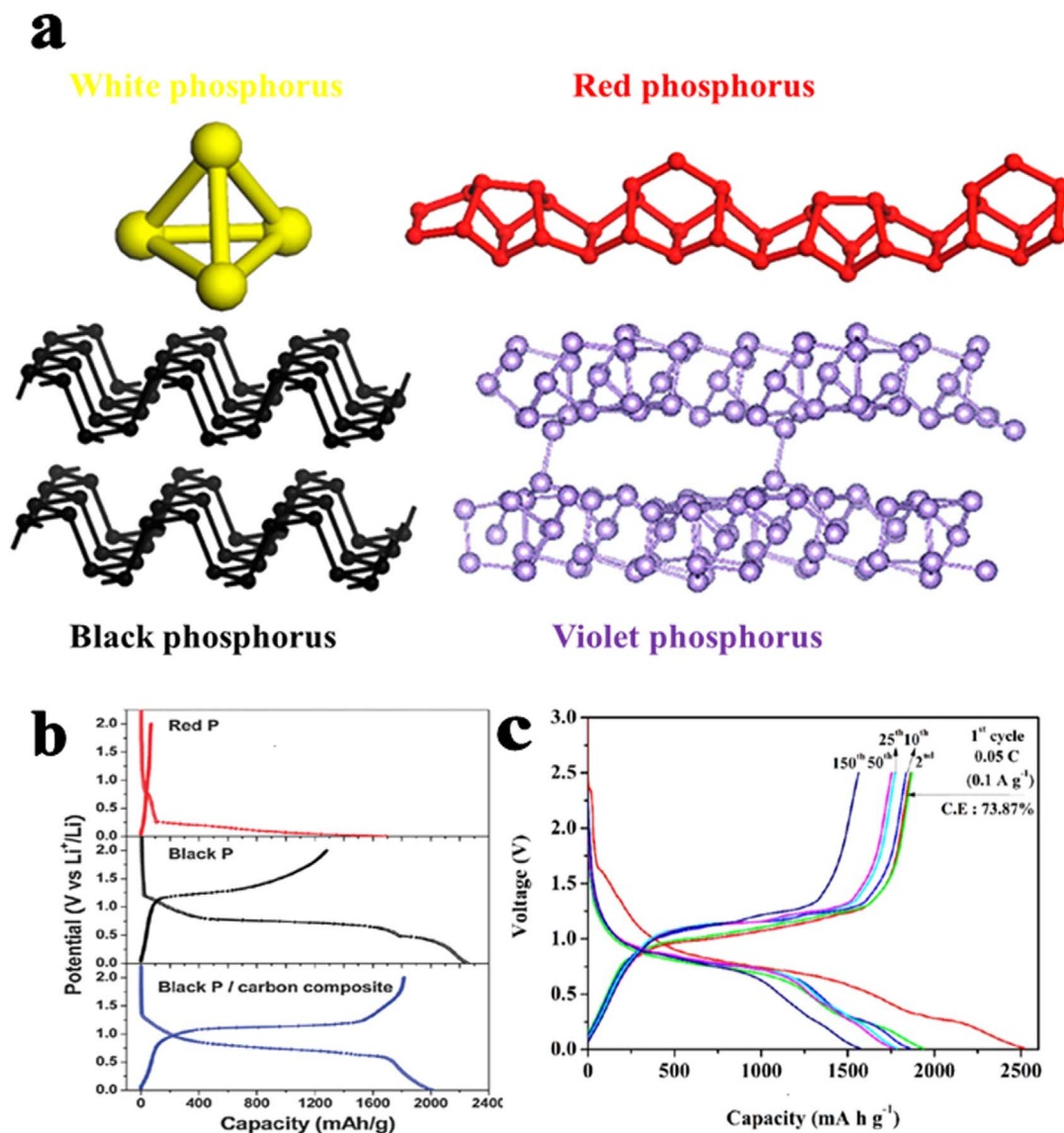
Fig. 2. (a) Schematics of white, red, violet and black phosphorus. (Reproduced with permission. Copyright 2014, American Chemical Society [31]) (b) Electrochemical behaviors of various types of phosphorus. (Reproduced with permission. Copyright 2007, Wiley-VCH Verlag GmbH & Co. KGaA [19]) (c) Voltage profiles of Iodine doped red phosphorus nanoparticles at a rate of 0.2 C between 0.01 and 2.5 V. (Reproduced with permission. Copyright 2017, American Chemical Society [34]).

2.1.2. Particle carbon materials

Park and Sohn first composited black phosphorus with carbon black (Super P), used as an anode material for LIBs in 2007 through a high-energy mechanical milling method [19]. The composite displayed enhanced electrochemical discharge/charge performance with a high initial Coulombic efficiency (90%) (Fig. 2b) and good cycle performance (600 mA h/g after 100 cycles between 0.78 and 2.0 V). To further improve the electrochemical performance of phosphorus, Qian et al. prepared an amorphous phosphorus/carbon nanocomposite (a-P/C) through ball-milling red phosphorus with conductive carbon black powders and found that the amorphous phosphorus can fully store reversible 3-Li storage capacity (2355 mA h/g) with stable cyclability (2119.5 mA h/g after 100 cycles) and high rate capability (Fig. 3a & b) [33]. Later, Sun et al. found that phosphorus-carbon (P-C) bonds could be formed by mechanochemical reaction, and the P-C bonds maintained stable during cycling, ensuring that phosphorus could keep well contact with carbon (Fig. 3c). Due to the stable P-C bonds, the composite delivered a high initial discharge capacity of 2786 mA h/g at 520 mA/g and an excellent cycle life (80% capacity retention over 100 cycles) (Fig. 3d) [31]. Recently, phosphorus was

also studied as an anode for NIBs. Qian et al. demonstrated that by compositing amorphous phosphorus with carbon materials, a capacity of 1750 mA h/g at a current density of 250 mA/g was delivered at room temperature (Fig. 3e) [36]. Simultaneously, Kim et al. estimated that a capacity of 1890 mA h/g at a current density of 143 mA/g could be provided at a slightly elevated temperature of 30 °C for amorphous red phosphorus-carbon composite (Fig. 3f) [25].

2.1.3. One-dimensional carbon materials

Owning to the high aspect ratios, one-dimensional carbon nanotubes are able to form interconnected networks between phosphorus and impart long-range conductivity to phosphorus anode materials (Fig. 4a). The phosphorus-carbon nanotube composite was initially studied as lithium/sodium anode materials by Dou and co-workers, who simply hand-grinded commercial red phosphorus (P) with multi-walled carbon nanotubes (MWCNTs). The P-MWCNT composite delivered a surprisingly high initial charge capacity of 1530 mA h/g at the current density of 143 mA/g (Fig. 4b) [42]. However, the capacity of the P-MWCNT composite dropped quickly to 750 mA h/g after only 20 cycles. The unsatisfactory electrochemical performances of the P-
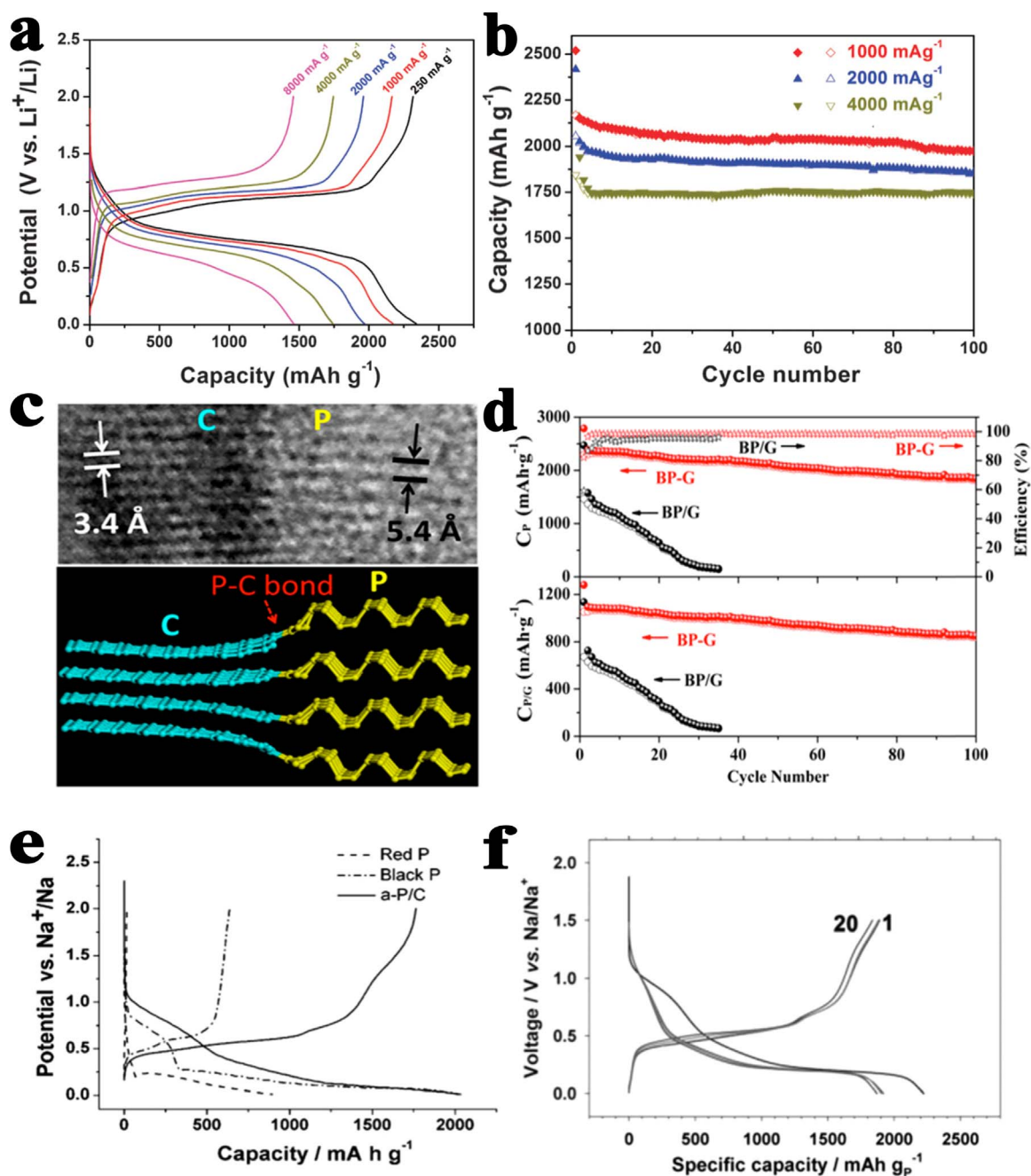
Fig. 3. (a) Charge-discharge profiles and (b) cycling performances at various current densities. (Reproduced with permission. Copyright 2012, The Royal Society of Chemistry [33]) (c) The HRTEM image and schematic of black phosphorus-graphite composite; (d) The cycling performance and Coulombic efficiency of black phosphorus/graphite mixture and black phosphorus-graphite composite electrodes at a current density of 520 mA/g. (Reproduced with permission. Copyright 2014, American Chemical Society [31]) (e) Initial charge/discharge curves of three phases of phosphorus: red phosphorus, black phosphorus, and a-P/C nanocomposites. (Reproduced with permission. Copyright 2013, Wiley-VCH Verlag GmbH & Co. KGaA [36]) (f) Charge-discharge voltage profile of the red phosphorus-carbon composite electrode. (Reproduced with permission. Copyright 2013, Wiley-VCH Verlag GmbH & Co. KGaA [25]).

MWCNT composite above are possibly due to the less contact and weak physical interaction between phosphorus particles and carbon matrix. To create better physical interaction, red phosphorus and tangled single-walled carbon nanotube were heated at 600 °C under vacuum condition in a sealed glass tube, where phosphorus vaporized and diffused into the voids between and in tangled single-walled carbon nanotube bundles. Phosphorus was mainly adsorbed on the outer surface of the carbon nanotubes, with little diffused into the interspaces of the single-walled carbon nanotube bundles, providing more physical contact between the two materials (Fig. 4c). As a result, the phosphorus-carbon nanotube anodes delivered a high discharge capacity of ~ 300 mA h/g$_{composite}$ with 80% capacity retention after 2000 cycles at

2000 mA/g$_{composite}$ (Fig. 4d) [43]. Considering these promising works, further improvement of phosphorus-carbon nanotube (P-CNT) hybrid was conducted through chemical bonding between phosphorus, carbon nanotube, and crosslinked polymer binder formed by facile ball milling (Fig. 4e), and a capacity of 1586.2 mA h/g after 100 cycles at 520 mA/g could be maintained (Fig. 4f) [44].

One-dimensional porous carbon nanofibers could not only form interconnected conductivity networks between phosphorus with a free-standing characteristics, but also effectively buffer the volume change of phosphorus anodes due to its porous structure. This was demonstrated by Li et al., who loaded crystalline red phosphorus into free-standing porous carbon nanofibers with 3D interconnected, flexible
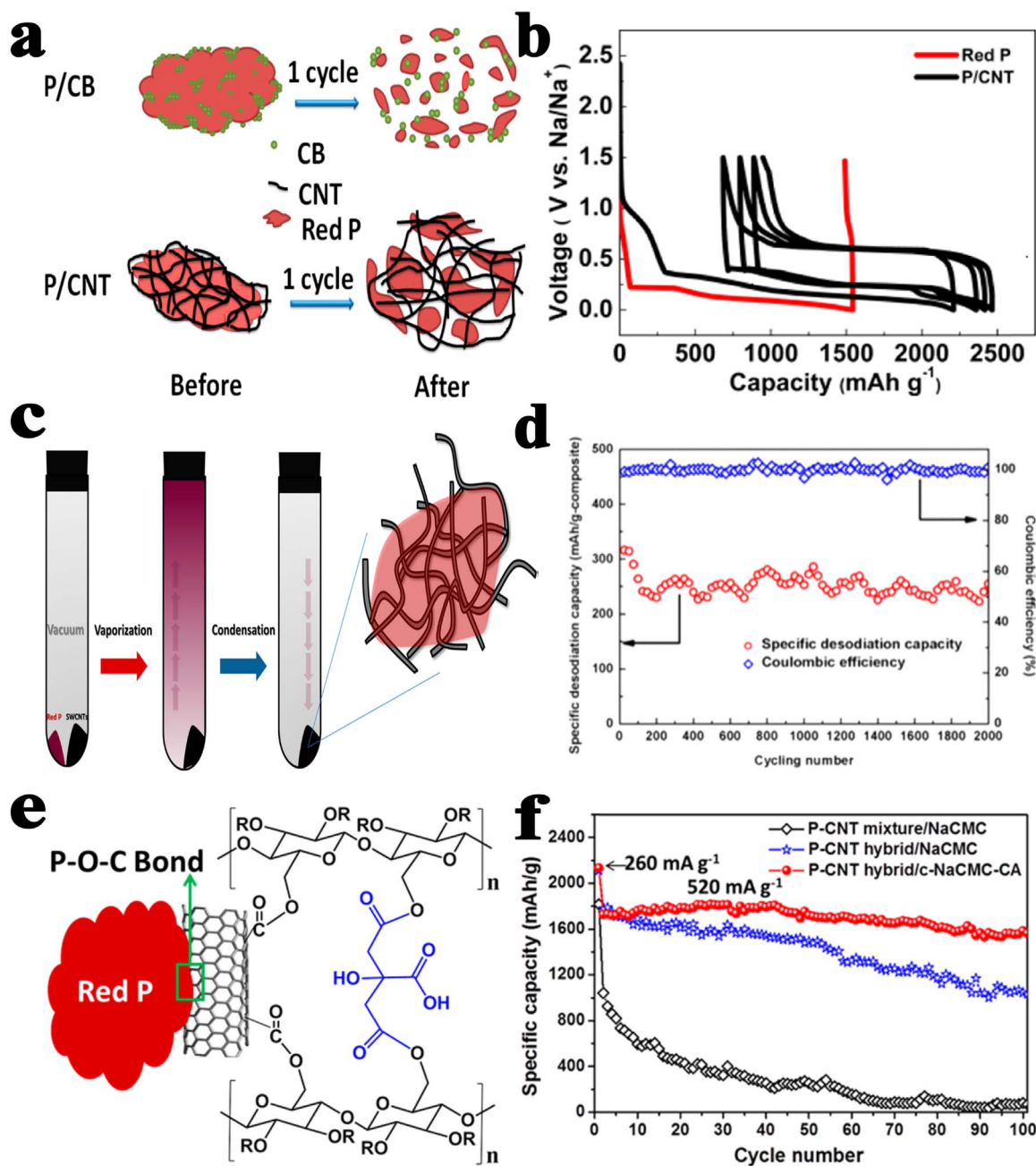
Fig. 4. (a) Proposed functions of carbon nanotubes during the volume expansion; (b) Charge-discharge curves of red phosphorus and phosphorus/carbon nanotubes composite. (Reproduced with permission. Copyright 2013, American Chemical Society [42]) (c) Schematic illustration of the synthesis process for red phosphorus-single-walled carbon nanotubes composite; (d) Cycling performance of red phosphorus-single-walled carbon nanotubes composite at 2000 mA/g$_{composite}$. (Reproduced with permission. Copyright 2015, American Chemical Society [43]) (e) Interaction between phosphorus-carbon nanotubes hybrid and c-NaCMC-CA binder; (f) Cycling stability of the P-CNT mixture/NaCMC, P-CNT hybrid/ NaCMC, and P-CNT hybrid/c-NaCMC-CA electrode at a current density of 260 mA/g for activation and then at 520 mA/g in the subsequent cycles. (Reproduced with permission. Copyright 2015, American Chemical Society [44]).

characteristics (Fig. 5). When used as the additive-free flexible film electrodes, a reversible capacity of 2030 mA h/g and an average Coulombic efficiency of ~ 99.9% over 100 cycles were achieved [48].

Besides the porous carbon nanofibers, N-doped carbon nanofibers are also suitable to improve the performances of phosphorus anodes for LIBs/NIBs, because the nitrogen-containing functional groups on the carbon surface can improve the surface wettability between the electrolyte and the active materials as well as the electronic conductivity. Based on the above advantages, Ruan et al. employed polypyrrole (PPy) precursor as the carbon source to obtain N-doped carbon nanofibers, and further loaded with phosphorus to prepare the phosphorus/N-doped carbon nanofiber composite. The phosphorus/

N-doped carbon nanofiber composite delivered a reversible capacity of 731 mA h/g in NIBs, with capacity retention of 57.3% over 55 cycles [49].

2.1.4. Two-dimensional carbon materials

Graphene, as a typical and the most arresting two-dimensional carbon material, owns high conductivity, surface area (theoretically 2630 m^2/g) and flexibility. These excellent properties enable it a good interfacial contact ability to anchor phosphorus particles very dispersively as a matrix, which can effectively restrain the aggregation of phosphorus particles during volume change [50–52]. Therefore, the composite of graphene and phosphorus is believed to own superior
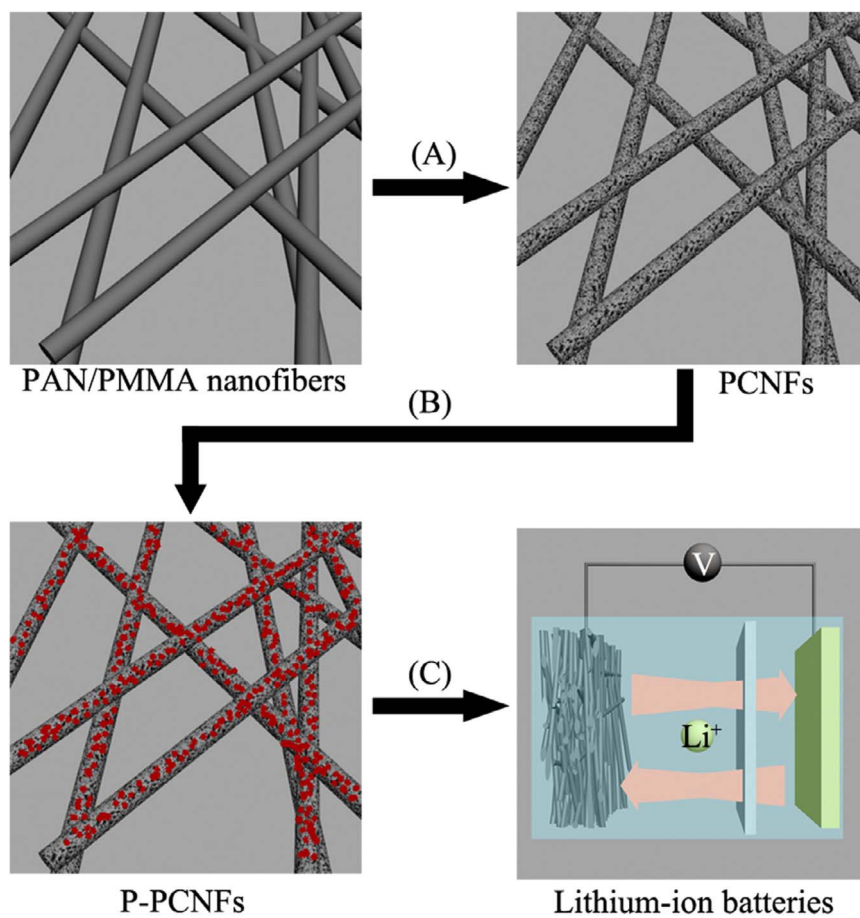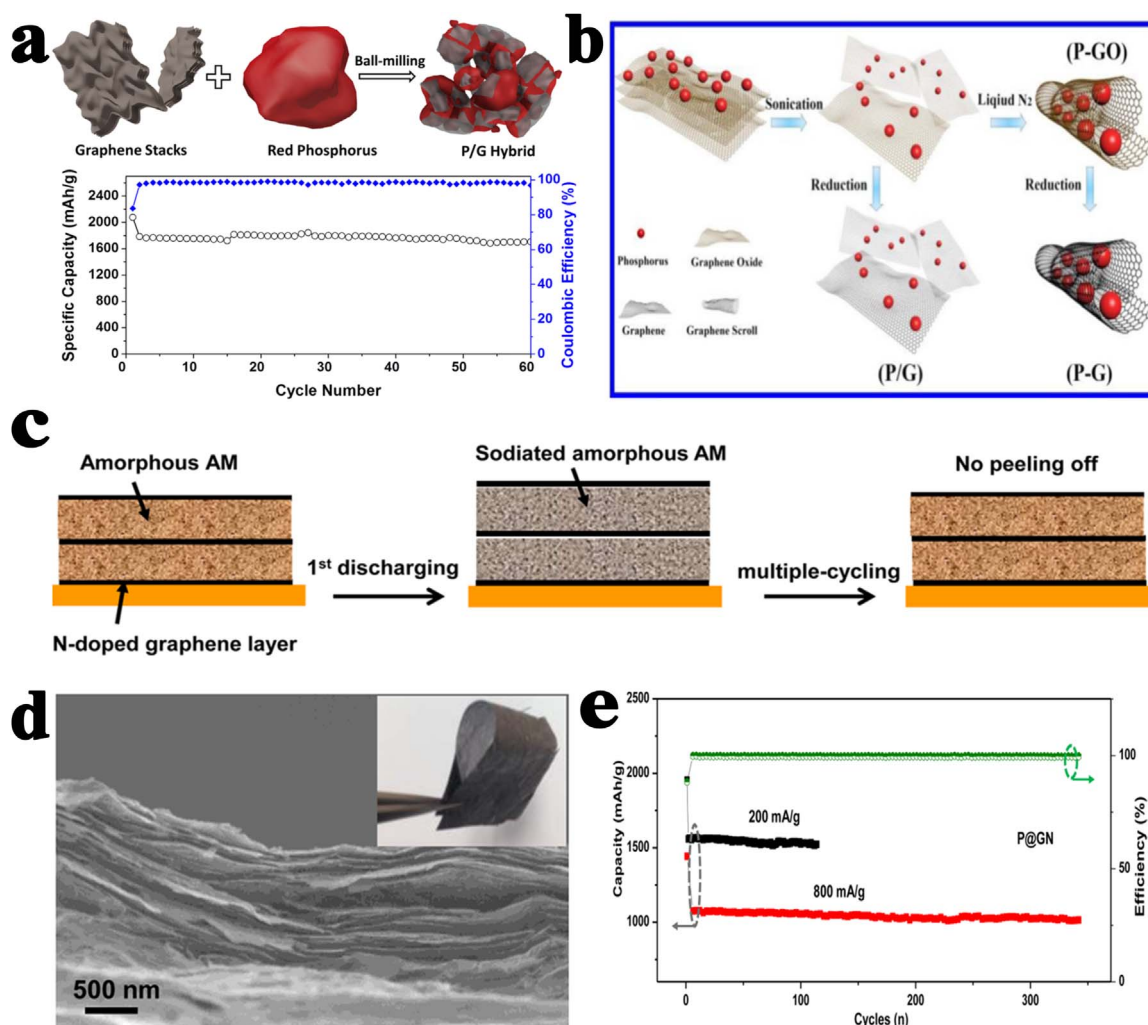
Fig. 5. Schematic illustration of the experimental procedures. (A) Carbonizing electrospun PAN/PMMA bicomponent nanofibers to obtain porous carbon nanofibers (B) Incorporating red phosphorus into the porous carbon nanofibers nanostructure via a vaporization-adsorption-transformation strategy (C) Directly using self supported phosphorus/porous carbon nanofibers working electrodes to assemble lithium-ion batteries and evaluate the electrochemical performance. (Reproduced with permission. Copyright 2014, ScienceDirect [48]).

performance in LIBs/NIBs. Wang and co-workers first employed graphene to composite with phosphorus by ball-milling as NIB anodes. They demonstrated that the graphene served to enhance the overall conductivity and buffer the large volume change of phosphorus during cycling. As a result, the as-synthesized phosphorus/graphene composite presented a high initial capacity of 2077 mA h/g at 260 mA/g and retained 1700 mA h/g after 60 cycles (Fig. 6a) [53]. Further improvement was achieved through a full encapsulation of phosphorus by graphene scrolls. The synthesis was performed via co-freeze-drying phosphorus nanoparticles and graphene oxide (GO) nanosheets and then reduction process (Fig. 6b). Assigned to the graphene scrolls encapsulating phosphorus nanoparticles, the phosphorus-graphene anodes for NIBs showed a high reversible capacity of 2355 mA h/g with high capacity retention of 92.3% after 150 cycles at a current density of 250 mA/g [54]. Later, Zhang et al. redesigned a novel anode structure by fabricating flexible paper made of nitrogen-doped graphene and amorphous phosphorus (Fig. 6c & d). The restructured anode exhibited an ultrastable cyclic performance (0.002% decay per cycle from 2nd to 350th cycle at 800 mA/g) (Fig. 6e) [55].

Phosphorene, namely monolayer or few-layer black phosphorus (BP), has recently attracted great scientific interest for LIBs/NIBs applications. Phosphorene–graphene hybrid, working as an anode for NIBs, has achieved exciting progress. The phosphorene–graphene hybrid material, consisting of a few phosphorene layers sandwiched between graphene layers (Fig. 7a), delivered a specific capacity of 2440 mA h/g at a current density of 50 mA/g with 83% capacity retention after 100 cycles while operating between 0 and 1.5 V (Fig. 7b) [59]. However, there are still some hurdles before phosphorene as anode material can realize commercialization. One representative of the hurdles is the poor air stability of

phosphorene which plagues its electrochemical activities. In addition, some side effects are inevitably induced on exfoliated phosphorene. Finally, its high specific surface area possibly lead to low initial Coulombic efficiency and volumetric capacity due to the low packing efficiency of nanostructures. To deal with these problems, Zhang et al. prepared densely stacked packed phosphorene–graphene composite (PG-SPS, a packing density of 0.6 g/cm^3) via spark plasma sintering (Fig. 7c). When used for LIBs anode, PG-SPS electrode showed a much improved initial Coulombic efficiency of 60.2% than phosphorene (11.5%) and loosely stacked phosphorene-graphene (34.3%) electrodes, which is ascribed to the reduced exposed surface and excellent electrical contact between reduced graphene oxide and BP (Fig. 7d). Moreover, high gravimetric capacity (1306.7 mA h/g$_{composite}$) and volumetric capacity (256.4 mA h/cm^3$_{composite}$) (Fig. 7f), good rate capabilities (415.0 mA h/g$_{composite}$ at 10 A/g$_{composite}$) (Fig. 7e) as well as stable long-term cyclic performance (91.9% retention after 800 cycles at 10 A/g$_{composite}$) were achieved in the PG-SPS electrode (Fig. 7g). Importantly, the PG-SPS achieved excellent air stability (over the 60-days) [60].

Besides the 2D layered structure phosphorene, ultra-small black phosphorus quantum dot (QD) is also favorable for LIBs/NIBs, because its large surface area enable it more active sites and shorter lithium/sodium diffusion distance as well as less mechanical fracture. Pan et al. achieved, for the first time, the uniform distribution of BP QDs on nitrogen-doped graphene (N-graphene) nanosheets in molecular level for superior lithium storage through a facile strategy (Fig. 8). The molecular level distribution of BP QDs on the N-graphene nanosheets effectively prevented their aggregation upon cycling and preserved the whole structure. As a result, superior electrochemical performances (a startlingly high reversible capacity of 1271 mA h/g at 500 mA/g) were presented [64].

Fig. 6. (a) Schematic illustration of the synthesis of phosphorus/graphene nanosheets hybrid and its cycling performance. (Reproduced with permission. Copyright 2014, American Chemical Society [53]) (b) Schematic illustration for the preparation of P-G and P/G composites. (Reproduced with permission. Copyright 2015, Wiley-VCH Verlag GmbH & Co. KGaA [54]) (c) Illustrative scheme of the designed novel "butter-bread"-like anode structure consisting of amorphous phosphorus layer@N-doped graphene frameworks; (d) SEM image of the cross section of a phosphorus@N-doped graphene paper, the inset shows its paperlike appearance; (e) Cyclic performance and Coulombic efficiency of phosphorus@N-doped graphene composite at 200 mA/g and 800 mA/g. (Reproduced with permission. Copyright 2016, American Chemical Society [55]).

2.1.5. Three-dimensional carbon materials

Three-dimensional carbon materials, due to their large porosity and pore volume, are excellent hosts for phosphorus. Volume expansion of phosphorus anodes during cycling can be efficiently buffered by confining phosphorus within their pores with improved cycling stability. Moreover, higher mass loading of phosphorus materials and hence higher areal capacity can be achieved [65–68]. Encapsulating phosphorus in porous carbon matrix is a representative example of a three-dimensional carbon-phosphorus structure. This was first reported by Wang et al., who synthesized nano-structured porous carbon phosphorus composite via vaporization/adsorption strategy for lithium storage. And the composite showed a highly reversible capacity of ~ 750 mA h/$g_{composite}$ at 100 mA/$g_{composite}$, and long cycle life with high Coulombic efficiencies [65]. Then Yu's group confined nanosized amorphous red phosphorus into highly ordered channels of mesoporous carbon matrix, CMK-3 (donated as P@CMK-3) via a vaporization-condensation-conversion strategy. Due to the uniform diameter pores, high pore volume, and excellent conductivity of CMK-3 and benefiting from this unique hybrid nanostructure, P@CMK-3 exhibited superior lithium and sodium storage performance. The P@CMK-3 composite with 31.54 wt% phosphorus displayed a high reversible specific capacity of ~ 2250 mA h/g (~ 971 mA h/g based on the composite) at

650 mA/g and significantly enhanced cyclablility with 1150 mAh/g (500 mAh/g based on the mass of the composite) at 13 A/g after 1000 cycles for LIBs. For NIBs, 1020 mA h/g (370 mA h/g based on the mass of the composite) was maintained after 210 cycles at 13 A/g. Interestingly, the phosphorus content could reach further ~60 wt% with a high specific capacity and stable cycling performance, which is a very promising result [66].

Instead of using mesoporous carbon, the same group prepared a unique microporous carbon-phosphorus composite by confining phosphorus into microporous of ZIF-8-derived N-doped microporous carbon matrix (donated as P@N-MPC) (Fig. 9a). With the small micropores (~ 1 nm), organic electrolyte ions can diffuse faster and the size of the encapsulated red phosphorus particles are smaller. When used as anode for NIBs, the P@N-MPC composite displayed a high reversible specific capacity of ~ 600 mA h/g at 150 mA/g and stable cycling performance (~ 450 mA h/g at 1 A/g after 1000 cycles with a high capacity retention of 80%) [67].

To create more intimately contact between phosphorus particles and the conductive 3D carbon framework, a 3D-structured phosphorus/carbon composite was fabricated starting from P_4O_{10} using a carbothermic reduction method (Fig. 9b), in which ultrafine red phosphorus particles (~ 10 nm) were connected to three-dimensional
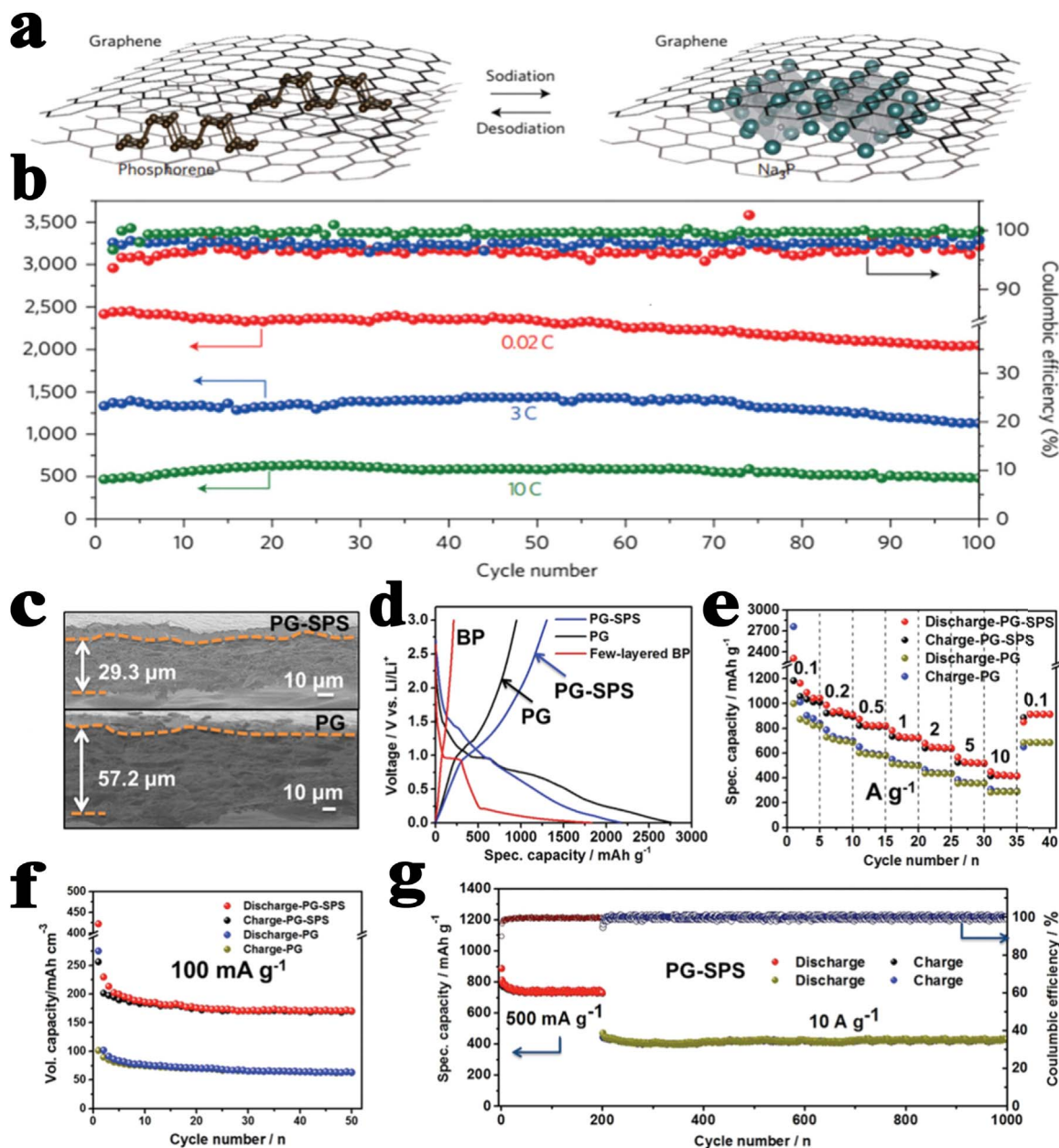
Fig. 7. (a) Structural evolution of the sandwiched phosphorene-graphene structure during sodiation; (b) Cycling performance of phosphorene/graphene composites at different current densities. (Reproduced with permission. Copyright 2015, Nature Publishing Group [59]) (c) Cross-sectional SEM images of PG-SPS and PG electrodes on Cu foil with the same mass loading of 0.65 mg/cm^2; (d) The first galvanic charge/discharge measurements of few layered BP, PG, and PG-SPS at a current density of 100 mA/g$_{composite}$; (e) Rate capabilities of PG and PG-SPS electrodes at various current densities; (f) Cycling life of PG and PG-SPS electrodes based on volumetric capacities at a current density of 100 mA/g$_{composite}$; (g) Long-term cycle life of PG-SPS electrode at high current densities of 500 mA/g$_{composite}$ (200 cycles) and 10 A/g$_{composite}$. (Reproduced with permission. Copyright 2016, Wiley-VCH Verlag GmbH & Co. KGaA [60]).

carbon framework via P-O-C bonds. With the unique structure and strong P-O-C bonds connection, the phosphorus/carbon composite for NIBs delivered a reversible specific capacity of 1027 mA h/g at 520 mA/g with high capacity retention of 88% over 160 cycles [68].

Encapsulating phosphorus in novel three-dimensional porous graphene matrix, graphene aerogel, is another example of three-dimensional carbon-phosphorus structure [71–73]. Guo's group uniformly distributed phosphorus nanoparticles within three-dimensional graphene through a vapor-redistribution approach to fabricate a three-dimensional integrated carbon/red phosphorus/graphene aerogel composite (C@P/GA) (Fig. 9c). The as-prepared C@P/GA electrode showed a high capacity of 1867 mA h/g after 100 cycles at 260 mA/g and achieved a significant capacity of 1095.5 mA h/g, even at 2600 mA/g after 200 cycles [74].

2.2. Metal phosphides

Among the phosphorus based anode materials for LIBs/NIBs, metal phosphides, due to their high specific capacity, appropriately safer operating potential, richness, metallic features and excellent thermal stability, have also been studied extensively [75].

2.2.1. Lithium/sodium-storage mechanism

The mechanism of metal phosphides, MP$_y$ (M = Mn, V, Sn, Ni, Cu, Fe, Co, Zn, Ge, Se, Mo, Ga, In; y = 1, 2, 3, 4), according to the features of the metal and the metal-phosphorus bonds stability when reacted with Li, can be divided into the following two categories.

Insertion reaction: $MP_n \leftrightarrow Li_xMP_n$ (3)
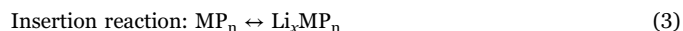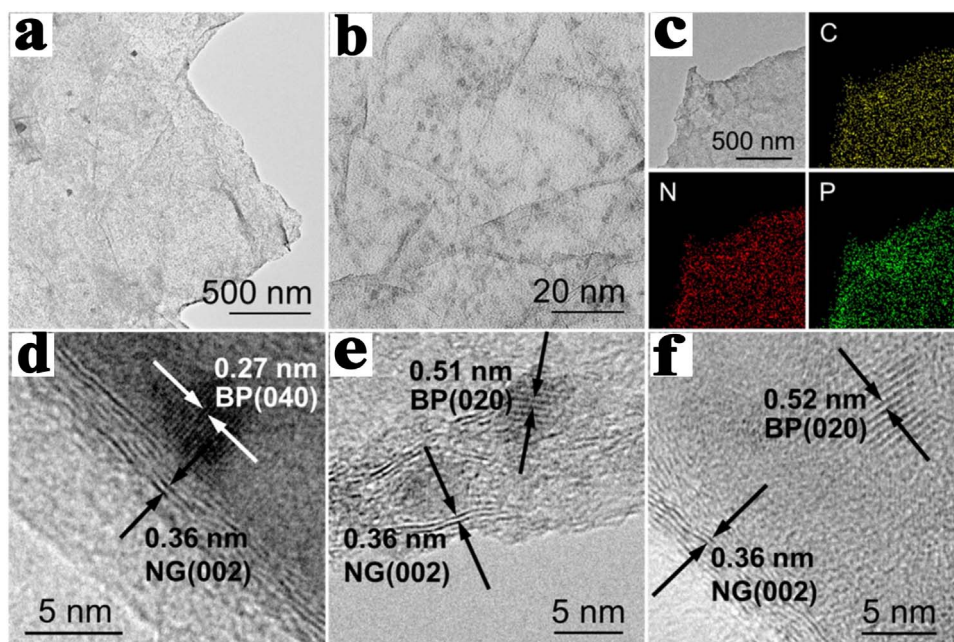
Fig. 8. (a) Low- and (b) high-magnification TEM images of van der Waals heterostructures, (c) TEM image of van der Waals heterostructures and the corresponding EDS maps of elemental C, N and P, (d–f) HRTEM images of van der Waals heterostructures. (Reproduced with permission. Copyright 2016, ScienceDirect [64]).

Conversion reaction: $MP_n \leftrightarrow M (Li_xM) + Li_xP$ (4)

When the metal phosphides have stable crystalline structures, Li_xMP_y is formed through the insertion reaction mechanism. However, the structures of phosphides collapsed within a few insertions/extractions, or full discharge/charge reactions accrued through the conversion reaction mechanisms, providing nanosized Li_3P and M (Li_xM), with bonds between metal and phosphorus broken. The conversion reaction produced nanocrystallites with less severe structural stress. The redox nature of the phosphorus dominated the reactivity of metal phosphides with lithium, and the number of electrons in the anion dominated the capacities. The Na storage mechanism of metal phosphides needs further investigations due to the just emerging study of metal phosphides in NIBs.

2.2.2. Mn-P phosphides

Little was known about the electrochemical behavior of metal phosphides, which lie between the more ionic nitrides and the intermetallic antimonides in their chemistry, before the intercalation of lithium into metal phosphides MP_4 at low-potential was demonstrated by Souza et al. They proposed that the intercalation/deintercalation of lithium ion in MP_4 accompanied by a topotactic first-order transition between different but related crystal structures at room temperature as the following process.

$MnP_4 + 7Li^+ + 7e^- \leftrightarrow 2Li_7MnP_4$ (5)

The P-P bonds between the binary layered phosphide were cleaved when Li inserted to produce crystalline Li_7MnP_4 and were reformed after Li extraction from Li_7MnP_4 (Fig. 10a), thereby storing electrons. In the field of LIBs, this topotactic intercalation is an interesting concept, as its covalent bond breaking within the crystalline solid state and bond reformation by the electrochemical reaction are facile [76]. Then MnP nanoparticles (< 30 nm) were prepared through the reaction of dimanganese decacarbonyl and trioctyl phosphine (TOP) at 380 °C under Ar atmosphere. During the first cycle, Li^+ was inserted into the MnP to first form LiMnP and then LiMnP phase was decomposed to LiP and LiP_7 phases after discharged to 0 V; while LiMnP phase was turned into the LiP and LiP_5 phases when charging to 2 V (Fig. 10b). Irreversible phase transitions with LiMnP phase to $Li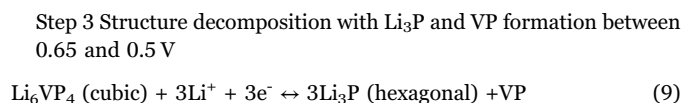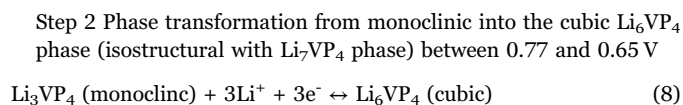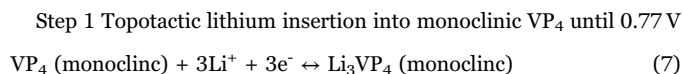P_x$ phases, along with the formation of inactive LiMnP led to a very low initial Coulombic efficiency. Subsequent decomposition and pulverization of the Li_xP phase led to a continuous capacity fading of MnP [77].

2.2.3. V-P phosphides
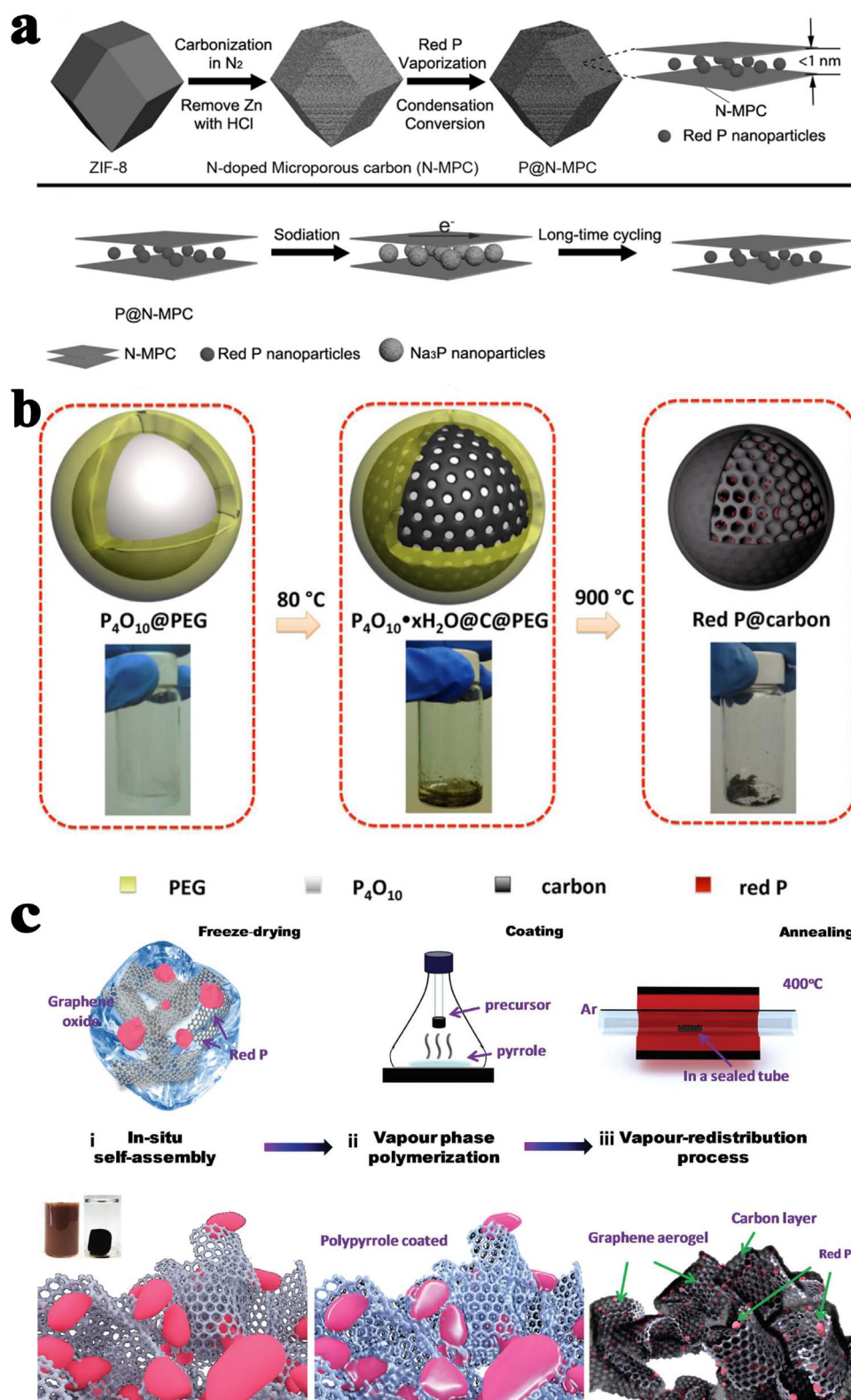
Since the discovery of low potential intercalation behavior in metal phosphide MnP_4, the phosphorus-based intermetallic compounds as anode materials for LIBs have been studied as a possibility. Another topotactic Li fist-order transition in a hexagonal VP electrode was demonstrated during the Li insertion/extraction process. The VP delivered high initial discharge and charge volumetric capacity of 1990 and 1452 mA h/cm³, respectively, with capacity retention of 80% over 250 cycles. *Ex-situ* XRD and X-ray absorption spectroscopy (XAS) (Fig. 11a–c) analyses confirmed the electrochemical reaction mechanism of VP electrode as the following [78].

$VP + Li^+ + e^- \leftrightarrow LiVP$ (6)

Besides VP, the Li insertion/extraction was also investigated in VP_4 and VP_2 [79,80]. Kim et al. prepared VP_4 by mechanical alloying and carried out its electrochemical characterization during cycling. According to differential capacity plots and X-ray analyses (Fig. 11d & e), a four-step reduction process was proposed:

Step 1 Topotactic lithium insertion into monoclinic VP_4 until 0.77 V

VP_4 (monoclinc) $+ 3Li^+ + 3e^- \leftrightarrow Li_3VP_4$ (monoclinc)   (7)

Step 2 Phase transformation from monoclinic into the cubic Li_6VP_4 phase (isostructural with Li_7VP_4 phase) between 0.77 and 0.65 V

Li_3VP_4 (monoclinc) $+ 3Li^+ + 3e^- \leftrightarrow Li_6VP_4$ (cubic)   (8)

Step 3 Structure decomposition with Li_3P and VP formation between 0.65 and 0.5 V

Li_6VP_4 (cubic) $+ 3Li^+ + 3e^- \leftrightarrow 3Li_3P$ (hexagonal) $+VP$ (9)

Step 4 Lithium insertions into VP lattice below 0.5 V

Fig. 9. (a) Schematic illustration of the preparation process for P@N-MPC and sodiation process of P@N-MPC. (Reproduced with permission. Copyright 2017, Wiley-VCH Verlag GmbH & Co [67]) (b) Schematic and digital photographs of the synthesis procedure for the ultrafine red phosphorus particles embedded in a 3D carbon framework. (Reproduced with permission. Copyright 2016, ScienceDirect [68]) (c) Schematic illustration of the synthesis process for C@P/GA composite in three steps. (Reproduced with permission. Copyright 2016, Wiley-VCH Verlag GmbH & Co [74]).

$$VP + Li^+ + e^- \leftrightarrow LiVP \tag{10}$$

VP$_4$ electrode showed good cycling performance (430 mA h/g after 100 cycles), and high initial Coulombic efficiency at first cycle within

0.77–2.5 V [79]. Gillot et al. reported the Li electrochemical behavior of lithium with amorphous and crystalline VP$_2$, respectively. The reversibly insertion/extraction of 3.5 Li can be achieved in the amorphous VP$_2$, as a comparison, solely 2.5 for the crystalline VP$_2$. Based on the
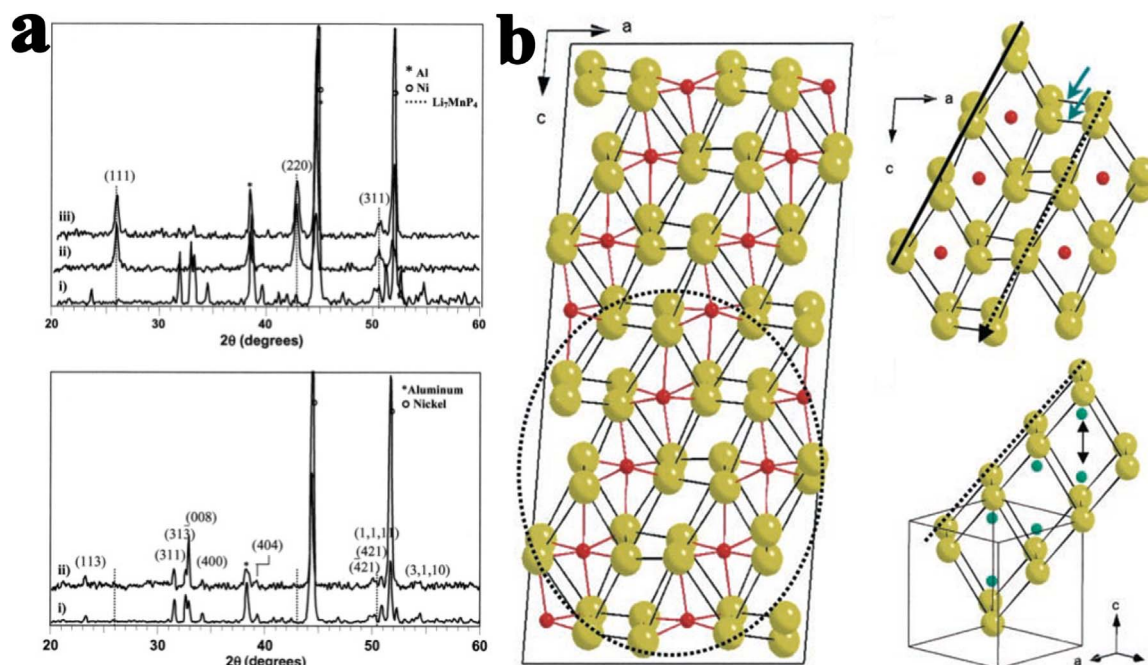
Fig. 10. (a) Ex situ XRD patterns of MnP$_4$ at different cycling stages; (b) The relation of the layered structure of MnP$_4$ to the antifluorite structure of Li$_7$MnP$_4$ and the proposed mechanism for the transformation. (Reproduced with permission. Copyright 2002, Science Society [76]).
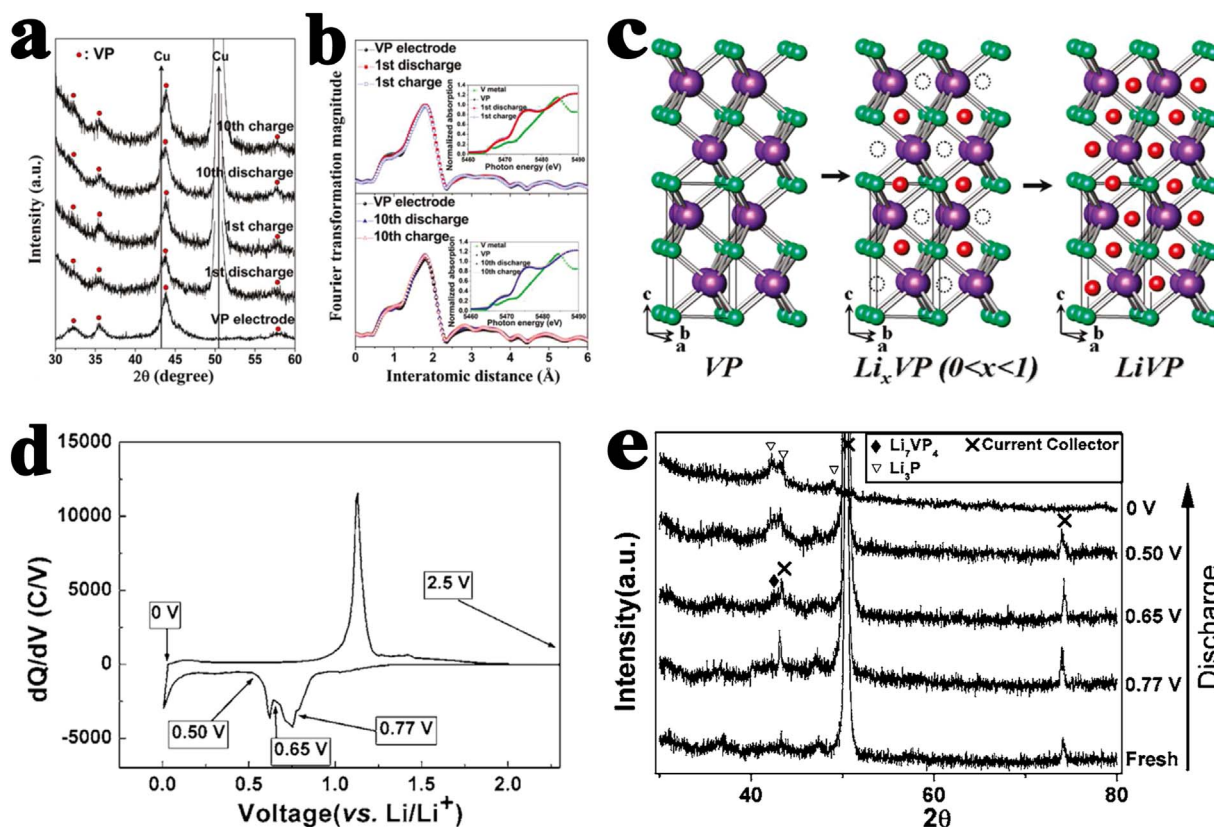

Fig. 11. Reaction mechanism of the VP electrode: (a) Ex situ XRD patterns during the 1st and 10th cycle; (b) EXAFS and XANES results during the 1st and 10th cycle; (c) Suggested topotactic reaction mechanism of VP (V atoms, green; P atoms, purple; Li atoms, red). (Reproduced with permission. Copyright 2009, American Chemical Society [78]) (d) Differential capacity plot of VP$_4$. (e) Ex situ XRD pattern of VP$_4$ during the first discharge. (Reproduced with permission. Copyright 2005, The Electrochemical Society [79]).

XRD, HRTEM and NMR results, no V nanoparticles and the formation of Li$_3$P were detected, which confirmed that the Li reactivity mechanism were not conversion reaction. They suggested that the nature of the redox center upon lithiation was possibly changed from a cation (M) to an anion (P) [80].

2.2.4. Sn-P phosphides

There are four forms of Sn-P phosphides available, viz., SnP$_3$, Sn$_3$P, SnP, and Sn$_4$P$_3$ [81,82]. Among these Sn-P phosphides, Sn$_4$P$_3$ possesses a layered structure, in which P layer alternates with Sn layer, organized into 7-layer units along the c-axis (Fig. 12**a**). The layered
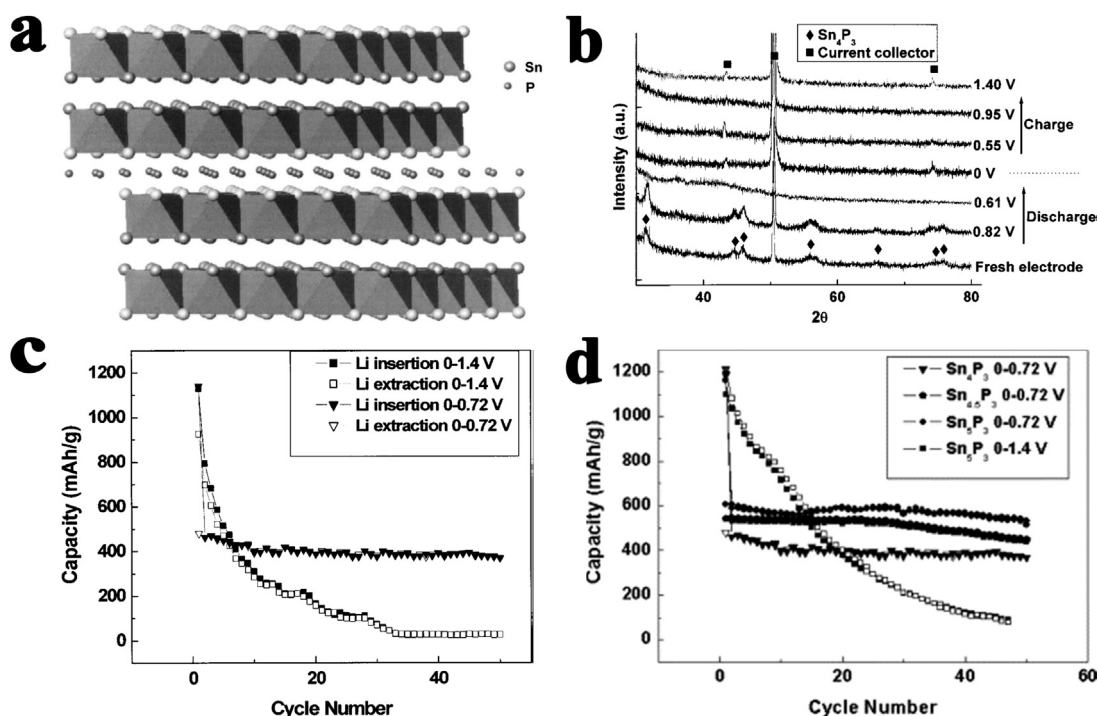
Fig. 12. (a) Crystal structure of Sn_4P_3; (b) Ex situ XRD patterns of Sn_4P_3 electrode during the first cycle; (c) Cyclability of the Sn_4P_3 electrodes. (Reproduced with permission. Copyright 2004, The Electrochemical Society [85]) (d) Cycle performances of Sn_4P_3, $Sn_{4.5}P_3$, and Sn_5P_3. (Reproduced with permission. Copyright 2005, ScienceDirect [86]).

structure, which may insert cations between two weakly bound tin layers, makes it possible as anode materials [83]. The electrochemical property of Sn_4P_3 was studied in 2004 [85], although its synthesis was first reported in 1967 [84]. The Sn_4P_3 electrode delivered a high first discharge capacity of 1130 mA h/g with a high initial Coulombic efficiency of 79.64%. The reaction mechanism during discharge was suggested as: $Sn_4P_3 \rightarrow Li_2Sn_4P_3 \rightarrow Sn + (LiP_5 + LiP_7) \rightarrow Sn + LiP \rightarrow Li_4Sn + Li_3P$ (Fig. 12**b**). At a limited voltage window, the Sn_4P_3 electrode showed a stable cyclability with a high capacity of 370 mA h/g after 50 cycles (Fig. 12**c**). On the other hand, the formation of Li_3P during the first cycle led to a relatively large irreversible capacity and Sn_4P_3 still contained high phosphorus content. To increase the reversible capacity at first cycle and enhance the Coulombic efficiency, an increase of the tin content in Sn_4P_3 active material was attempted through solid-solution formation using mechanical alloying technique. Based on the investigative analyses, the region for the solid-solution formation of $Sn_{4+\delta}P_3$ was $0 \leq \delta \leq 1$. The tin-rich solid solutions had no topotactic lithium insertion reaction which took place in stoichiometric Sn_4P_3 during the first cycle. In the following cycles, both of them had the similar reaction mechanism. Due to the higher tin content, improved cyclability with a 20% higher reversible capacity than that of stoichiometric Sn_4P_3 was achieved (Fig. 12**d**) [86]. León et al. further investigated the mechanism of electrochemical reactions with lithium using ^7Li and ^{31}P magic angle spinning nuclear magnetic resonance and ^{119}Sn Mössbauer spectroscopy techniques. The reaction of Sn_4P_3 with lithium can be broken down into three reactions: 1) $Sn_4P_3 + 3Li \rightarrow 4Sn + 3LiP$; 2) $3LiP + 6Li \rightarrow 3Li_3P$; 3) $4Sn + 17Li \rightarrow Li_{17}Sn_4$. The third reaction started almost at the beginning of the discharge and continued through to the end of the discharge. Reversibility was almost limited to the third reaction, and thus the maximum allowed reversible capacity was limited [87].

Subsequently, the electrochemical performance of Sn_4P_3 was improved through various strategies. Wu et al. prepared Sn_4P_3 thin films through reactive pulsed laser deposition. The films delivered a high reversible capacity of 906.2 mA h/g with capacity retention of 60.69% after 10 cycles at 100 mA/g [88]. Liu et al. prepared Sn_4P_3 nanoparticles (~ 15 nm) through a solvothermal method. The nano Sn_4P_3

materials showed stable cyclability with a high reversible capacity of 442 mA h/g after 320 cycles at 100 mA/g [89]. Liu et al. also reported hollow spherical microstructured Sn_4P_3 fabricated by a facile solvothermal approach using ethylenediamine tetraacetic acid (EDTA) as chelating and capping reagent. The as-prepared Sn_4P_3 hollow microspheres presented a high reversible capacity of 689 mA h/g at 500 mA/g [90].

Sn_4P_3 was first reported for NIBs anode by Kim et al., who demonstrated that Sn_4P_3 was a promising anode material due to its highest volumetric capacity among anode materials for NIBs reported to date and its appropriately low redox potential of about 0.3 V vs. Na/Na$^+$. In this study, Sn_4P_3 presented a reversible capacity of 718 mA h/g and maintained the same capacity over 100 cycles [91]. Simultaneously, Qian et al. synthesized Sn_4P_3/C nanocomposite via a green approach. As a novel anode material for NIBs, the Sn_4P_3/C delivered a very high reversible capacity of 850 mA h/g at 500 mA/g and a good retention capacity of 731 mA h/g over 150 cycles [92]. Besides, they both revealed a synergistic reaction mechanism of the Sn_4P_3 with sodium, where the Sn nanoparticles improved the electric conductivity and enhanced the reaction activities of the P component, while the elemental P and its sodiated product Na_3P prevented aggregation and volume expansion of the Sn particles during cycling (Fig. 13). To address the issue of volumetric expansion during sodiation, Li et al. synthesized core-shell $Sn_{4+x}P_3$@amorphous Sn-P composites, which delivered a high capacity of about 465 mA h/g, with negligible capacity fading over 100 cycles, at a current density of 100 mA/g [93]. However, volume expansion may cause cracking of the shells with the conventional core-shell structure. Liu et al. designed a yolk-shell structure to mitigate this problem. The structure consisted of the Sn_4P_3 nanoparticles yolk and the carbon shell. With the void space between the shell and yolk nanoparticles, the expansion of Sn_4P_3 during sodiation was allowed without breaking the carbon shell. Due to their unique structure, the yolk–shell Sn_4P_3@C nanospheres delivered a very high reversible capacity of 790 mA h/g and showed stable cycling performance (a high capacity of 360 mAh/g at 1500 mA/g after 400 cycles) (Fig. 14) [94]. Recently, Li et al. synthesized Sn_4P_3/reduced graphene oxide (Sn_4P_3/RGO) hybrids through an in situ solution-based phosphorization at low-temperature with the adjustable graphene
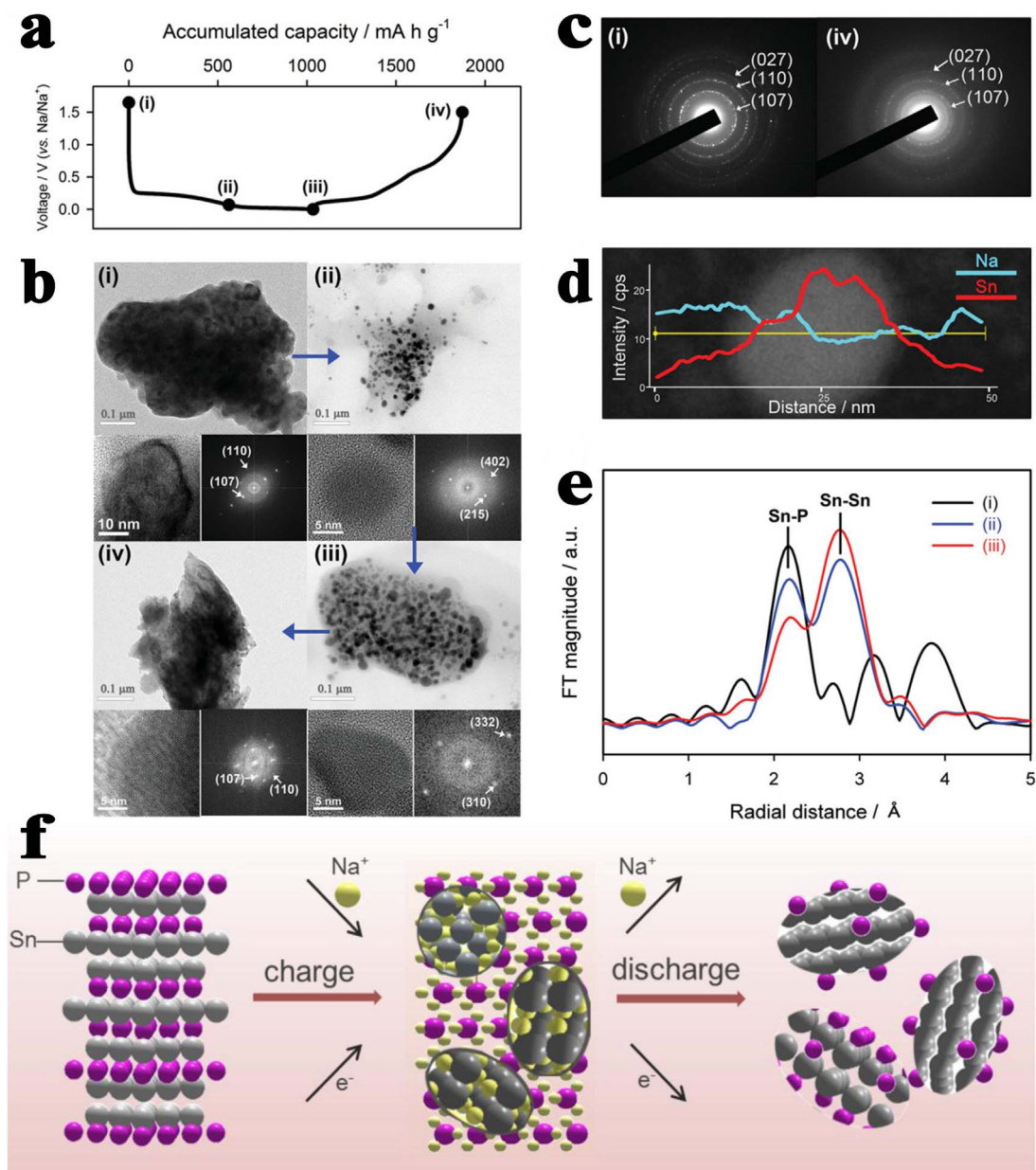
Fig. 13. (a) First galvanostatic charge and discharge profiles of the Sn$_4$P$_3$ electrode obtained without an FEC additive. The different points indicate (i) pristine, (ii) 0.07 V, (iii) 0 V and (iv) 1.5 V. (b) The ex situ HR-TEM bright-field images at each point in (a) (insets of (i) through (iv): enlarged HR-TEM images (left) of crystalline regions and the corresponding FFT patterns (right)). (c) Electron diffraction (ED) patterns at the points (i) and (iv) in (a). (d) STEM dark-field image and EDX line profiles of Sn and Na in the nanocrystalline region at the point (ii) in (a). (e) Sn K-edge EXAFS spectra of Sn$_4$P$_3$ during sodiation. (Reproduced with permission. Copyright 2014, Wiley-VCH Verlag GmbH & Co [91]) (f) Schematic illustration of the Na-storage mechanism in Sn$_4$P$_3$ electrode. (Reproduced with permission. Copyright 2014, American Chemical Society [92]).

content. The monodisperse Sn$_4$P$_3$ nanoparticles (< 6 nm) were uniformly loaded on the graphene nanosheets, which interconnected to form 3D mesoporous architecture structures. RGO nanosheet not only improved the conductivity of the nanohybrids but also buffered the volume change during cycling. Benefited from the porous structure of the Sn$_4$P$_3$/RGO and the synergistic effect between Sn$_4$P$_3$ nanoparticles and graphene nanosheets, the Sn$_4$P$_3$/RGO hybrids showed significantly improved electrochemical performance with high reversible capacity of 656 mAh/g at 100 mA/g, high-rate capability, and a superior long cycling life (362 mA h/g after 1500 cycles at a high current density of 1.0 A/g) (Fig. 15) [95].

Besides Sn$_4$P$_3$, SnP and SnP$_3$ were also reported as anode materials [96,97]. Kim et al. reported teardrop-shaped ultrafine SnP$_{0.94}$ nanoparticles synthesized in a solution mixture of TOP and TOPO through a thermal decomposing (Fig. 16a−e). The teardrop-shaped ultrafine SnP$_{0.94}$ nanoparticles showed an initial capacity of

740 mAh/g and a good retention capacity of 681 mA h/g after 40 cycles at 120 mA/g at the voltage range of 0 and 1.2 V. The good electrochemical cycle performances were attributed to the structure stability with a lithium intercalation/deintercalation process without conversion reaction (Fig. 16f & g) [96]. The electrochemical performance of SnP$_3$/C anodes for NIBs was investigated by Fan et al. And the SnP$_3$/C provided a high capacity of ~ 810 mA h/g without capacity fading over 150 cycles at 150 mA/g. Besides, SnP$_3$/C retained 400 mA h/g even at a high current density of 2560 mA/g and the overall performance was shown to be the best among P, Sn, and Sn-P compound as anodes materials for NIBs reported to date. The excellent electrochemical performance of SnP$_3$/C was mainly attributed to the strong Sn-P bonding interaction, which successfully prevented the pulverization and aggregation of Sn and P, partially self-healing the structure of SnP$_3$/C composites (Fig. 16h) [97].
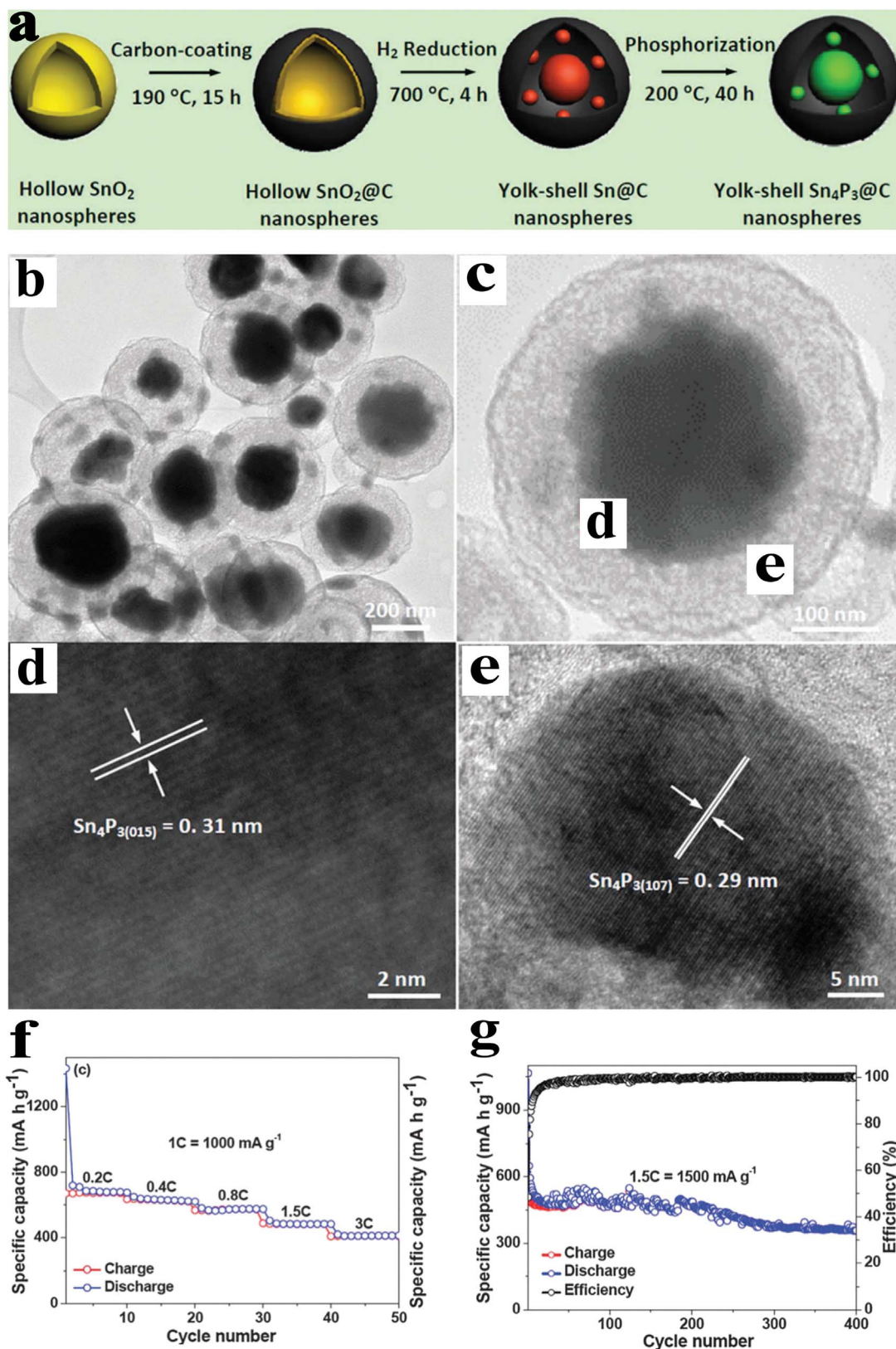
Fig. 14. (a) Schematic illustration of the fabrication of uniform yolk−shell Sn$_4$P$_3$@C nanosphere anodes; (b−e) TEM images of uniform yolk−shell Sn$_4$P$_3$@C nanosphere products; (f) Rate capability at different rates; (g) Long cycling performances of yolk−shell Sn$_4$P$_3$@C nanospheres at 1500 mA/g. (Reproduced with permission. Copyright 2015, The Royal Society of Chemistry [94]).
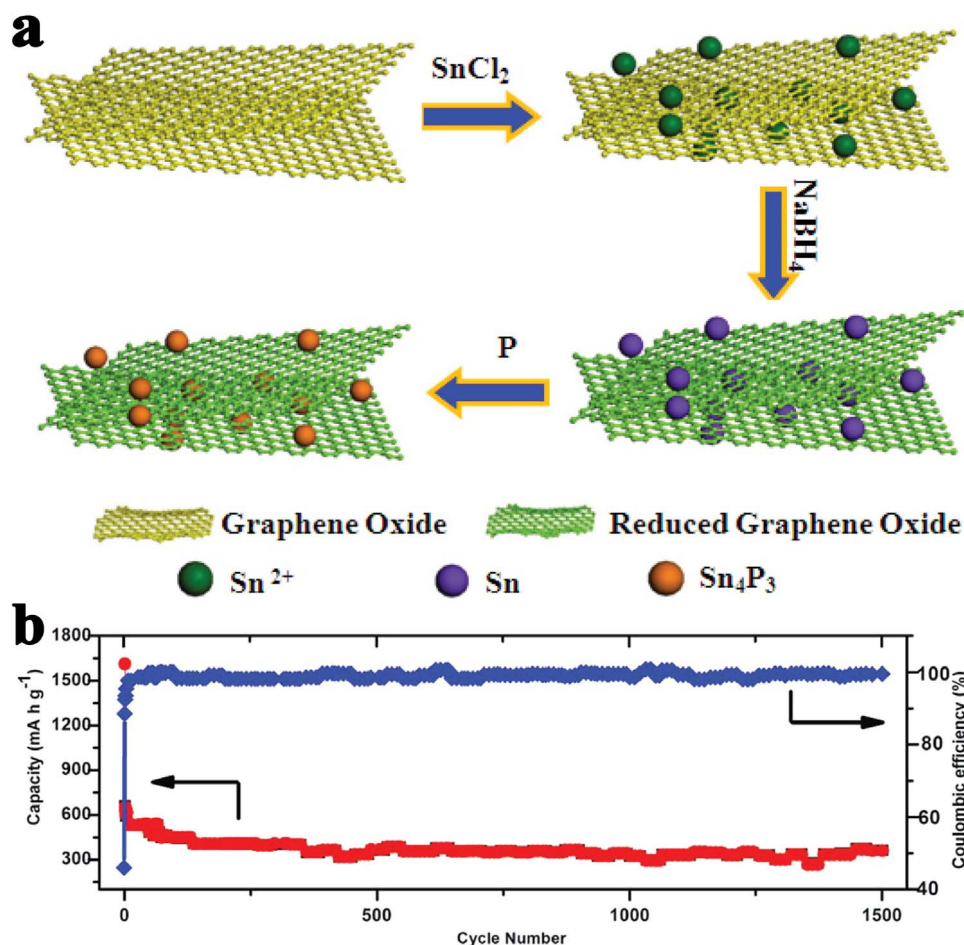
Fig. 15. (a) Schematic illustration of the synthesis process of the Sn_4P_3/RGO hybrid sample; (b) Long cycling performance of Sn_4P_3/RGO samples at a current density of 1.0 A/g for 1500 cycles. (Reproduced with permission. Copyright 2016 Wiley-VCH Verlag GmbH & Co [95]).

2.2.5. Ni-P phosphides

Due to the richness of the associated phase diagram, nickel phosphides, such as NiP_2 [98,99], NiP_3 [100], Ni_3P [101–103], Ni_2P [104–117], Ni_5P_4 [118,119] and $Ni_{12}P_5$ [120,121], are studied most as anode materials for batteries among metal phosphides. Nickel phosphides can be divided into two categories: phosphorus-rich phases and metal-rich phases. Phosphorus-rich phases (NiP_2 and NiP_3), owning to their higher theoretical capacities, are promising for LIBs/NIBs anodes. Gillot et al. first investigated the Li storage performance of cubic and monoclinic NiP_2 polymorphs. They found that cubic NiP_2 reacted with lithium through a direct conversion process during the first discharge, while monoclinic NiP_2 suffered from an intercalation process followed by a conversion process (Fig. 17**a & b**). After the first discharge, the mechanisms of both phases were transformed to classical conversion. Electronic structure calculations confirmed that such a different behavior was rooted in subtle structural changes. It suggested that the closely packed structure of the cubic NiP_2 hindered any Li^+ insertion and thus it reacted with lithium through a direct conversion process into Li_3P and Ni. While the monoclinic NiP_2 owned some available interlayer space to accommodate Li^+ with the formation of the monoclinic $Li_{2.5}NiP_2$ phase [98]. Then Fullenwarth et al. first studied the electrochemical mechanism and behavior of NiP_3 as an anode material for both LIBs and NIBs. It was demonstrated that after a full discharge, the final reaction products were Li_3P/Na_3P embedded Ni nanoparticles (Fig. 17**c & d**). Furthermore, the NiP_3 electrode delivered a reversible capacity higher than 1000 mA h/g after 50 cycles for LIB and 900 mA h/g after 15 cycles for NIB [100]. Recently, Lou et al. designed and anchored monodispersed carbon-coated cubic NiP_2 nanoparticles on carbon nanotubes. With the unique structural feature, the reaction kinetics was enhanced and stable cyclability (more than 1000 cycles) with high capacity retention (high capacities of 816 mAh/g after 1200 cycles at 1300 mA/g and 654.5 mA h/g after 1500 cycles at 5 A/g) were achieved. However, it should be pointed out that phosphorus-rich phases have to be obtained at high temperature or under complex conditions such as hydrothermal synthesis for a long time [99].

Compared with phosphorus-rich phosphides, metal-rich phases, including Ni_3P, Ni_2P, Ni_5P_4 and $Ni_{12}P_5$, can be obtained at relatively lower temperature and under simpler conditions. Moreover, they present a stronger metallic character due to their higher proportion of Ni-Ni bonds, exhibiting relatively stable cyclability. Cruz et al. electrodeposited Ni_3P thin films on a stainless steel substrate and then heated at 500 °C in an argon or vacuum atmosphere. The Ni_3P films, which consisted of pseudo-spherical agglomerates of nanosized particles (less than 70 nm in size) (Fig. 18**a**), which showed better capacity retention than bulk Ni_3P, but exhibited a low reversible capacity less than 100 mA h/g after a few cycles [101]. To obtain a high reversible capacity, Xiang et al. electrodeposited Ni_3P films (50–100 nm Ni_3P nanoparticles) on porous nickel foam substrate, which presented improved cycling stability and capacity (340 mA h/g after 40 cycles) [102]. Then they further enhanced the electrochemical performance of Ni_3P by fabricating porous Ni_3P films (Fig. 18**b**), providing high capacities of 557 mAh/g and 243 mA h/g at 77.6 mA/g and 194 mA/g after 50 cycles [103]. Moreover, Lu et al. synthesized single-crystalline dinickel phosphide (Ni_2P) nanowires [104] (Fig. 18**c**) and porous Ni_2P nanosheets [105] (Fig. 18**d**) to improve their electrochemical performance, which delivered specific reversible capacities of 434 mA h/g at 54.32 mA/g, 326 mA h/g at 271.6 mA/g after 50 cycles and 379.8 mA h/g at 54.32 mA/g after 50 cycles, respectively.
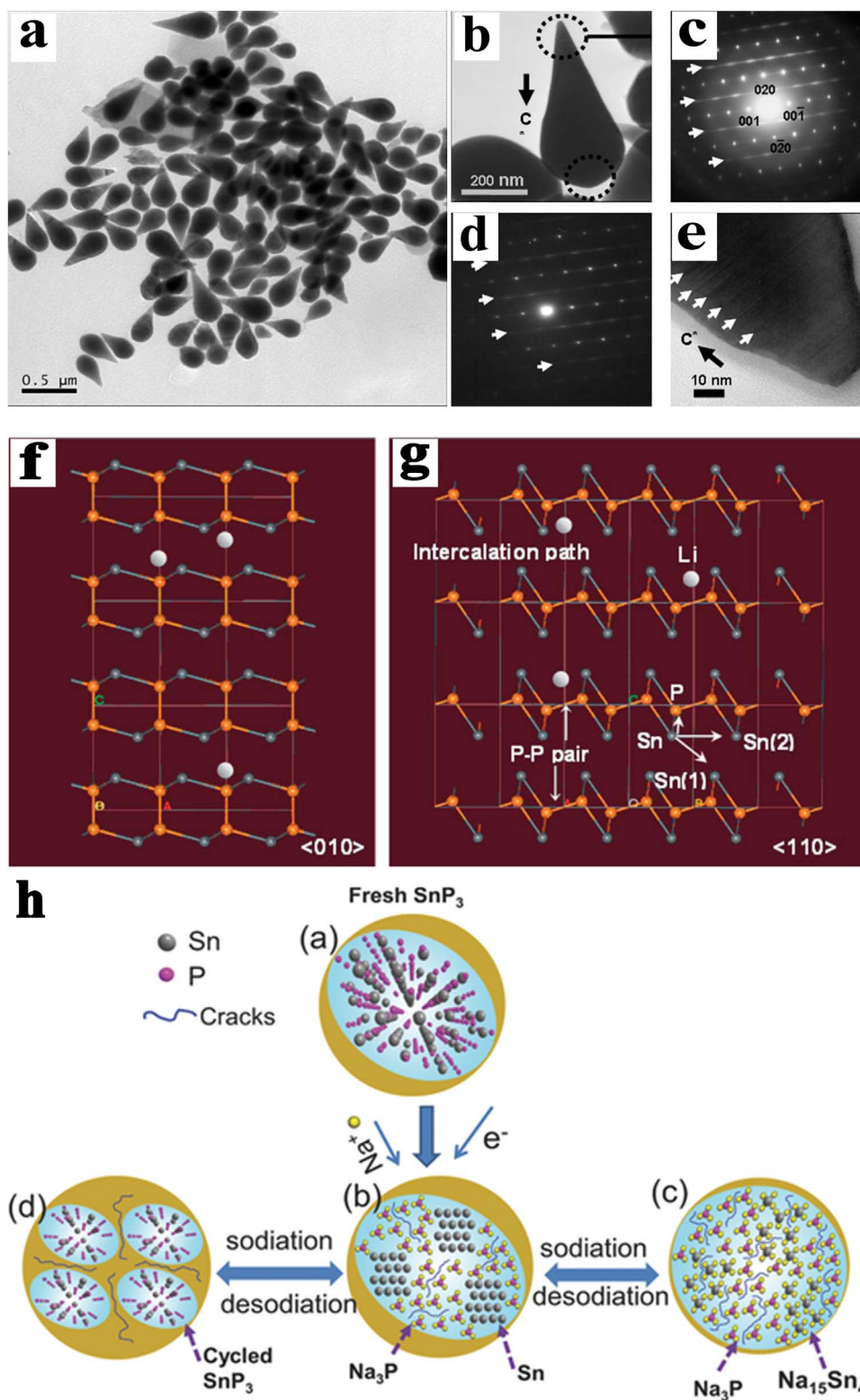
Fig. 16. (a, b) TEM images of teardrop-shaped SnP$_{0.94}$ particles; (c) SAED pattern of the tail portion of a SnP$_{0.94}$ particle; (d) SAED pattern of the head portion of a SnP$_{0.94}$ particle; (e) HRTEM image of the tail section of SnP$_{0.94}$ particle. Possible intercalating path from SnP$_{0.94}$ crystal structures which consists of (f) Sn-P1 (2c site) and (g) Sn-P2 (6i site) atomic pairs under the space group of P-3m1 (Sn atom: dark gray and P atom: orange). (Reproduced with permission. Copyright 2007, Wiley-VCH Verlag GmbH & Co [96]) (h) Schematic illustration for the sodiation and outlayer denotes carbon. (Reproduced with permission. Copyright 2015, Wiley-VCH Verlag GmbH & Co [97]).

Besides the designing of nanostructured nickel phosphides, compositing with carbonaceous materials, e.g., carbon coating [111,112,117,118,121], carbon nanotubes [119], carbon fibers [108,109,120] or graphene [113–116], would be a favorable strategy to improve the electrochemical performance of nickel phosphides. The

carbon coating can effectively buffer the volume change during Li$^+$/Na$^+$ insertion/extraction and prevent the aggregation of the resulted products. Lu et al. synthesized a monophase Ni$_5$P$_4$/C composite with a uniform sphere-like morphology and a thin amorphous carbon shell through a wet-chemistry reaction followed by a solid-state reaction
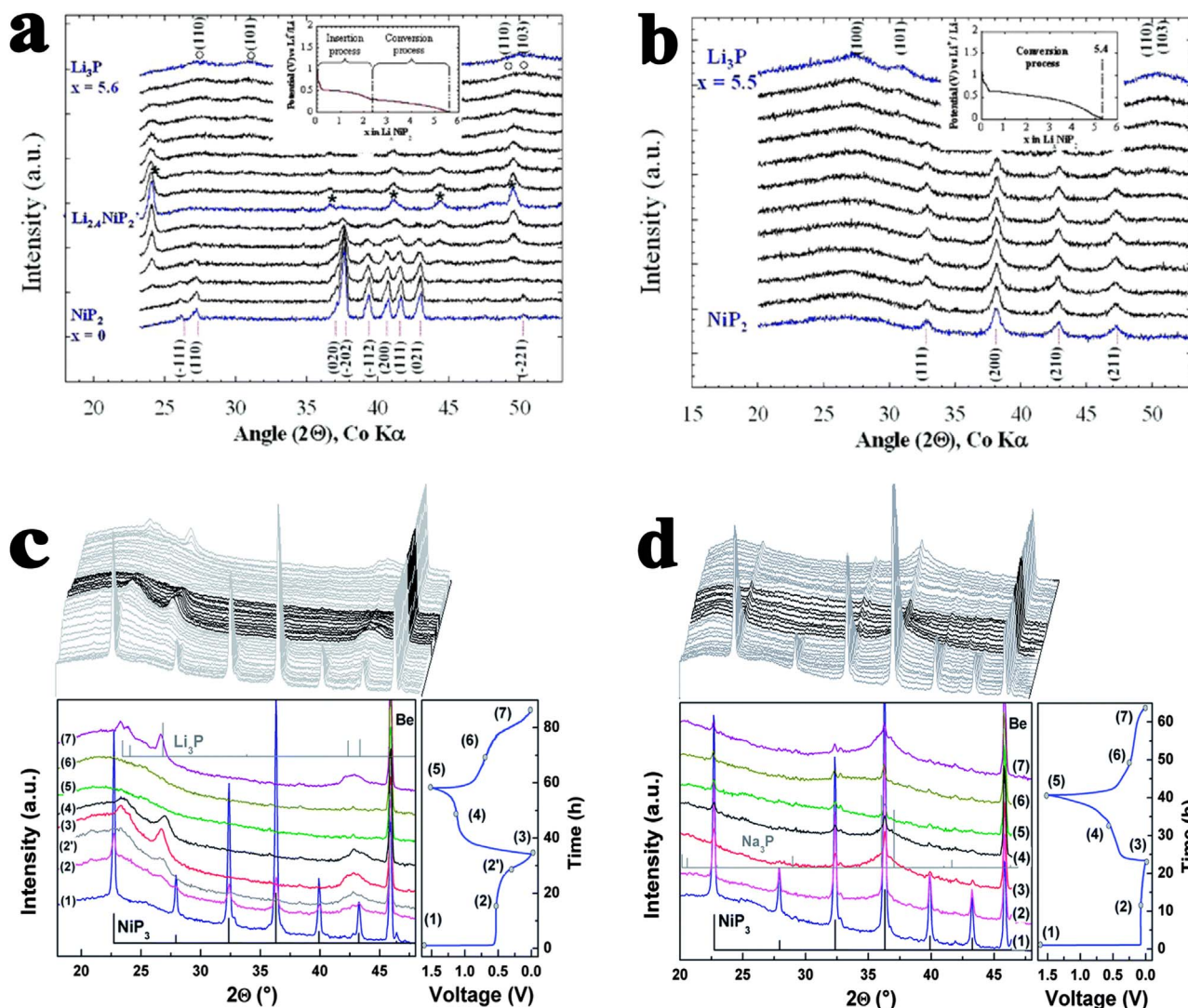
Fig. 17. In situ XRD patterns of (a) monoclinic NiP_2 and (b) cubic NiP_2 collected during the first discharge. (Reproduced with permission. Copyright 2005, American Chemical Society [98]) In situ XRD patterns collected at various stages of the first discharge of (c) a NiP_3/Li cell and (d) a NiP_3/Na cell. (Reproduced with permission. Copyright 2014, The Royal Society of Chemistry [100]).

(Fig. 19**a**). The thickness of amorphous carbon shell was uniform and approximately 10 nm with content of about 9.91 wt% in the composites (Fig. 19**b**). With the amorphous carbon shell, the resulting core-shell Ni_5P_4/C composite exhibited an excellent cyclability of 644.1 mA h/g at 71.89 mA/g over 50 cycles [117]. To further optimize the structure and electrochemical performance of nickel phosphide/carbon composites, peapod-like nanocomposites, which consisted of nanosized nickel phosphide particles encapsulated in carbon fibers, were proposed. Zhang et al. prepared a peapod-like $Ni_{12}P_5$ composite, using a $NiNH_4PO_4·H_2O$ nanorod as the precursor and sacrificial templates, and glucose molecules served as carbon source (Fig. 19**c–g**). Due to their extraordinarily active surfaces/interfaces and robust stabilities, the obtained peapod-like $Ni_{12}P_5$/C nanocomposites showed a high reversible capacity of 600 mA h/g at 3.0 A/g over 200 cycles, with extraordinarily stable cyclability and Coulombic efficiency up to 100% for each cycle [120]. Besides one dimensional peapod-like nanocomposites, two dimensional sandwich-like structural materials are promising for LIBs/NIBs. Feng et al. encapsulated sandwich-like Ni_2P nanoparticles in coupled graphene sheets by a simple and controllable synthetic method (Fig. 20**a**). With the unique sandwich architecture, a fast charge transport through the conducting paths was provided by the conductive matrix, leading to excellent cycling stability and a high reversible capacity of 625 mA h/g at 108.64 mA/g over 200 cycles

[106]. Recently, Wu et al. fabricated 3D yolk-shell-like $Ni_2P@C$ nanoparticles which embedded into porous graphene networks (denoted as $Ni_2P⊂pGN$) through an assembly and self-template strategy (Fig. 20**d–f**). This architecture combined the advantages of nanostructure and microstructure and provided highly efficient electron pathways around the active nanoparticles (Fig. 20**b & c**). The $Ni_2P⊂pGN$ electrodes exhibited excellent Li and Na storage performances. After 500 cycles, the charge capacity reached 457 mA h/g at 300 mA/g, with capacity retention up to 100% for LIB. For NIB, it also presented a high initial charge capacity of 181 mA h/g at 200 mA/g and a good retention capacity of 161 mA h/g after 100 cycles [107].

In addition to designing nanostructured nickel phosphides and coating or compositing with carbonaceous materials, Luo et al. synthesized 0D nickel phosphides nanocrystals-2D ultrathin black phosphorus heterostructure ($Ni_2P@BP$). The $Ni_2P@BP$ displayed quick electrochemical response with improved Li ion diffusion kinetics, and exhibited an excellent rate capability (322 mA h/g at 10 A/g), high reversible capacity of around 1196.3 mA h/g at 100 mA/g and outstanding cycle life of 743.7 mA h/g over 1000 cycles at 1 A/g [110].

2.2.6. Cu-P phosphides

Copper forms three phosphorus compounds (Cu_3P, CuP_2 and Cu_2P_7) according to the Cu-P phase diagram [122]. Among them,
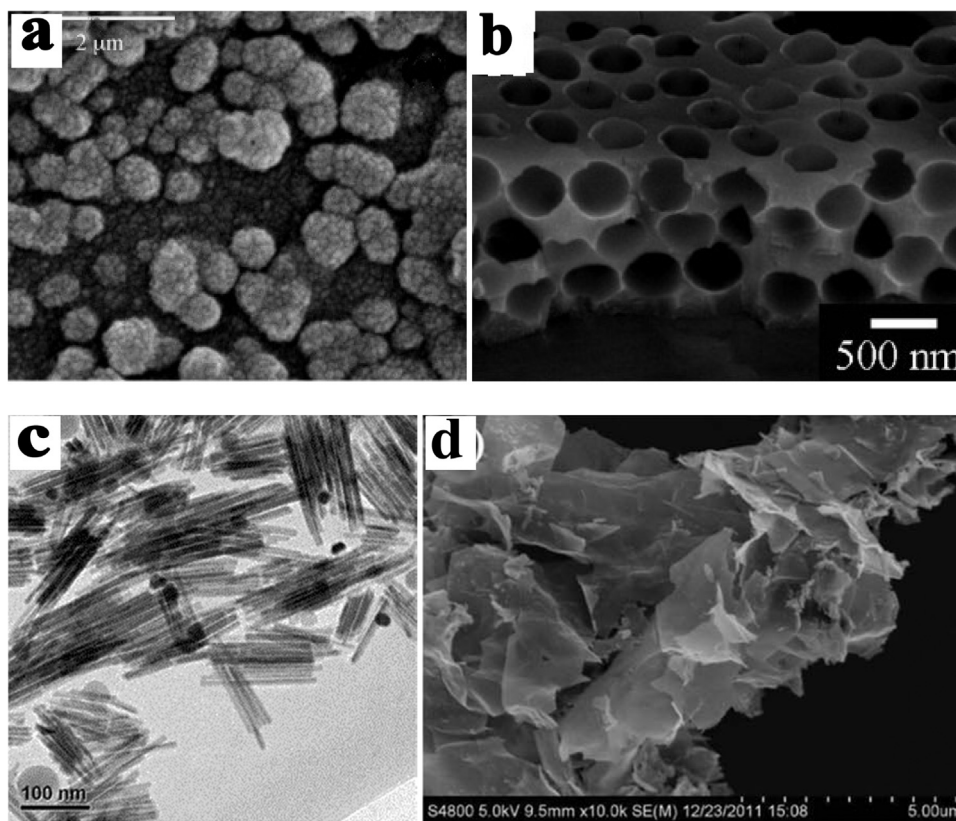
Fig. 18. (a) Top view SEM images for Ni–P films. (Reproduced with permission. Copyright 2007, ScienceDirect [101]) (b) SEM images of the porous Ni_3P film. (Reproduced with permission. Copyright 2011, ScienceDirect [103]) (c) TEM image of Ni_2P nanowires. (Reproduced with permission. Copyright 2012, The Royal Society of Chemistry [104]) (d) SEM images of Ni_2P nanosheets. (Reproduced with permission. Copyright 2012, the Royal Society of Chemistry [105]).

Cu_3P is the most studied material as anode for batteries [123–135], due to its air stability. Serving as an anode material for LIBs/NIBs, Cu_3P possesses theoretical gravimetric capacity of 390 mA h/g and volumetric capacity of 3020 mA h/cm^3. Pfeiffer et al. [123] and Bichat et al. [124] first synthesized pure Cu_3P using different methods and investigated its electrochemical reaction with lithium, respectively. The Cu_3P film synthesized via solid-state reaction delivered the discharge capacity of 415 mA h/g at the first discharge and a stable reversible capacity close to 200 mA h/g during subsequent cycles. Bichat et al. demonstrated that Cu_3P with various particle sizes and crystallinities could be obtained through different synthetic route, including solvothermal, ball-milling, spray and ceramic methods. The particle sizes and crystallinities were strongly correlated to the electrochemical performances. Small particle size favored high capacity values and the crystallinity degree of the powder affected the rate capacity, while the microsized powders had better capacity retention. Then the electrochemical reaction mechanism of Cu_3P was investigated through in-situ XRD and first-principles electronic structure calculations, which showed that $3Li^+$ completely inserted into in the Cu_3P electrode and formed three intermediate phases of lithium composition $Li_xCu_{(3-x)}P$ (x = 1, 2 and 3) [125]. The lithium reactions with the CuP_2 impurity and SEI formation contributed to the previously observed extra capacity in discharge [123,124]. Poli et al. further investigated the lithium storage mechanism of Cu_3P by in-situ NMR spectroscopy. ^{31}P and ^7Li NMR data confirmed four distinct $Li_xCu_{3-x}P$ phases (Cu_3P, $Li_{0.2}Cu_{2.8}P$, Li_2CuP, and Li_3P) and the electrochemical reaction mechanisms ($Cu_3P\rightarrow Li_{0.2}Cu_{2.8}P\rightarrow Li_2CuP\rightarrow Li_3P$). During a delithiation process, metallic Cu^0 atomic aggregates intercalated into the Li_2CuP structure. This process resulted in the poor capacity retention when Cu_3P/Li cells were cycled to a low potential of 0.02 V [126].

To enhance their electrochemical capacity and cycle stability, various Cu_3P nano/micro-structures have been designed, including thin Cu_3P films [127,128], Cu_3P hierarchical dendrites [129] and self-supported Cu_3P/Cu electrodes [130–132]. Chandrasekar et al. prepared Cu_3P films by annealing copper discs containing red phosphorus sprayed over copper deposits. The as-prepared carbon-free Cu_3P electrodes showed significantly improved cycle stability over 40 cycles at 20 μA/cm^2 and rate capability [127]. Then well-defined Cu_3P hierarchical dendrites were successfully synthesized by a hydrothermal method. The Cu_3P dendrites displayed a high initial discharge capacity of 1300 mA h/g and kept at 291 mA h/g after 20 cycles at 36.36 mA/g [129]. Fan et al. further investigated the electrochemical performance of self-supported Cu_3P nanowires as anode for NIBs. The Cu_3P nanowires were prepared by phosphidation of the $Cu(OH)_2$ nanowires which was directly grown on copper current collector via an in-situ growth (Fig. 21a). With the unique structure, the Cu_3P nanowire electrode showed a high specific reversible capacity (349 mA h/g at 50 mA/g) and excellent rate performance (137.8 mA h/g at 5000 mA/g) as well as stable cyclability (a capacity retention of 88% at 1000 mA/g over 260 cycles) (Fig. 21b) [130].

Other methods, such as higher cut-off potentials [133], compositing with carbonaceous materials [134], and addition of Fe [135], have also been proposed to improve the cycling performance of Cu_3P. Stan et al. presented the favorable cycle performance of the Cu_3P sample by higher potential cut-off. They demonstrated that an improved cycling stability (more than 50 cycles) was obtained when limited the charge potential to 0.5 V (vs. Li/Li^+), while the capacity fading was faster when charge to 0.02 V (Fig. 21c). The delivered charge capacity in the second cycle with a cut-off potential value of 0.5 V is 223 mA h/g compared to 381 mA h/g when cycled to the lower cut-off potential of 0.02 V. The capacity decay when cycled to lower cut-off potentials (0.02 V) was caused by the much higher energy barrier needed to reconvert to the pristine material. Because the energy barrier needed to reconvert to the pristine material was much smaller when the cut-off potential was
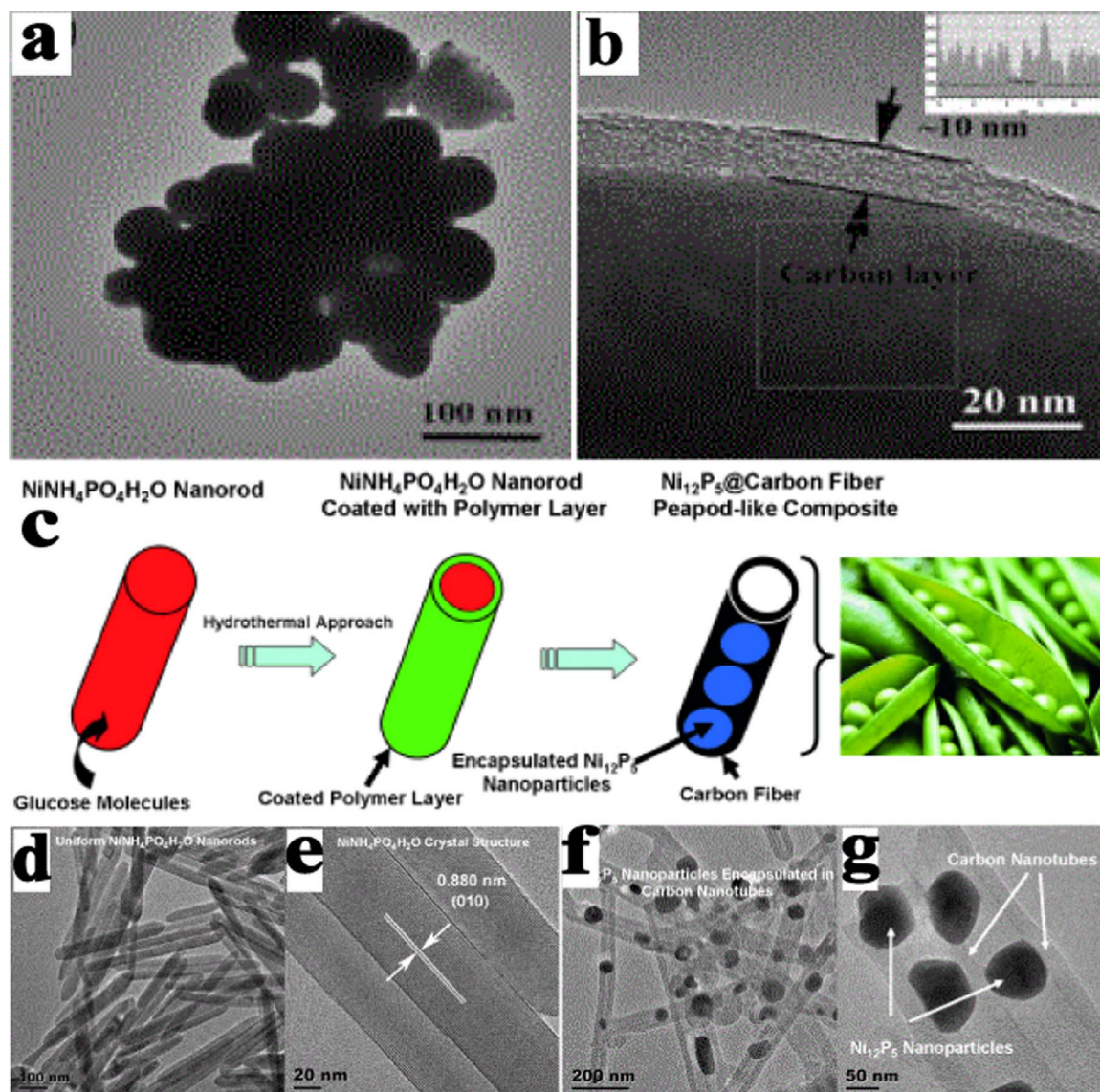
Fig. 19. (a) TEM image of the corresponding composite of the Ni_5P_4/C spheres. (b) TEM image of an individual Ni_5P_4/C sphere; the inset is the corresponding intensity profile for the line scan across the amorphous carbon shell. (Reproduced with permission. Copyright 2012, Wiley-VCH Verlag GmbH & Co. KGaA [117]) (c) Synthesis of peapod-like composites with $Ni_{12}P_5$ nanoparticles encapsulated in carbon fibers. (d) Magnified TEM image of $NiNH_4PO_4 \cdot H_2O$ samples and (e) HRTEM image to clearly demonstrate the layered structure for $NiNH_4PO_4 \cdot H_2O$ nanorods. (f, g) TEM images of the peapod-like $Ni_{12}P_5$ composite. (Reproduced with permission. Copyright 2014, Wiley-VCH Verlag GmbH & Co. KGaA [120]).

limited to 0.5 V, the good capacity retention of these electrodes was achieved [133]. Liu et al. synthesized Cu_3P/reduced graphene oxide (Cu_3P/RGO) nanocomposite by a one-pot solvothermal method. Cu_3P nanoparticles with polyhedral structures were found to anchor homogeneously on the RGO sheets (Fig. 21d). The as-prepared Cu_3P/RGO nanocomposite presented a high capacity of 756.15 mA h/g at 500 mA/g over 80 cycles, good rate capability and superior cyclic performance [134]. Zhou et al. employed Fe addition as a simple strategy to modulate the composition and phase constitution of Cu_3P nanopowders, and thereby to tune the electrochemical performance of the Cu_3P anode. With the addition of Fe, a composite containing Cu_3P as the major phase and some other minor phases including Cu, α-Fe and FeP was formed, determined by XRD, energy dispersive X-ray spectroscopy and Mössbauer spectroscopy. Electrochemical tests demonstrated that the Fe addition effectively improved the cyclability and the rate capability. The Cu_3P electrode with 10% Fe addition had the capacity improved from 82 mA h/g to 178 mA h/g after 50 cycles at 292.5 mA/g between 2.0 V and 0.5 V vs. Li/Li$^+$ [135].

Besides Cu_3P, the binary copper phosphide (CuP_2) is also a good candidate for commercial graphite [136–140], because of its high

energy density and power density. Wang et al. first reported the electrochemical performance and lithium storage mechanism of CuP_2. When the CuP_2 phase was first discharged to 0.0 V vs. Li, there was a long voltage plateau corresponding to the formation of copper and the lithium phosphide (Li_3P). During the subsequent charge process, three voltage plateaus were presented, which were related to the formation of new phase such as Li_2CuP. The irreversible and multistepwise extraction reactions led to a poor cyclability and a low initial efficiency (61.5%) in CuP_2. Although possessing a similar reaction process, lithium copper phosphide delivered a high initial efficiency about 100% and reversible capacity about 750 mA h/g [136]. Recently, CuP_2 nanowires were synthesized via a supercritical fluid–liquid–solid growth (SFLS), with a mixed organic solution of copper chloride (CuCl) and tri-noctylphosphine (TOP) as precursor, and bismuth precursor as the metal seed source. The prepared CuP_2 nanowires presented a high aspect ratio and exhibited a single monoclinic CuP_2 crystal structure with no impurity phase. Serving for LIB anode, CuP_2 nanowires provided a reversible capacity of 945 mA h/g at 85.29 mA/g over 100 cycles. Even at 5117.46 mA/g, an outstanding capacity of 600 mA h/g was still displayed. Such stable cycling performance and excellent rate
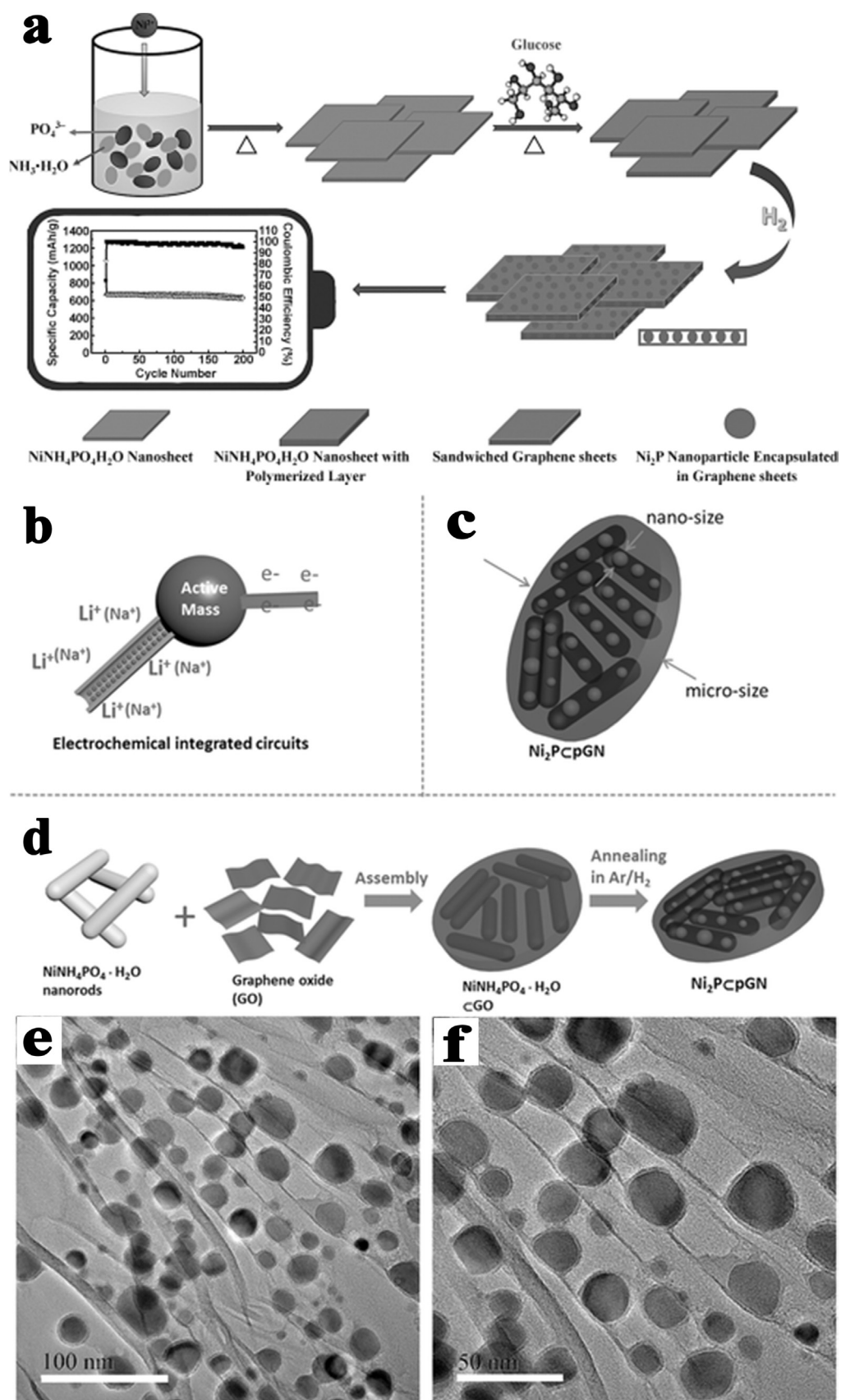
Fig. 20. (a) Schematic illustration of the synthetic process of the sandwiched Ni$_2$P nanoparticles encapsulated in coupled graphene sheets. (Reproduced with permission. Copyright 2015, Wiley-VCH Verlag GmbH & Co. KGaA [106]) Schematic diagrams of (b) electrochemically integrated circuit around the active mass and (c) 3D yolk–shell-like architecture. (d) Schematic illustration of the fabrication process for Ni$_2$P⊂pGN, involving an assembly step of precursors and the following annealing step. (e, f) TEM of Ni$_2$P⊂pGN. (Reproduced with permission. Copyright 2017, Wiley-VCH Verlag GmbH & Co. KGaA [107]).
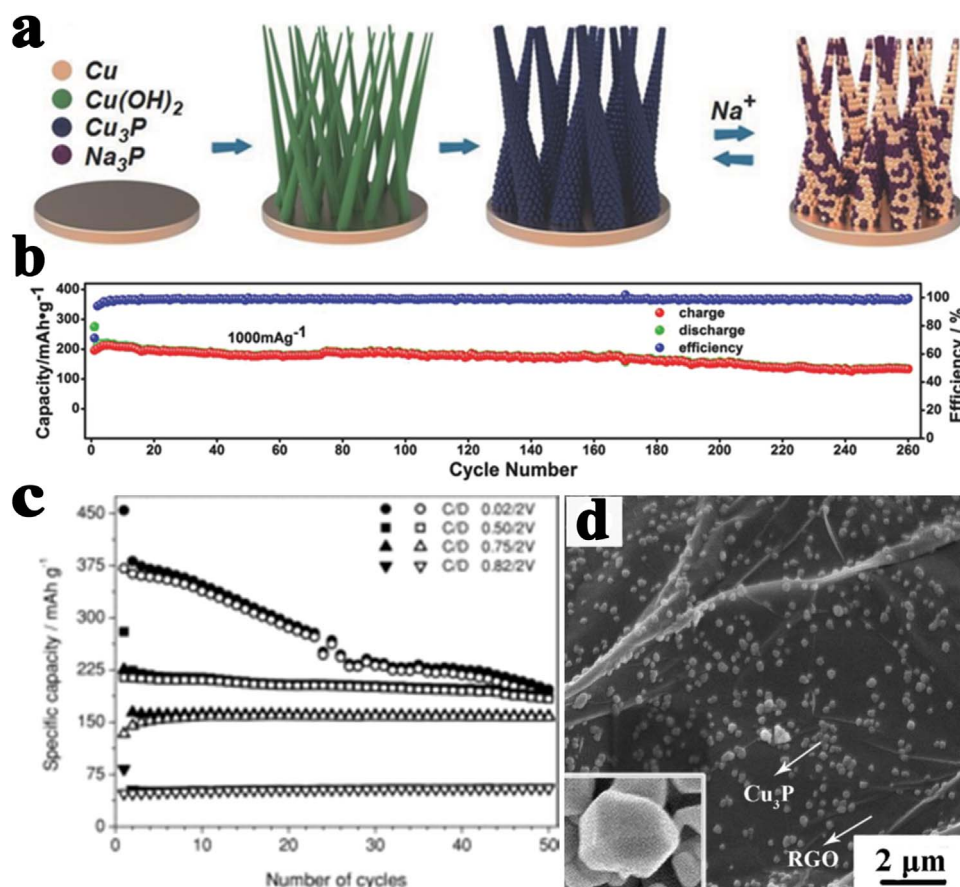
Fig. 21. (a) Schematic representation of the synthesis, sodiation/desodiation process of CPNWs and (b) long cycling performance of CPNW electrode. (Reproduced with permission. Copyright 2016, Wiley-VCH Verlag GmbH & Co. KGaA [130]) (c) Cycling performance of the Cu_3P electrodes in Li-metal cells using the lower potential cut-off values indicated in the figure legend. (Reproduced with permission. Copyright 2013, Wiley-VCH Verlag GmbH & Co. KGaA [133]) (d) SEM of Cu_3P/RGO nanocomposite. (Reproduced with permission. Copyright 2016 Nature Publishing Group [134]).

capability were attributed to the metal phosphide conversion-type lithium storage mechanism, based on *ex-situ* TEM and CV tests [137]. Zhao et al. first investigated the preparation and evaluation of CuP_2 and carbon black (CuP_2/C) composites as a potential candidate anode for NIBs. After ball milling, the crystalline CuP_2 was coated with carbon black nanoparticles on the surface. With the carbon coating, the CuP_2/C showed a large capacity in excess of 500 mA h/g, remarkable rate capability and stable short-term cycling performance, based on conversion mechanism [138]. Kim et al. further improved the cycling stability of CuP_2/C and achieved a high tap density of ~ 1.2 g/cm^3 through chemical bonding between CuP_2 and carbon network using high-energy ball milling. Due to conductive carbon network and stable P-O-C chemical bonding, the hybrid electrode exhibited excellent cycle stability (> 450 mAh/g at 50 mA/g with nearly 100% capacity retention up to 100 cycles) and a high rate capability (64% desodiation capacity showed at 800 mA/g) [139].

2.2.7. Fe-P phosphides

Iron forms different metal phosphides like Fe_2P, FeP, FeP_2 and FeP_4, depending on the phosphorus content and operating temperatures [141]. As anode materials for LIBs/NIBs, FeP_2 was first reported by Silva et al., who suggested that upon discharge, a metastable and nanostructured Fe_xP-Li_yP-Fe_x was formed through an insertion process, instead of a conversion reaction process [142]. Then Boyanov et al. investigated FeP and revealed a complex lithium reaction mechanism, i.e., in the first discharge, Li_3P and Fe metal were formed as the product through a direct conversion. During the subsequent discharge/charge process, the reaction mechanism combined the conversion and insertion/extraction reaction. The inser-

tion/extraction reaction corresponded to the formation/destructuration of an intermediate tetragonal LiFeP phase, which was highly reversible, resulting in high capacity retention of 300 mA h/g over 100 cycles [143]. Considering the high capacity of FeP, even higher capacities can be expected for FeP_x when x was increased from 1 to 4. The electrochemical behavior of FeP_x was compared by the same authors. The study of the reactivity of Li versus FeP_x (x = 0.33, 0.5, 1, 2 and 4) had clearly suggested that the Fe/P ratio, structure, electronic properties played important roles in influencing their performance. The phosphorus-rich iron phosphide phases exhibited faster reaction kinetics with lithium. The lithium reaction process of iron phosphides with different stoichiometries was different. For FeP and FeP_2, Li_xFeP and FeP as the intermediate phases were produced during cycling, and then were fully or partially converted to Li_3P and Fe as the final phase. However, the mechanism of FeP_4 was an insertion/extraction process with no conversion reaction to Li_3P/Fe [144].

Subsequently, various Fe-P phosphide-based nanomaterials were explored to improve their electrochemical performances as LIB/NIB anodes [145–156]. Amorphous structured Fe-P phosphides was an optional strategy to buffer volume changes and prevent degradation processes during the cycling. Hall et al. reported an amorphous FeP_2 which was synthesized by reacting $Fe(N(SiMe_3)_2)_3$ with PH_3 intetrahydrofuran (THF) at 100 °C (Fig. 22**a**). Due to the nanostructural and amorphous properties of the FeP_2, a high reversible capacity of 906 mA h/g after 10 cycles at 137 mA/g was delivered, corresponding to 66% of the theoretical capacity [145]. However, the electrochemical performances of Fe-P phosphides were still limited by their low electrical conductivity.
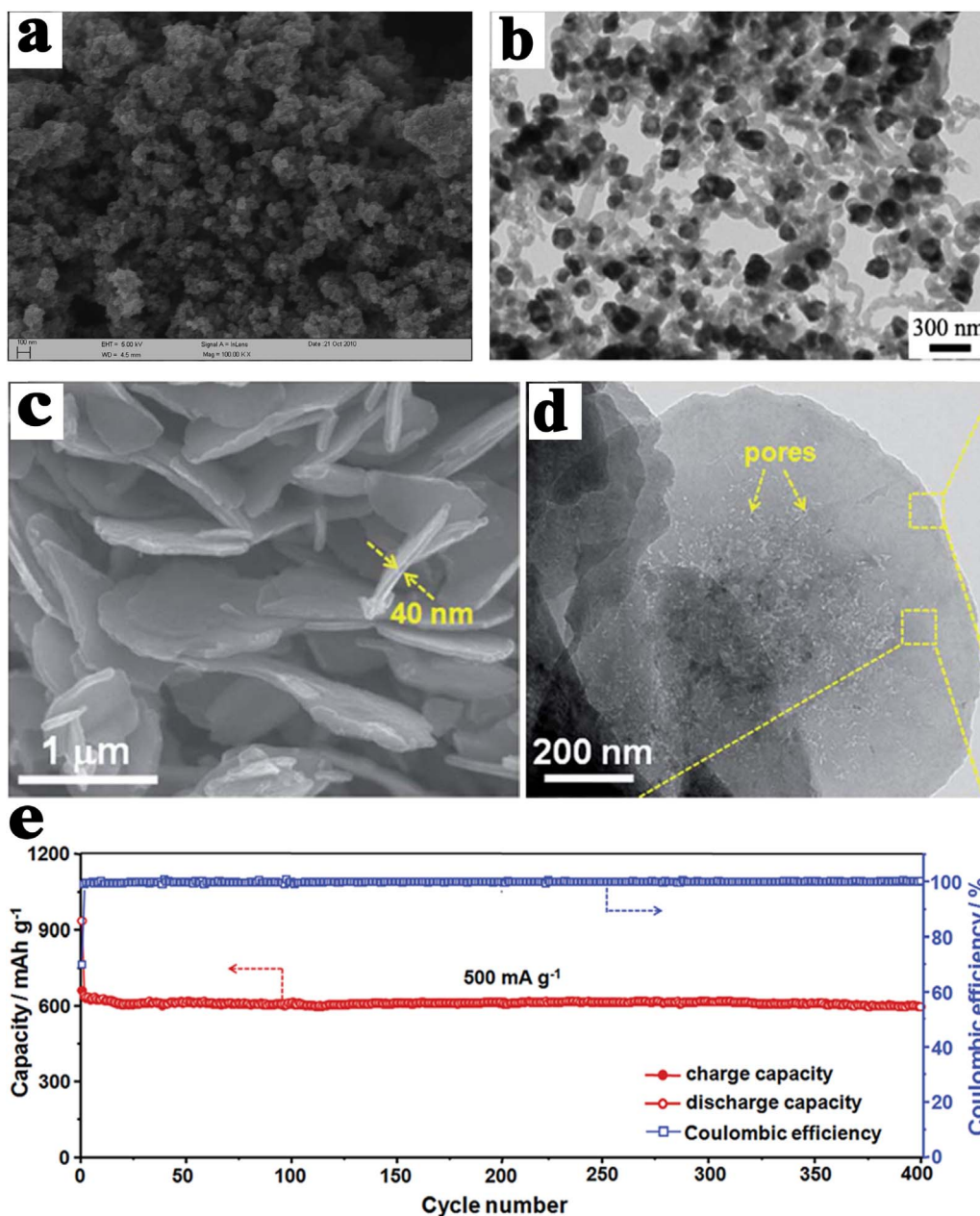
Fig. 22. (a) SEM image of amorphous FeP₂. (Reproduced with permission. Copyright 2012, American Chemical Society [145]) (b) TEM images for the annealed FeP₂/C nanohybrids. (Reproduced with permission. Copyright 2015, ScienceDirect [146]) (c) TEM and (d) HRTEM images of FeP@C nanoplates. (e) Long cycle performance of FeP@C nanoplates. (Reproduced with permission. Copyright 2016, the Royal Society of Chemistry [148]).

Compositing with carbon materials is a conventional but efficient way to improve the electrochemical performance of the Fe-P compound. Jiang et al. synthesized phosphorus-rich phase iron disphosphide/carbon tube (FeP₂/C) nanohybrids via a pyrolysis process (Fig. 22b). Due to the addition of carbon nanotube, the FeP₂/C nanohybrids showed improved electrochemical performance, delivering a discharge capacity of 435 mA h/g after 100 cycles at 137 mA/g [146]. Yang et al. synthesized FeP/graphite composite as anode for NIBs using a low energy ball-milling method. Assigned to compositing with graphite, the cycling performance was improved significantly, with 58% capacity retention after 70 cycles, and the FeP/graphite composite could still deliver a capacity of 134 mA h/g, even at a higher current density of 500 mA/g, which was more than twice the capacity of the FeP compound alone [147].

The electrochemical performances of Fe-P phosphides could be further improved by combining the nanostructure with carbon coating simultaneously. Han et al. synthesized porous FeP nanoplates with

carbon-coating (FeP@C) via a hydrothermal reaction followed by carbon coating process and phosphidation treatment (Fig. 22c & d). Benefiting from the plate-like nanostructure with abundant inner mesopores and carbon coating, the FeP@C nanoplates showed a reversible specific capacity of 720 mA h/g and kept at 691.2 mA h/g after 100 cycles at 200 mA/g. When increasing current density to 500 mA/g, it still delivered a stable capacity of 610 mA h/g after 400 cycles with negligible capacity fading (Fig. 22e). Furthermore, the superior rate capability of 347 mA h/g at 5000 mA/g was also obtained [148].

2.2.8. Co-P phosphides

Cobalt phosphides exist in a wide range of stoichiometries compositions, such as Co_2P, CoP, CoP_2 and CoP_3 [157–170]. As anode materials for LIBs, CoP_3 was first reported by Alcántara et al. [158] and Pralong et al. [159] simultaneously. Alcántara et al. investigated the reaction mechanism of CoP_3 using XRD, ⁷Li NMR and XAS

demonstrated that CoP_3 was converted to Co and Li_3P during the first discharge, and then Li_3P was formed from phosphorus during the subsequent cycles [158]. Pralong et al. revealed the reaction mechanism of CoP_3 via a combination of XRD, electron microscopy, potentiodynamic and galvanostatic intermittent measurements as well as XPS. They proposed that after the initial lithium insertion into the CoP_3 phase, Co nanoclusters were formed and highly dispersed on the Li_3P matrix; while upon charging, the Li_3P matrix was converted to LiP nanoparticles and the oxidation state of Co had little change [159]. Cui et al. first investigated CoP as an anode material for LIBs, and revealed that CoP was fully decomposed to Co and Li_3P after discharging to 0.1 V and CoP nanocrystalline structure was reformed after recharging to 3.0 V through *ex-situ* TEM and SAED, demonstrating a fully reversible conversion reaction mechanism for CoP [161]. López et al. first studied the electrochemical property of Co_2P as an anode material for rechargeable batteries and demonstrated that during the first discharge, Co and Li_3P were formed through conversion reaction mechanism. During the following recharge and all successive discharge/charge cycles, a redox reaction between Li_3P and LiP was demonstrated [162].

With the great progress in nanotechnology, tremendous efforts have been devoted to improving the electrochemical performances of cobalt phosphides [163–168]. One attractive approach is constructing nanostructured materials with controlled morphologies (e.g., nanotubes, nanorods, and hollow spheres). Yang et al. synthesized different nanostructured CoP and Co_2P (e.g., particles, rods, hollow spheres, and solid spheres) using Co-TOP complex as the precursor and oleylamine (OAm) served as surfactant, and systematically compared the electrochemical performance of different nanostructures and phases as anode materials for LIBs (Fig. 23**a**−**c**). The results showed that Li storage performances of cobalt phosphides could be enhanced through the shape or microstructure control. Specifically for the CoP hollow nanoparticles, a discharge capacity of 630 mA h/g was delivered after 100 cycles at 178.8 mA/g and a reversible discharge capacity of 256 mA h/g was still presented even at 4470 mA/g [163].
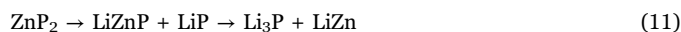
However, due to their intrinsically low electronic conductivity, practical application of cobalt phosphides is still a challenge. Generally, the electronic conductivity and lithium/sodium storage performance can be enhanced through hybridizing cobalt phosphides with carbonaceous materials, e.g. carbon network/shell. Yang et al. fabricated CoP nanowires/reduced graphene oxide (CoP/RGO) composite via a combination of hydrothermal reaction and calcinations. With the conductive graphene, the CoP/RGO displayed high specific capacity and excellent cycling stability. Impressively, high reversible capacities up to 960 mA h/g at 200 mA/g over 200 cycles and 297 mA h/g after 10,000 cycles at 20 A/g were achieved [166]. Recently, Zhu et al. synthesized ultrafine CoP nanoparticles embedded in nitrogen-doped carbon matrix, which derived from zeolitic imidazolate framework 67 (ZIF-67) templates (Fig. 23**d**−**f**). Owing to their unique architecture characteristics, a superior specific capacity of 522.6 mA h/g after 750 cycles at a current density of 200 mA/g and outstanding cycling stability up to 2000 cycles at a high current density of 500 mA/g were achieved [167].

CoP used for NIB anode was investigated by Chou's group, who demonstrated that CoP showed a large initial capacity of 770 mA h/g with lower voltage polarization. *Ex-situ* XPS and STEM characterization demonstrated a reversible conversion reaction mechanism between P and Na_3P [169]. Then Ge et al. synthesized core/shell structured CoP@C polyhedrons anchored on 3D reduced graphene oxide (CoP@C-RGO). The core/shell structured CoP@C polyhedrons were derived from metal-organic framework (MOF) and the hybrid of CoP@C-RGO was on nickel foam (NF) used as binder-free NIB anode (Fig. 23**g**). Owning to the unique structure and synergistic effects, the CoP@C-RGO-NF binder-free anode showed a specific capacity of 473.1 mA h/g at 100 mA/g over 100 cycles [170].
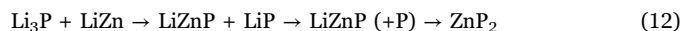
2.2.9. Other phosphides

Besides the metal phosphides mentioned above, several other metal phosphides have also been investigated as anode materials for LIBs/NIBs [171–189], including Zn-P phosphides [171–175], Ge-P phosphides [176–178], Mo-P phosphides [179–182], SiP_2 [183], Se_4P_4 [184], GaP [185], InP [186–188] and so on.

Bichat et al. [171,172] and Kishore et al. [173] initially investigated the electrochemical reaction of tetragonal ZnP_2 with Li. The Li insertion into the ZnP_2 electrode included two different but parallel processes based on *ex-situ* XRD: one involved only phosphide phases (Zn_3P_2, LiZnP, Li_4ZnP_2 and Li_3P); the second one implied exclusively Li-Zn alloys (Zn, $LiZn_4$ and LiZn). Monoclinic ZnP_2 and tetragonal ZnP_2 electrodes were also reported as anodes for LIBs. Hwang et al. reported the electrochemical behavior of the monoclinic ZnP_2 electrode and demonstrated that successive of $Li_{2.67}ZnP_2$-LiP, LiP_5, Zn-LiZnP phases were formed during the discharge process [174]. The electrochemical performance of the tetragonal ZnP_2 was investigated using a ZnP_2/C nanocomposite electrode, delivering a discharge capacity of 1340 mA h/g, with the initial Coulombic efficiency of about 83%. The tetragonal ZnP_2 presented a Li reaction mechanism as follows. During the first discharge:

$$ZnP_2 \rightarrow LiZnP + LiP \rightarrow Li_3P + LiZn \tag{11}$$

During the first charge:

$$Li_3P + LiZn \rightarrow LiZnP + LiP \rightarrow LiZnP (+P) \rightarrow ZnP_2 \tag{12}$$

The ZnP_2/C nanocomposite electrode also exhibited good cyclabiliy (about 350 mA h/g over 100 cycles) and high rate capability within the limited voltage range [175].

GeP_5, with a layered structure, promises bonding feasibility with a graphitic layer. Its conductivity is similar to that of graphite and 10000 times higher than that of black phosphorus. When used as an anode material, GeP_5 delivered a large specific capacity of 2406 mA h/g at 200 mA/g, with an initial Coulombic efficiency of 95%. By further compositing GeP_5 with conductive carbon, the cycle and rate performances of GeP_5 were notably improved, e.g., a capacity of 2127 mA h/g at a high current density of 5 A/g and a stable cyclability of 2300 mA h/g after 40 cycles at 200 mA/g [176]. It was suggested that the enhanced performance of the GeP_5/C composite may result from the effective combination between GeP_5 and carbon layers. The carbon layers provided not only an integrated continuous conductive network but also good structural flexibility to buffer the volume changes during Li^+ insertion/extraction. Recently, the same group investigated the electrochemical Na storage behaviors of GeP_5 and demonstrated that it promised a theoretically capacity of 1888 mA h/g or 6891 mA h/cm^3 with a low average redox potential of 0.4 V (vs.Na^+/Na) as NIB anode. After compositing with carbon, GeP_5/C showed a large capacity of 1250 mAh/g combined with a high initial Coulombic efficiency of 93%, excellent cyclability and a considerable rate performance of 900 mA h/g even at 1.5 A/g [177]. Almost at the same time, Qi et al. prepared a layer-structured GeP_3/C nanocomposite by a facile and large-scale ball milling method via an *in-situ* mechanical reaction. With the P-O-C bonds formed in the composite, the GeP_3/C anode showed stable cyclability of ~ 1109 mA h/g over 130 cycles at 100 mA/g. Even at high current densities of 2 and 5 A/g, it still presented high reversible capacities of 590 and 425 mA h/g, respectively [178].

Kim et al. fabricated MoP_2 nanoparticles clusters made up of dispersed nanoparticles with size ~ 10 nm through a mechanochemical method. Between 0 and 1.5 V, the MoP_2 nanoparticles clusters delivered an initial discharge capacity of 817 with Coulombic efficiency of 88% and capacity retention of 93% after 60 cycles. No decomposition of MoP_2 to other phases was demonstrated via X-ray absorption spectroscopy, *ex-situ* TEM and XRD. When increasing the cut-off voltage to 2.0 V, the capacity decreased rapidly after 10 cycles, demonstrating that MoP_2 was converted into Mo and Li_nP [179]. Then Wang et al. synthesized a novel
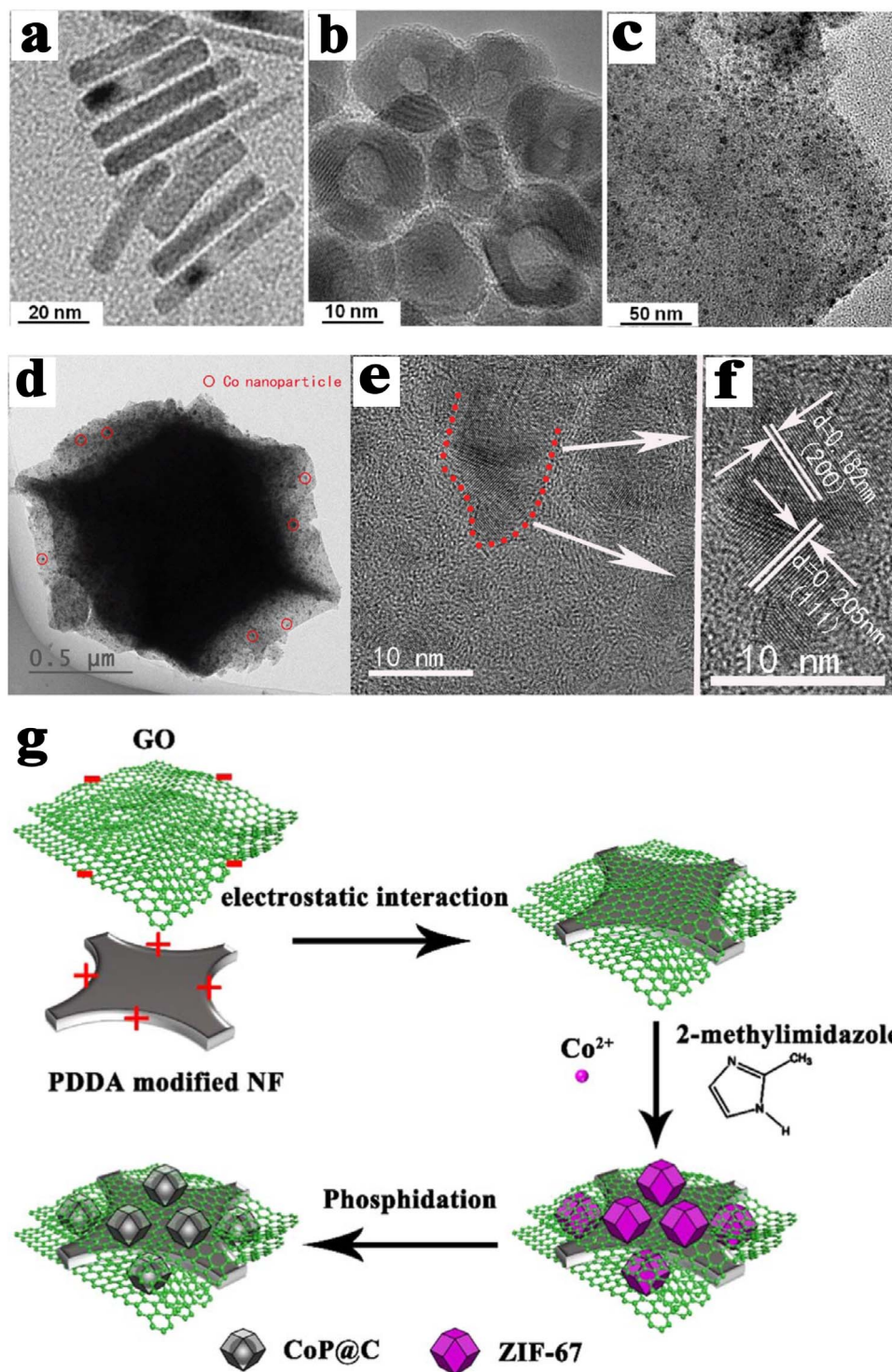
Fig. 23. TEM images of (a) Co$_2$P nanorods; (b) CoP hollow nanoparticles; (c) fine CoP nanoparticles. (Reproduced with permission. Copyright 2013, American Chemical Society [163]) (d) TEM, (e) HRTEM and (f) magnified HRTEM images of CoP. (Reproduced with permission. Copyright 2017, Wiley-VCH Verlag GmbH & Co. KGaA [167]) (g) Schematic illustration of the synthesis process of CoP@C-RGO-NF. (Reproduced with permission. Copyright 2016 ScienceDirect [170]).

molybdenum phosphide@carbon hybrid with a three-dimensional interconnected ordered porous structure (3D porous MoP@C hybrid) via a combination of a template sol-gel and an annealing treatment. The 3D porous MoP@C hybrid presented excellent cyclability with a high reversible capacity up to 1028 mA h/g at a current density of 100 mA/g over 100 cycles. The reaction mechanism of the 3D porous MoP@C hybrid was demonstrated to be a Li-intercalation reaction (MoP + xLi$^+$ + e$^-$ ↔ Li$_x$MoP), based on *ex-situ* XRD, HRTEM, SAED and XPS analyses and *ab initio* calculations [182].

Duveau et al. first prepared SiP$_2$ through a facile ball milling method, and demonstrated that the dense SiP$_2$ delivered outstanding capacities up to 1000 mA h/g after 30 cycles as LIB anode and 572 mA h/g over 15 cycles as NIB anode, respectively [183]. Se$_4$P$_4$ was recently reported as a new and promising candidate for NIB anode, because of its good electrical conductivity and high theoretical capacity. The Se$_4$P$_4$ material with amorphous structure was prepared by a simple mechanical milling method, delivering a high reversible capacity of 1048 mA h/g at 50 mA/g with excellent cyclability (804 mA h/g after 60 cycles).

Moreover, a reversible capacity of 724 mA h/g at 500 mA/g was achieved and 332 mA h/g was still maintained even at 3000 mA/g. Based on XRD, Raman spectroscopy, MAS-NMR, infrared spectroscopy, SEM, TEM and electrochemical measurements, the reaction mechanism of $Se_4P_4 + 20Na^+ + 20e^- \leftrightarrow 4Na_3P + 4Na_2Se$ during sodiation/desodiation was confirmed [184]. Hwang et al. prepared GaP nanoparticles (< 30 nm) with the reduction of sodium naphthalenide, and investigated its Li reaction behavior at the range of 1.5 and 0 V. During the first discharge, lithium inserted into GaP, forming Li_2GaP and electrochemically inactive Li_nP_7 phases. Li_2GaP decomposed to Li_xGa and irreversible Li_nP phases below 0.36 V. Only the reaction of Ga with lithium was reversible for GaP, contributing to the reversible capacity (~ 800 mA h/g) [185]. Cui et al. first investigated the electrochemical performance of InP thin film by pulsed laser deposition (PLD). They demonstrated that the nanostructured InP thin film electrode showed a high reversible capacity around 620 mA h/g with low potential and revealed a reversible electrochemical lithium reaction mechanism of InP due to its reversible crystalline structure through *ex-situ* XRD and XPS measurements [186]. Then Gerngross et al. reported the electrochemical and photochemical fabrication of a single-crystalline porous InP anode for LIBs. The InP anode consisted only of active material and a thin Au layer as a current collector, displaying a high area capacity of ~ 63 mA h/cm^2 and capacity of ~ 800 mA h/g. By adjusting the InP membrane thickness, the total anode capacity could be freely scalable [187].

3. Methods for composition

In the above sections, we have discussed various strategies for improving phosphorus based anodes, namely, compositing phosphorus with carbon materials of different architectures and developing varieties of metal phosphides or metal phosphide-carbon composites. Here, different synthesis methods involved in preparing the phosphorus-carbon composites and metal phosphides will be summarized (as listed in Table 1).

3.1. Methods for phosphorus carbon composites

Currently, ball-milling and vaporization-condensation are the most commonly developed methods to prepare phosphorus carbon anodes for LIBs and NIBs. There are also other methods employed to prepare phosphorus carbon anodes in a few papers.

3.1.1. Ball milling

The ball milling method was first adopted to prepare phosphorus carbon composites by mixing phosphorus and carbon materials under Ar atmosphere [19,25,36]. During the milling process, the bulk phosphorus particles are milled into small particles and dispersed well into carbon materials with the formation of phosphorus-carbon (P-C) [31,41] or phosphorus-oxide-carbon (P-O-C) bonds [44,53]. Many phosphorus-carbon composite anodes like red phosphorus-carbon black [25,36], red phosphorus-graphite [41], red phosphorus-carbon nanotube [44], red phosphorus-graphene [53], black phosphorus-carbon black [19], black phosphorus-ketjenblack [45], black phosphorus-graphite [40], are synthesized through high energy ball milling (Fig. 24**a**). Ball milling method is simple and productive, and can control the ratio of phosphorus in the composite materials precisely. However, the particle size of phosphorus is still not small enough and the particles are easy to aggregate after high energy ball milling. Both of them adversely affect the rate and cycling performance of the electrodes.

3.1.2. Vaporization–condensation

The vaporization-condensation strategy has been demonstrated to be more effective in enhancing the electrochemical performance of phosphorus, which takes advantage of the sublimation of red phos-

Summary of representative composition methods for phosphorus based anodes.

Composites	Methods	Phosphorus size	Temp.	Advantages	Disadvantages	Ref
Phosphorus-carbon	Ball milling	μm	r.t.[a]	Formation of P-C bond, simple and productive, phosphorus content controllable	Larger particles, poor cyclability	[19,25,31,33–36,38,39,42–45,51]
	Vaporization-condensation	nm to μm	400–600 °C	Smaller particles, excellent cyclability	Not safe	[41,46,47,53,54,63–65,72]
	Others	nm to μm	Variable	Good performance	No universal	[32,52,57,58,188]
Metal phosphides	Ball milling	μm	r.t.	Scaled up for mass production	Difficult to control the morphology	[76–80,83,88,89,94–96,100–103,106,130,139,141,142,144,145,153,159–161,166,175,177,181–186]
	Temperature-programmed reduction	nm to μm	150–1000 °C	Effective and favorable route to synthesize metal phosphides with various nanostructures	Toxic and highly corrosive, and easy to explode	[104,105,112–115,124,126,137,152,154,156,160,164,165,170–173,176,189]
	Organometallic synthesis	nm to μm	220–385 °C	Size-controllable route to prepare nanostructured metal phosphides with good uniformity and crystallinity	Sophisticated and highly toxic	[99,111,112,117–123,125,143,169,174]
	Solvothermal/hydrothermal	nm to μm	100–250 °C	Green and low temperature	Large polydispersity in crystallite sizes	[92,93,97,98,116,135,140]

[a] In general, room temperature (r.t.) refers to 25 °C.
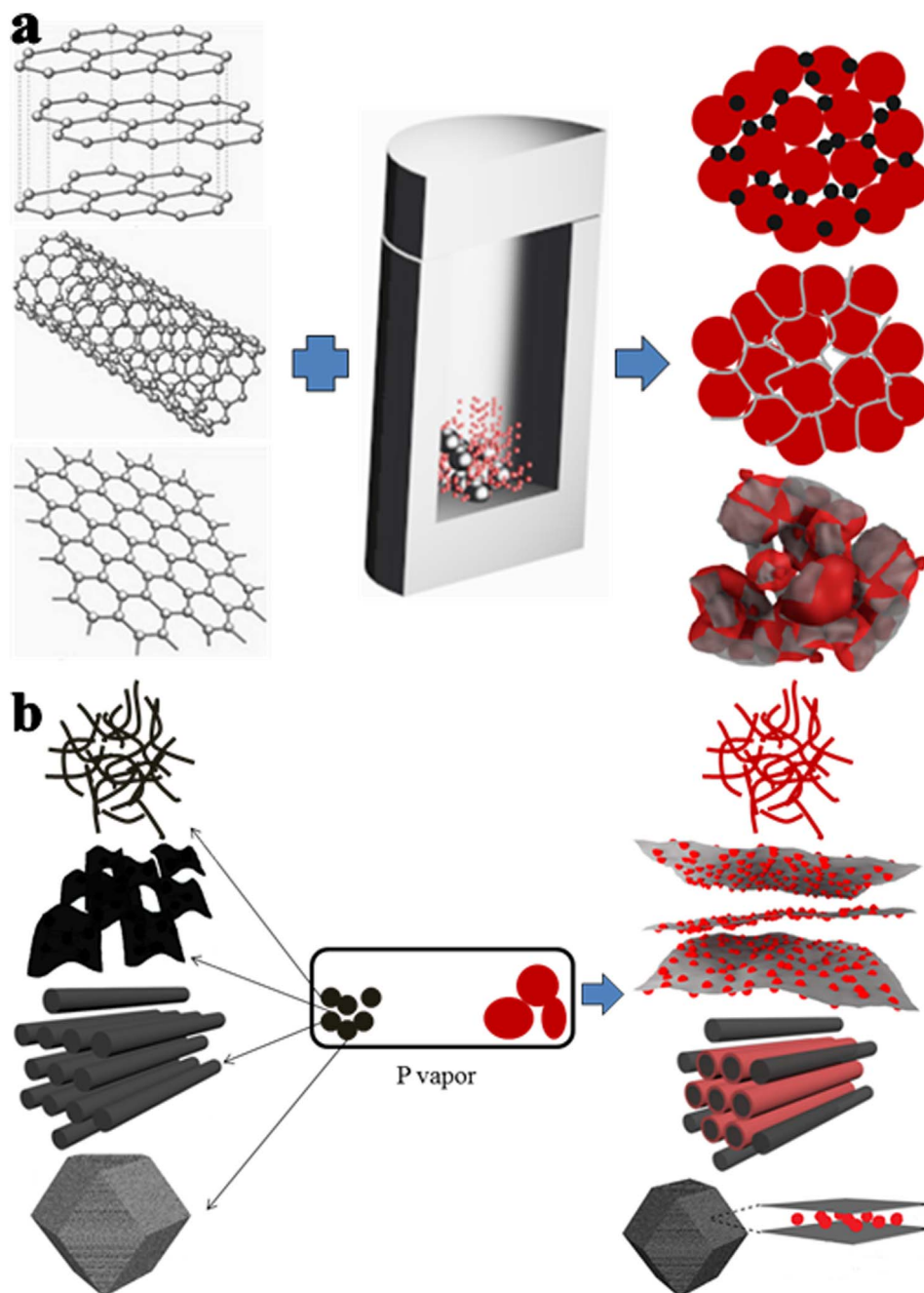
Fig. 24. Schematic illustration of the (a) ball milling and (b) vaporization-condensation process of phosphorus with different carbon materials.

phorus and conversion between white phosphorus and red phosphorus [65]. When the bulk red phosphorus is heated above the sublimation temperature (400–600 °C under Ar atmosphere or vacuum), the phosphorus sublimate diffuses into the pores due to capillary forces and pressure differences, whereupon it is adsorbed and deposited on the internal and external surface of the carbon host materials. Afterward, the condensate is converted to red phosphorus nanoparticles at conversion temperature (260–280 °C under Ar atmosphere or vacuum). When under vacuum condition, higher temperature (600 °C) is used, which creates large driving force for phosphorus vapor and enhances the loading ratio of phosphorus [43]. Vaporization-condensation strategy is adaptable for a large variety of carbon materials, such as nanotubes [43], nanofibers [48,49], graphene [56], graphene paper [55] and porous carbon [65–67] with pore volume spanning from micrometers to nanometers, even molecular level (Fig. 24b). The

composite prepared by vaporization-condensation presents high capacity, excellent rate capability, and stable cyclability. However, the loading ratio of phosphorus in the composite materials prepared by the vaporization-condensation method is typically low and difficult to control precisely, and more safety considerations are also brought about by the vaporization-condensation method, both of which are unfavorable for the practical application.

3.1.3. Other methods

There are some researchers who adopt other methods to prepare phosphorus-carbon composites. For red phosphorus-carbon composites, co-freeze-drying of nano-sized phosphorus and exfoliated graphene oxide sheets (P-GO) [54] and carbothermic reduction of P_4O_{10} into red phosphorus [68] are used. For phosphorene-graphene hybrids, self-assembly of phosphorene and graphene in N-methyl-2-pyrrolidone

(NMP) solution [59] and spark plasma sintering [60] are applied. Recently, a solution-phase method to synthesize red phosphorus nanoparticles [34] and a wet solvothermal approach to fabricate hollow phosphorus nanospheres with porous shell [190] were reported. All the methods above have their own advantages and can improve the electrochemical performance of phosphorus based anodes to some extent. However, each of these methods also has its limits, for example, the co-assembly of P-GO has the similar disadvantage to ball-milling, and the process is comparably complex; the carbothermic reduction method needs high temperature and brings about safety considerations like vaporization-condensation method; the self-assembly method may be limited to phosphorene and graphene; while the chemical reagents used in the solution-phase approach and wet solvothermal method are highly explosive and toxic.

3.2. Methods for metal phosphides

For metal phosphides, the synthetic methods are relative more than that of phosphorus-carbon composites. The most commonly used methods to prepare metal phosphide anodes for LIBs/NIBs are high energy ball milling, temperature-programmed reduction, organometallic synthesis and solvothermal/hydrothermal.

3.2.1. High energy ball milling

High energy ball milling is a facile way to synthesize high purity metal phosphides, owning to its starting from elemental metal and phosphorus powders. The precursors undergo intense impacts and collisions generated by balls in a high speed rotated and sealed steel container, thereby allowing chemical reactions to take place with high temperature and pressure established in the space between the balls and the precursors. Almost all metal phosphides (MP$_y$, M = V [76–78], Sn [85,86,91–93,97], Ni [100], Cu [124,133,135,136,138,139], Fe [147,153,155], Co [160,169], Zn [171,172,175], Ge [176–178], Mo [179], Si [183], Se [184], Ga [185] and In [186–188]) were synthesized through high energy ball milling. Due to its simplicity and high efficiency, high energy ball milling was usually adopted to fabricate the metal phosphides which were first investigated as anodes for LIBs/NIBs [78,81,85,91,92,100,124,147,160,176,179,183–186]. Easy to scale up for mass production is a major benefit of the high energy ball milling technique. However, controlling the morphology of the products is difficult, and the rate performance and long-term stability still remain issues for the metal phosphides prepared by this technique.

3.2.2. Temperature-programmed reduction

Temperature-programmed reduction (TPR) is a solid-gas technique for synthesizing materials. During the process, a reducing gas mixture is flowed over an oxidized precursor while the temperature rises according to program. The TPR method is a widely applied method to prepare metal phosphide anodes [98,99,106–109,120,130,131,148,150,154,158,159,164–167,170,191]. When synthesizing metal phosphides via TPR, there are mainly three reducing gases, including phosphorus vapor, H$_2$ and PH$_3$.

When phosphorus vapor, sourced from red/white phosphorus, is used as the reducing gases, metal phosphides are synthesized by mixing the stoichiometric metal and red phosphorus solids in the sealed atmosphere at extremely high temperature through long-term annealing (e.g., 800 °C for 14 days in the case of NiP$_3$ [191], 900 °C for 5 days in the case of NiP$_2$ [98]). In a sense, high purity metal phosphides could be provided by element phosphorus due to its independent phosphorus source for phosphidation. Besides, both metal-rich (e.g., Cu$_3$P nanorods [131]) and phosphorus-rich phosphides (e.g., cubic NiP$_2$ nanoparticles [99], NiP$_3$ [191], CoP$_3$ [158,159]) could be obtained with high yield, by changing the synthesis conditions (phosphorus molar ratio, temperature, etc.) (Fig. 25). However, due to the harsh conditions (extreme high temperature and too long calcinations time), the use of element phosphorus is less concerned.

Metal phosphides can also be prepared by reducing metal salts and phosphorus compound in H$_2$ at elevated temperature. In flowing hydrogen, the reduction of metal salts and phosphate occurs between 400 and 1000 °C, completed within a few hours. Due to its strong P-O bond, the reduction of phosphate requires high temperature. The reduction process can be explained as follow: once metal particles have formed, hydrogen molecules can be dissociated to hydrogen atoms, then the hydrogen atoms spill over to the phosphate and reduce it to phosphorus or phosphine. These phosphorus species react with the metal to form a metal phosphide. The reduction of inorganic phosphorus, i.e. phosphate, in H$_2$ is a facile and safer route. Therefore, many metal phosphide composites for LIB/NIB applications , such as sandwiched Ni$_2$P nanoparticles encapsulated in coupled graphene sheets [106], 3D yolk-shell-like Ni$_2$P nanoparticles embedded into porous graphene networks [107], peapod-like composite with Ni$_2$P nanoparticles encapsulated in carbon fibers [108,109], peapod-like composite with Ni$_{12}$P$_5$ nanoparticles encapsulated in carbon fibers [120], Fe$_2$P/graphitized carbon yolk/shell octahedral [150] and Fe$_2$P nanoparticles enveloped in sandwichlike graphite carbon sheets [154], were prepared in this manner (Fig. 25). However, the crystal size of phosphides synthesized through the phosphate route is large in bulk form, due to the sintering at high temperature.

In addition to the two routes discussed above, the *in-situ* decomposition of hypophosphite is another accessible route to synthesize phosphides, where a metal source is reduced and phosphidated by PH$_3$ generated from hypophosphite disproportionation reaction. The hypophosphite route allows wide metal precursor options, and phosphides are produced via a more straightforward manner without sophisticated steps. Moreover, the hypophosphite route can preserve the morphology of the metal precursor well. Therefore, Metal phosphides with desired nanostructures can be achieved by using the relative metal precursor with the desired nanostructures, which is much easier to synthesize. A series of nanostructured phosphides, e.g., Cu$_3$P nanowire [130], FeP@C nanoplates [148], self-supported CoP nanorod arrays [164], mesoporous CoP nanorods [165], CoP nanowires [166], ultrafine CoP nanoparticles [167], CoP polyhedrons [170], etc., were realized through this route (Fig. 25). It should be paid much more attention that PH$_3$ is extremely toxic, highly corrosive and easy to explode.

TPR, especially the H$_2$ and PH$_3$ reduction routes, is an effective and favorable approach to realize good electrochemical performance of metal phosphide anodes, because various nanostructured metal phosphides and their composites with carbon materials can be realized by this method. However, additional works are still needed to tackle the issues above.

3.2.3. Organometallic synthesis

The preparation of nanoscale metal phosphides is not only limited to the solid-gas methods, liquid phase methods are also adopted commonly. Through the organometallic synthesis method, it is possible to control the phase, size and morphology of the metal phosphide particles, which are important properties for LIBs/NIBs [163]. Usually a low-valent metal complex is phosphidated at high temperature by an excess of a phosphorus compound, e.g., trioctylphosphine (TOP) or tris(trimethylsilyl)-phosphine (TMSP), in a high-boiling solvent such as trioctylphosphine oxide (TOPO). Besides allowing the samples to be annealed at moderate temperatures (T < 350 °C), the high-boiling TOPO solvent also functions as a coordinating capping ligand to prevent aggregation. In addition, secondary capping agents, e.g., oleylamine (OAm) or oleic acid (OA), are usually employed to control particle size and shape, and/or to alter the solubility and air sensitivity of the resultant particles. Phosphides with various nanostructures can also be obtained via phosphidating as-formed nanostructured metals using TOP as phosphorus source at temperature between 220 and 385 °C. Besides controlling particle size and shape, compositions controlling can also be achieved by changing the time/temperature of reaction between metal precursor and phosphorus compound. With
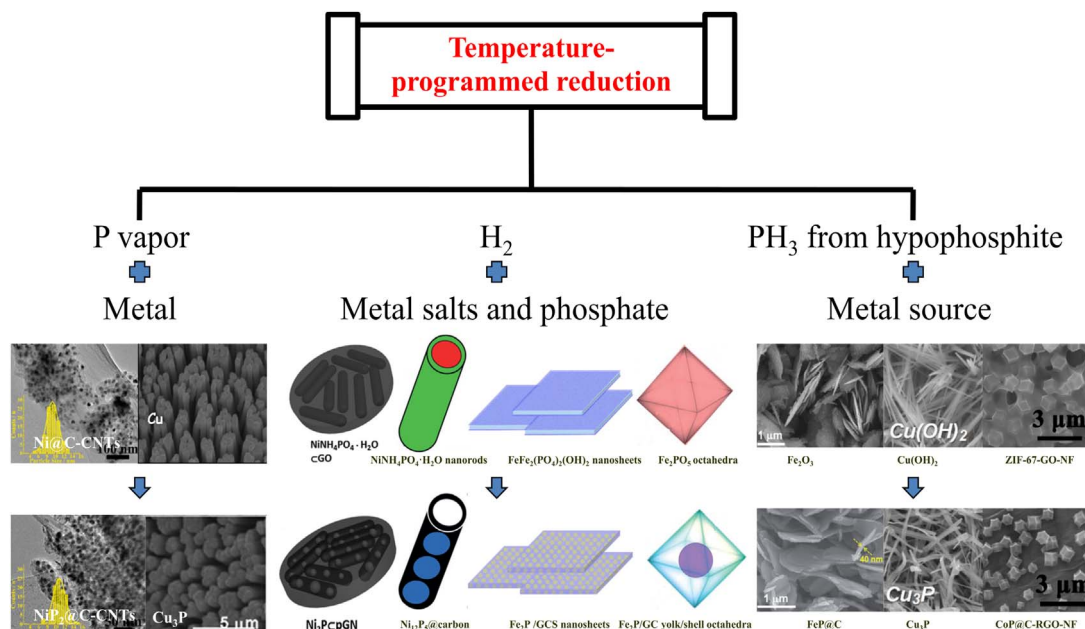
Fig. 25. Schematic illustration of the TPR process to synthesize metal phosphides through three routes.
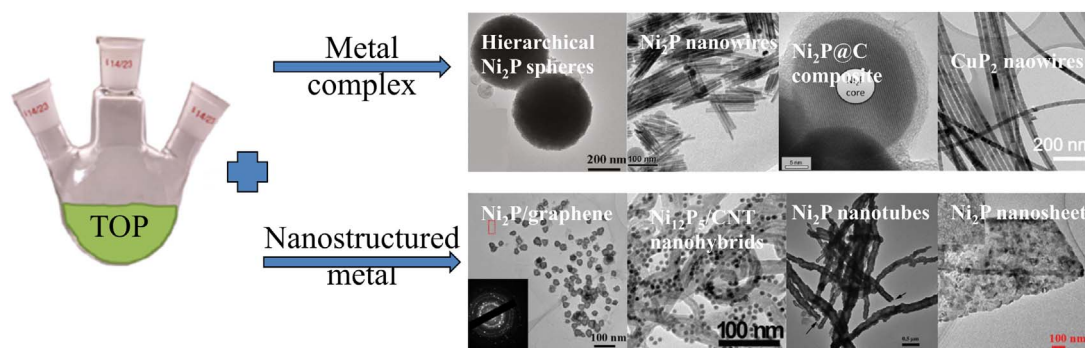

Fig. 26. Schematic illustration of the organometallic synthesis process using different metal sources.

shape, size and compositions controllable, many metal phosphide anodes with desired electrochemical performance, such as teardrop-shaped ultrafine $SnP_{0.94}$ [96], Ni_2P nanotubes [116], Ni_5P_4/C composite [117], hierarchical Ni_2P spheres [111], $Ni_2P@C$ composite [112], porous Ni_2P nanosheets [105], Ni_2P/graphene sheet composite [113], $Ni_{12}P_5$/CNT nanohybrids [119], Ni_2P nanowires [104], CuP_2 naowires [137], Co_xP nanostructures [163], were obtained (Fig. 26). However, the process of organophosphorus route is sophisticated, which is unfavorable for large scale production, and it also involves the highly toxic organic phosphine which can be pyrophoric when contacting with air.

3.2.4. Solvothermal/hydrothermal

The solvothermal/hydrothermal approach is a liquid phase method or liquid-solid phase method, which is commonly used to synthesize nanocrystalline metal phosphides. The reactions are conducted in a sealed Teflon-lined autoclave (autogeneous pressure), where a high pressure above normal atmospheric is created when temperatures are higher than the normal boiling point of the solvent. Such mild methods are ideal for producing metal phosphide nanoparticles, because the reaction temperatures are relatively low (< 250 °C). However, the nanoparticles appear the non-uniformed morphologies, and the crystallite sizes distributed from 1 nm to 200 nm. Another drawback is that highly reactive and toxic phosphide sources (i.e., Na_3P or P_4) are needed in general. Moreover, the nanoparticles produced through solvothermal/hydrothermal pathway are usually insoluble and aggre-

gated, so their size and physical-property are difficult to be evaluated. Due to the hurdles above, the solvothermal/hydrothermal method was rarely applied to prepare metal phosphide anodes for LIBs/NIBs. Until recently, uniform yolk-shell $Sn_4P_3@C$ nanospheres with high capacity and stable cyclability as NIB anode were synthesized via solvothermal method using yolk-shell $Sn@C$ nanospheres and red phosphorus as the precursor [92]. Then Sn_4P_3/reduced graphene oxide (RGO) hybrids as anodes for NIBs were synthesized through solvthermal method from Sn/RGO and red phosphorus [95]. In addition to the strategy of metal-carbon composites as the precursors, the issues of large polydispersity and aggregation can also be solved by addition of surfactant or carbon matrix, such as Cu_3P/reduced graphene oxide (RGO) with CTAB as surfactant and GO as carbon matrix (Fig. 27) [134]. What's more, the size and shape of metal phosphide nanoparticles can be better controlled through appropriate modification of the synthetic routes.

4. Conclusion and outlook

In this review, we have presented the great advance in phosphorus based anodes for LIBs and NIBs. Various strategies have been carried out to improve their performance, i.e., compositing phosphorus with variety of carbon materials , developing different metal phosphides or metal phosphide-carbon composites. These rational and creative designs are helpful to address the issues of poor electronic and ionic transport and volume expansion, thus significantly improving the capacity, cyclability and rate performance of phosphorus based anodes.
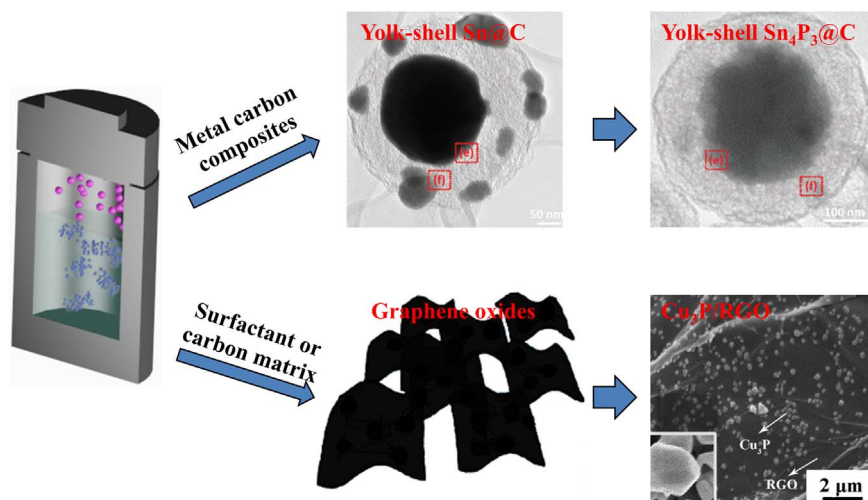
Fig. 27. Schematic illustration of the solvothermal/hydrothermal process via different strategies.

However, some significant challenges are still remaining.

First, many details of the electrochemical mechanisms for phosphorus based anodes are controversial and unclear. Especially metal phosphides used for NIBs, little is known about the electrochemical mechanisms, because their study is just emerging. Further studies, especially *in-situ* approaches, e.g., *in-situ* XRD and *in-situ* TEM, would be helpful to build a thorough understanding of reaction mechanisms and lead to an optimized design for the electrode. Besides further enhancement on the cycle life of phosphorus based anodes, the content of phosphorus in the whole electrode has yet to be solved. In most phosphorus-based anodes, the phosphorus content is very low. Because the active materials just account for 70–90% in weight in the whole electrodes while there is a large portion of conductive materials in phosphorus based composites. Enhancing phosphorus content in composite (> 70%) or constructing the self-supported anode free of additives can effectively raise the proportion of phosphorus in the whole electrode. Moreover, the low initial Coulombic efficiency in phosphorus based anodes is another important issue that needs to be taken into account for assembling full cells, and the investigation on enhancing the initial Coulombic efficiency of nanostructured phosphorus based anodes should focus on the atomic or molecular level by virtue of the modern analytical techniques. Finally, most of the currently available synthetic methodologies for the nanostructured phosphorus based anodes either bring about more safety considerations or use toxic sources, and some of synthetic methodologies have sophisticated process, which are only limited to the laboratory level and cannot meet the demand of large-scale and low cost commercial production. Although ball-milling technique is an easily scale-up method, the particle size of phosphorus based materials obtained by ball milling is not small enough, which results in their rate performance and long-term stability still remaining issues. More attentions should be focused on developing new approaches under mild synthetic conditions for performance improvement.

Although the road to viable energy storage devices based on phosphorus based materials is filled with significant challenges, great strides have been achieved over the last few years. By virtue of its abundance and attractive high capacity, it is clear that intensive studies of phosphorus based anodes toward high-performance will be going on, and their development will bring fundamental and technical breakthrough in the future.

Acknowledgements

References

[1] D. Kundu, E. Talaie, V. Duffort, L.F. Nazar, The emerging chemistry of sodium ion batteries for electrochemical energy storage, Angew. Chem. Int. Ed. 54 (2015) 3431–3448.

[2] D. Larcher, J.-M. Tarascon, Towards greener and more sustainable batteries for electrical energy storage, Nat. Chem. 7 (2015) 19–29.

[3] Crude Oil and Commodity Prices. ⟨http://www.oil-price.net/⟩. (Accessed March, 2016).

[4] J.M. Carrasco, L.G. Franquelo, J.T. Bialasiewicz, E. Galvan, R.C. Portillo Guisado, M.A.M. Prats, J.I. Leon, N. Moreno-Alfonso, Power-electronic systems for the grid integration of renewable energy sources: a survey, IEEE Trans. Ind. Electron. 53 (2006) 1002–1016.

[5] K.C. Divya, J. Østergaard, Battery energy storage technology for power systems-an overview, Electric Power Syst. Res. 79 (2009) 511–520.

[6] B. Dunn, H. Kamath, J.-M. Tarascon, Electrical energy storage for the grid: a battery of choices, Science 334 (2011) 928–935.

[7] S. Hameer, J.L. van Niekerk, A review of large-scale electrical energy storage, Int. J. Energy Res. 39 (2015) 1179–1195.

[8] S.W. Kim, D.H. Seo, X. Ma, G. Ceder, K. Kang, Electrode materials for rechargeable sodium-ion batteries: potential alternatives to current lithium-ion batteries, Adv. Energy Mater. 2 (2012) 710–721.

[9] H.L. Pan, Y.-S. Hu, L.Q. Chen, Room-temperature stationary sodium-ion batteries for large-scale electric energy storage, Energy Environ. Sci. 6 (2013) 2338–2360.

[10] B.L. Ellis, L.F. Nazar, Sodium and sodium-ion energy storage batteries, Curr. Opin. Solid State Mater. Sci. 16 (2012) 168–177.

[11] M. Hana, E. Gonzalo, G. Singh, T. Rojo, A comprehensive review of sodium layered oxides: powerful cathodes for Na-ion batteries, Energy Environ. Sci. 8 (2015) 81–102.

[12] X.X. Zuo, Y.G. Xia, Q. Ji, X. Gao, S.S. Yin, M.M. Wang, X.Y. Wang, B. Qiu, A.X. Wei, Z.C. Sun, Z.P. Liu, J. Zhu, Y.-J. Cheng, Self-templating construction of 3D hierarchical macro-/mesoporous silicon from 0D silica nanoparticles, ACS Nano 11 (2017) 889–899.

[13] J.L. Lang, B. Ding, T. Zhu, H.X. Su, H. Luo, L.H. Qi, K. Liu, K. Wang, N. Hussain, C.S. Zhao, X.Y. Li, H.J. Gao, H. Wu, Cycling of a lithium-ion battery with a silicon anode drives large mechanical actuation, Adv. Mater. 28 (2016) 10236–10243.

[14] T. Wang, J. Zhu, Y. Chen, H.G. Yang, Y. Qin, F. Li, Q.F. Cheng, X.Z. Yu, Z. Xu, B.G. Lu, Large-scale production of silicon nanoparticles@graphene embedded in nanotubes as ultra-robust battery anodes, J. Mater. Chem. A 5 (2017) 4809–4817.

[15] X.X. Zuo, J. Zhu, P. Müller-Buschbaum, Y.-J. Cheng, Silicon based lithium-ion battery anodes: a chronicle perspective review, Nano Energy 31 (2017) 113–143.

[16] C.-H. Lim, T.-Y. Huang, P.-S. Shao, J.-H. Chien, Y.-T. Weng, H.-F. Huang, B.J. Hwang, N.-L. Wu, Experimental study on sodiation of amorphous silicon for use as sodium-ion battery anode, Electrochim. Acta. 211 (2016) 265–272.

[17] S.C. Jung, D.S. Jung, J.W. Choi, Y.-K. Han, Atom-level understanding of the sodiation process in silicon anode material, J. Phys. Chem. Lett. 5 (2014) 1283–1288.

[18] O. Malyi, V.V. Kulish, T.L. Tan, S. Manzhos, A computational study of the insertion of Li, Na, and Mg atoms into Si(111) nanosheets, Nano Energy 2 (2013) 1149–1157.

[19] C.-M. Park, H.-J. Sohn, Black phosphorus and its composite for lithium rechargeable batteries, Adv. Mater. 19 (2007) 2465–2468.

[20] C. Marino, L. Boulet, P. Gaveau, B. Fraisse, L. Monconduit, Nanoconfined phosphorus in mesoporous carbon as an electrode for Li-ion batteries: performance and mechanism, J. Mater. Chem. 22 (2012) 22713–22720.

[21] M. Dahbi, N. Yabuuchi, M. Fukunishi, K. Kubota, K. Chihara, K. Takiwa, X.-F. Yu, H. Ushiyama, K. Yamashita, J.-Y. Son, Y.-T. Cui, H. Oji, S. Komaba, Black phosphorus as a high-capacity, high-capability negative electrode for sodium-ion batteries: investigation of the electrode/electrolyte interface, Chem. Mater. 28 (2016) 1625–1635.

[22] L.-Q. Sun, M.-J. Li, K. Sun, S.-H. Yu, R.-S. Wang, H.-M. Xie, Electrochemical activity of black phosphorus as an anode material for lithium-ion batteries, J. Phys. Chem. C 116 (2012) 14772–14779.

[23] M. Walter, R. Erni, M.V. Kovalenko, Inexpensive antimony nanocrystals and their composites with red phosphorus as high-performance anode materials for Na-ion batteries, Sci. Rep. 5 (2015) 8418–8425.

[24] J.M. Sangster, Na-P (sodium-phosphorus) system, J. Phase Equilib. Diffus. 31 (2010) 62–67.

[25] Y. Kim, Y. Park, A. Choi, N.S. Choi, J. Kim, J. Lee, J.H. Ryu, S.M. Oh, K.T. Lee, An amorphous red phosphorus/carbon composite as a promising anode material for sodium ion batteries, Adv. Mater. 25 (2013) 3045–3049.

[26] N. Nitta, D. Lei, H.R. Jung, D. Gordon, E. Zhao, G. Gresham, J. Cai, I. Luzinov, G. Yushin, Influence of binders, carbons, and solvents on the stability of phosphorus anodes for Li-ion batteries, ACS Appl. Mater. Interfaces 8 (2016) 25991–26001.

[27] N. Yabuuchi, Y. Matsuura, T. Ishikawa, S. Kuze, J.-Y. Son, Y.-T. Cui, H. Oji, S. Komaba, Phosphorus electrodes in sodium cells: small volume expansion by sodiation and the surface-stabilization mechanism in aprotic solvent, ChemElectroChem 1 (2014) 580–589.

[28] M. Li, R. Carter, L. Oakes, A. Douglas, N. Muralidharan, C.L. Pint, Role of carbon defects in the reversible alloying states of red phosphorus composite anodes for efficient sodium ion batteries, J. Mater. Chem. A 5 (2017) 5266–5272.

[29] S. Liu, J.K. Feng, X.F. Bian, J. Liu, Y.L. An, A controlled red phosphorus@Ni–P core@shell nanostructure as an ultralong cycle-life and superior high-rate anode for sodium-ion batteries, Energy Environ. Sci. 10 (2017) 1222–1233.

[30] J. Smajic, A. Alazmi, S.P. Patole, P.M.F.J. Costa, Single-walled carbon nanotubes as stabilizing agents in red phosphorus Li-ion battery anodes, RSC Adv. 7 (2017) 39997–40004.

[31] J. Sun, G.Y. Zheng, H.-W. Lee, N. Liu, H.T. Wang, H.B. Yao, W.S. Yang, Y. Cui, Formation of stable phosphorus-carbon bond for enhanced performance in black phosphorus nanoparticle-graphite composite battery anodes, Nano Lett. 14 (2014) 4573–4580.

[32] H.-S. Tsai, C.-C. Lai, C.-H. Hsiao, H. Medina, T.-Y. Su, H. Ouyang, T.-Hsiang Chen, J.-H. Liang, Y.-L. Chueh, Plasma-assisted synthesis of high-mobility atomically layered violet phosphorus, ACS Appl. Mater. Interfaces 7 (2015) 13723–13727.

[33] H.-S. Tsai, J.-H. Liang, Production and potential applications of elemental two-dimensional materials beyond graphene, ChemNanoMat 3 (2017) 604–613.

[34] W.-C. Chang, K.-W. Tseng, H.-Y. Tuan, Solution synthesis of iodine-doped red phosphorus nanoparticles for lithium-ion battery anodes, Nano Lett. 17 (2017) 1240–1247.

[35] J.F. Qian, D. Qiao, X.P. Ai, Y.L. Cao, H.X. Yang, Reversible 3-Li storage reactions of amorphous phosphorus as high capacity and cycling-stable anodes for Li-ion batteries, Chem. Commun. 48 (2012) 8931–8933.

[36] J.F. Qian, X.Y. Wu, Y.L. Cao, X.P. Ai, H.X. Yang, High capacity and rate capability of amorphous phosphorus for sodium ion batteries, Angew. Chem. Int. Ed. 52 (2013) 4633–4636.

[37] C. Marino, A. Debenedetti, B. Fraisse, F. Favier, L. Monconduit, Activated-phosphorus as new electrode material for Li-ion batteries, Electrochem. Commun. 13 (2011) 346–349.

[38] A.J. Bai, L. Wang, J.Y. Li, X.M. He, J.X. Wang, J.L. Wang, Composite of graphite/phosphorus as anode for lithium-ion batteries, J. Power Source 289 (2015) 100–104.

[39] Y.L. Wang, L.Y. Tian, Z.H. Yao, F. Li, S. Li, S.H. Ye, Enhanced reversibility of red phosphorus/active carbon composite as anode for lithium ion batteries, Electrochim. Acta 163 (2015) 71–76.

[40] T. Ramireddy, T. Xing, M.M. Rahman, Y. Chen, Q. Dutercq, D. Gunzelmann, A.M. Glushenkov, Phosphorus–carbon nanocomposite anodes for lithium-ion and sodium-ion batteries, J. Mater. Chem. A 3 (2015) 5572–5584.

[41] W.-J. Li, S.-L. Chou, J.-Z. Wang, H.-K. Liu, S.-X. Dou, Significant enhancement of the cycling performance and rate capability of the P/C composite via chemical bonding (P-C), J. Mater. Chem. A 4 (2016) 505–511.

[42] W.-J. Li, S.-L. Chou, J.-Z. Wang, H.-K. Liu, S.-X. Dou, Simply mixed commercial red phosphorus and carbon nanotube composite with exceptionally reversible sodium-ion storage, Nano Lett. 13 (2013) 5480–5484.

[43] Y.J. Zhu, Y. Wen, X.L. Fan, T. Gao, F.D. Han, C. Luo, S.C. Liou, C.S. Wang, Red phosphorus-single-walled carbon nanotube composite as a superior anode for sodium ion batteries, ACS Nano 9 (2015) 3254–3264.

[44] J.X. Song, Z.X. Yu, M.L. Gurdin, X.L. Li, H.S. Peng, D.H. Wang, Advanced sodium ion battery anode constructed via chemical bonding between phosphorus, carbon nanotube, and cross-linked polymer binder, ACS Nano 9 (2015) 11933–11941.

[45] G.L. Xu, Z.H. Chen, G.M. Zhong, Y.Z. Liu, Y. Yang, T.Y. Ma, Y. Ren, X.B. Zuo, X.-H. Wu, X.Y. Zhang, K. Amine, Nanostructured black phosphorus/ketjenblack–multiwalled carbon nanotubes composite as high performance anode material for sodium-ion batteries, Nano Lett. 16 (2016) 3955–3965.

[46] D. Yuan, J.L. Cheng, G.X. Qu, X.D. Li, W. Ni, B. Wang, H. Liu, Amorphous red phosphorous embedded in carbon nanotubes scaffold as promising anode materials for lithium-ion batteries, J. Power Source 301 (2016) 131–137.

[47] Z.W. Xu, Y. Zeng, L.Y. Wang, N. Li, C. Chen, C.Y. Li, J. Li, H.M. Lv, L.Y. Kuang, X. Tian, Nanoconfined phosphorus film coating on interconnected carbon nanotubes as ultrastable anodes for lithium ion batteries, J. Power Source 356 (2017) 18–26.

[48] W.H. Li, Z.Z. Yang, Y. Jiang, Z.R. Yu, L. Gu, Y. Yu, Crystalline red phosphorus incorporated with porous carbon nanofibers as flexible electrode for high performance lithium-ion batteries, Carbon 78 (2014) 455–462.

[49] B.Y. Ruan, J. Wang, D.Q. Shi, Y.F. Xu, S.L. Chou, H.K. Liu, J.Z. Wang, A phosphorus/N-doped carbon nanofiber composite as an anode material for sodium-ion batteries, J. Mater. Chem. A 3 (2015) 19011–19017.

[50] X. Zhou, Y.-X. Yin, L.-J. Wan, Y.-G. Guo, Facile synthesis of silicon nanoparticles inserted into graphene sheets as improved anode materials for lithium-ion batteries, Chem. Commun. 48 (2012) 2198–2200.

[51] X. Xin, X.F. Zhou, F. Wang, X.Y. Yao, X.X. Xu, Y.M. Zhu, Z.P. Liu, A 3D porous architecture of Si/graphene nanocomposite as high-performance anode materials for Li-ion batteries, J. Mater. Chem. 22 (2012) 7724–7730.

[52] J. Luo, X. Zhao, J. Wu, H.D. Jang, H.H. Kung, J. Huang, Crumpled graphene-encapsulated Si nanoparticles for lithium ion battery anodes, J. Phys. Chem. Lett. 3 (2012) 1824–1829.

[53] J.X. Song, Z.X. Yu, M.L. Gordin, S. Hu, R. Yi, D.H. Tang, T. Walter, M. Regula, D. Choi, X.L. Li, A. Manivannan, D.H. Wang, Chemically bonded phosphorus/graphene hybrid as a high performance anode for sodium-ion batteries, Nano Lett. 14 (2014) 6329–6335.

[54] L.K. Pei, Q. Zhao, C.C. Chen, J. Liang, J. Chen, Phosphorus nanoparticles encapsulated in graphene scrolls as a high-performance anode for sodium-ion batteries, ChemElectroChem 2 (2015) 1652–1655.

[55] C. Zhang, X. Wang, Q.F. Liang, X.Z. Liu, Q.H. Weng, J.W. Liu, Y.J. Yang, Z.H. Dai, K.J. Ding, Y. Bando, J. Tang, D. Golberg, Amorphous phosphorus/nitrogen-doped graphene paper for ultrastable sodium-ion batteries, Nano Lett. 16 (2016) 2054–2060.

[56] Y.H. Liu, A.Y. Zhang, C.F. Shen, Q.Z. Liu, X. Cao, Y.Q. Ma, L. Chen, C. Lao, T.C. Chen, F. Wei, C.W. Zhou, Red phosphorus nanodots on reduced graphene oxide as a flexible and ultra-fast anode for sodium-ion batteries, ACS Nano 11 (2017) 5530–5537.

[57] X.L. Ding, Y.Y. Huang, G.L. Li, Y. Tang, X.C. Li, Y.H. Huang, Phosphorus nanoparticles combined with cubic boron nitride and graphene as stable sodium-ion battery anodes, Electrochim. Acta 235 (2017) 150–157.

[58] G.H. Lee, M.R. Jo, K. Zhang, Y.M. Kang, A reduced graphene oxide-encapsulated phosphorus/carbon composite as a promising anode material for high-performance sodium-ion batteries, J. Mater. Chem. A 5 (2017) 3683–3690.

[59] J. Sun, H.-W. Lee, M. Pasta, H.T. Yuan, G.Y. Zheng, Y.M. Sun, Y.Z. Li, Y. Cui, A phosphorene-graphene hybrid material as a high-capacity anode for sodium-ion batteries, Nat. Nanotechnol. 10 (2015) 980–986.

[60] Y. Zhang, H.W. Wang, Z.Z. Luo, H.T. Tan, B. Li, S.N. Sun, Z. Li, Y. Zong, Z.C. Xu, Y.H. Yang, K.A. Khor, Q.Y. Yan, An air-stable densely packed phosphorene-graphene composite toward advanced lithium storage properties, Adv. Energy Mater. 6 (2016) 1600453.

[61] Z.X. Yu, J.X. Song, M.L. Gordin, R. Yi, D.H. Tang, D.H. Wang, Phosphorus-graphene nanosheet hybrids as lithium-ion anode with exceptional high-temperature cycling stability, Adv. Sci. 2 (2015) 1400020.

[62] L. Chen, G.M. Zhou, Z.B. Liu, X.M. Ma, J. Chen, Z.Y. Zhang, X.L. Ma, F. Li, H.M. Cheng, W.C. Ren, Scalable clean exfoliation of high-quality few-layer black phosphorus for a flexible lithium ion battery, Adv. Mater. 28 (2016) 510–517.

[63] Y.Y. Zhang, X.H. Rui, Y.X. Tang, Y.Q. Liu, J.Q. Wei, S. Chen, W.R. Leow, W.L. Li, Y.J. Liu, J.Y. Deng, B. Ma, Q.Y. Yan, X.D. Chen, Wet-chemical processing of phosphorus composite nanosheets for high-rate and High-capacity lithium-ion batteries, Adv. Energy Mater. (2016) 1502409.

[64] L. Pan, X.-D. Zhu, K.-N. Sun, Y.-T. Liu, X.-M. Xie, X.-Y. Ye, Molecular level distribution of black phosphorus quantum dots on nitrogen-doped graphene nanosheets for superior lithium storage, Nano Energy 30 (2016) 347–354.

[65] L. Wang, X.M. He, J.J. Li, W.T. Sun, J. Gao, J.W. Guo, C.Y. Jiang, Nano-structured phosphorus composite as high-capacity anode materials for lithium natteries, Angew. Chem. Int. Ed. 51 (2012) 9034–9037.

[66] W.H. Li, Z.Z. Yang, M.S. Li, Y. Jiang, X. Wei, X.W. Zhong, L. Gu, Y. Yu, Amorphous red phosphorus embedded in highly ordered mesoporous carbon with superior lithium and sodium storage capacity, Nano Lett. 16 (2016) 1546–1553.

[67] W.H. Li, S.H. Hu, X.Y. Luo, Z.L. Li, X.Z. Sun, M.S. Li, F.F. Liu, Y. Yu, Confined amorphous red phosphorus in MOF-derived N-doped microporous carbon as a superior anode for sodium-ion battery, Adv. Mater. (2017) 1605820.

[68] J. Sun, H.-W. Lee, M. Pasta, Y.M. Sun, W. Liu, Y.B. Li, H.R. Lee, N. Liu, Y. Cui, Carbothermic reduction synthesis of red phosphorus-filled 3D carbon material as a high-capacity anode for sodium ion batteries, Energy Storage Mater. 4 (2016) 130–136.

[69] C. Marino, L. Boulet, P. Gaveau, B. Fraisse, L. Monconduit, Nanoconfined phosphorus in mesoporous carbon as an electrode for Li-ion batteries: performance and mechanism, J. Mater. Chem. 22 (2012) 22713–22720.

[70] N. Wu, H.-R. Yao, Y.-X. Yin, Y.-G. Guo, Improving the electrochemical properties of the red P anode in Na-ion batteries via the space confinement of carbon nanopores, J. Mater. Chem. A 3 (2015) 24221–24225.

[71] a) W. Wei, S. Yang, H. Zhou, I. Lieberwirth, X. Feng, K. Müllen, 3D graphene foams cross-linked with pre-encapsulated Fe_3O_4 nanospheres for enhanced lithium storage, Adv. Mater. 25 (2013) 2909–2914;

b) Z.S. Wu, A. Winter, L. Chen, Y. Sun, A. Turchanin, X. Feng, K. Müllen, Three-dimensional nitrogen and boron co-doped graphene for high-performance all-solid-state supercapacitors, Adv. Mater. 24 (2012) 5130–5135;

c) Z.-S. Wu, S.B. Yang, Y. Sun, K. Parvez, X.L. Feng, K. Müllen, 3D nitrogen-doped graphene aerogel-supported Fe$_3$O$_4$ nanoparticles as efficient electrocatalysts for the oxygen reduction reaction, J. Am. Chem. Soc. 134 (2012) 9082–9085.

[72] M.A. Worsley, P.J. Pauzauskie, T.Y. Olson, J. Biener, J.H. Satcher, T.F. Baumann, Synthesis of graphene aerogel with high electrical conductivity, J. Am. Chem. Soc. 132 (2010) 14067–14069.

[73] a) J. Yuan, J. Zhu, H. Bi, X. Meng, S. Liang, L. Zhang, X. Wang, Graphene-based 3D composite hydrogel by anchoring Co$_3$O$_4$ nanoparticles with enhanced electrochemical properties, Phys. Chem. Chem. Phys. 15 (2013) 12940–12945;

b) Y. Huang, D. Wu, S. Han, S. Li, L. Xiao, F. Zhang, X. Feng, Assembly of tin oxide/graphene nanosheets into 3D hierarchical frameworks for high-performance lithium storage, ChemSusChem 6 (2013) 1510–1515.

[74] H. Gao, T.F. Zhou, Y. Zheng, Y.Q. Liu, J. Chen, H.K. Liu, Z.P. Guo, Integrated carbon/red phosphorus/graphene aerogel 3D architecture via advanced vapor-redistribution for high-energy sodium-on batteries, Adv. Energy Mater. (2016) 1601037.

[75] X.L. Fan, T. Gao, C. Luo, F. Wang, J.K. Hu, C.S. Wang, Superior reversible tin phosphide-carbon spheres for sodium ion battery anode, Nano Energy 38 (2017) 350–357.

[76] D.C.S. Souza, V. Pralong, A.J. Jacobson, L.F. Nazar, A reversible solid-state crystalline transformation in a metal phosphide induced by redox chemistry, Science 296 (2002) 2012–2015.

[77] S. Sim, J. Cho, Li reaction mechanism of MnP nanoparticles batteries and energy storage, J. Electrochem. Soc. 159 (2012) A669–A672.

[78] C.-M. Park, Y.-U. Kim, H.-J. Sohn, Topotactic Li insertion/extraction in hexagonal vanadium monophosphide, Chem. Mater. 21 (2009) 5566–5568.

[79] Y.-U. Kim, B.W. Cho, H.-J. Sohn, The reaction mechanism of lithium insertion in vanadium tetraphosphide: a possible anode material in lithium-ion batteries, J. Electrochem. Soc. 152 (2005) A1475–A1478.

[80] F. Gillot, M. Ménétrier, E. Bekaert, L. Dupont, M. Morcrette, L. Monconduit, J.M. Tarascon, Vanadium diphosphides as negative electrodes for secondary Li-ion batteries, J. Power Sources 172 (2007) 877–885.

[81] T.B. Massalski, Binary Alloy Phase Diagram, first ed. 2, American Society for Metals, 1989, p. 1828.

[82] JCPDS, File no. 42-1051.

[83] K.A. Kovnir, Y.V. Kolen'ko, S. Ray, J.W. Li, T. Watanabe, M. Itoh, M. Yoshimura, A.V. Shevelkov, A facile high-yield solvothermal route to tin phosphide Sn$_4$P$_3$, J. Solid State Chem. 179 (2006) 3756–3762.

[84] O. Olofsson, On the crystal structure of Sn$_4$P$_3$, Acta Chem. Scand. 21 (1967) 1659–1660.

[85] Y.U. Kim, C.K. Lee, H.J. Sohn, T. Kang, Reaction mechanism of tin phosphide anode by mechanochemical method for lithium secondary batteries, J. Electrochem. Soc. 151 (2004) A933–A937.

[86] Y.-U. Kim, S.-I. Lee, C.K. Lee, H.-J. Sohn, Enhancement of capacity and cycle-life of Sn$_{4+\delta}$P$_3$ ($0 \leq \delta \leq 1$) anode for lithium secondary batteries, J. Power Sources 141 (2005) 163–166.

[87] B. León, J.I. Corredor, J.L. Tirado, C. Pérez-Vicente, On the mechanism of the electrochemical reaction of tin phosphide with lithium, J. Electrochem. Soc. 153 (2006) A1829–A1834.

[88] J.-J. Wu, Z.-W. Fu, Pulsed-laser-deposited Sn$_4$P$_3$ electrodes for lithium-ion batteries and energy storage, J. Electrochem. Soc. 156 (2009) A22–A26.

[89] S.L. Liu, H.Z. Zhang, L.Q. Xu, L.B. Ma, X.X. Chen, Solvothermal preparation of tin phosphide as a long-life anode for advanced lithium and sodium ion batteries, J. Power Sources 304 (2016) 346–353.

[90] S.L. Liu, H.Z. Zhang, L.Q. Xu, L.B. Ma, Synthesis of hollow spherical tin phosphides (Sn$_4$P$_3$) and their high adsorptive and electrochemical performance, J. Cryst. Growth 438 (2016) 31–37.

[91] Y. Kim, Y. Kim, A. Choi, S. Woo, D. Mok, N.-S. Choi, Y.S. Jung, J.H. Ryu, S.M. Oh, K.T. Lee, Tin phosphide as a promising anode material for Na-ion batteries, Adv. Mater. 26 (2014) 4139–4144.

[92] J.F. Qian, Y. Xiong, Y.L. Cao, X.P. Ai, H.X. Yang, Synergistic Na-storage reactions in Sn$_4$P$_3$ as a high-capacity, cycle-stable anode of Na-ion batteries, Nano Lett. 14 (2014) 1865–1869.

[93] W.J. Li, S.-L. Chou, J.-Z. Wang, J.H. Kim, H.-K. Liu, S.-X. Dou, Sn$_{4+x}$P$_3$@ amorphous Sn-P composites as anodes for sodium-ion batteries with low cost, high capacity, long life, and superior rate capability, Adv. Mater. 26 (2014) 4037–4042.

[94] J. Liu, P. Kopold, C. Wu, P.A. Aken, J. Maier, Y. Yu, Uniform yolk-shell Sn$_4$P$_3$@C nanospheres as high-capacity and cycle-stable anode materials for sodium-ion batteries, Energy Environ. Sci. 8 (2015) 3531–3538.

[95] Q. Li, Z.Q. Li, Z.W. Zhang, C.X. Li, J.Y. Ma, C.X. Wang, X.L. Ge, S.H. Dong, L.W. Yin, Low-temperature solution-based phosphorization reaction route to Sn$_4$P$_3$/reduced graphene oxide nanohybrids as anodes for sodium ion batteries, Adv. Energy Mater. 6 (2016) 1600376.

[96] B.Y. Kim, H. Hwang, C.S. Yoon, M.G. Kim, J. Cho, Reversible lithium intercalation in teardrop-shaped ultrafine SnP$_{0.94}$ particles: an anode material for lithium-ion batteries, Adv. Mater. 19 (2007) 92–96.

[97] X.L. Fan, J.F. Mao, Y.J. Zhu, C. Luo, L.M. Suo, T. Gao, F.D. Han, S.-C. Liou, C.S. Wang, Superior stable self-healing SnP$_3$ anode for sodium-ion batteries, Adv. Energy Mater. (2015) 1500174.

[98] F. Gillot, S. Boyanov, L. Dupout, M.L. Doublet, M. Morcrette, L. Monconduit, J.M. Tarascon, Electrochemical reactivity and design of NiP$_2$ negative electrodes for secondary Li-ion natteries, Chem. Mater. 17 (2005) 6327–6337.

[99] P.L. Lou, Z.H. Cui, Z.Q. Jia, J.Y. Sun, Y.B. Tan, X.X. Guo, Monodispersed carbon-coated cubic NiP$_2$ nanoparticles anchored on carbon nanotubes as ultra-long-life anodes for reversible lithium storage, ACS Nano 11 (2017) 3705–3715.

[100] J. Fullenwarth, A. Darwiche, A. Soares, B. Donnadieu, L. Monconduit, NiP$_3$: a promising negative electrode for Li- and Na-ion batteries, J. Mater. Chem. A 2 (2014) 2050–2059.

[101] M. Cruz, J. Morales, L. Sánchez, J.S. Peña, F. Martín, Electrochemical properties of electrodeposited nicked phosphide thin films in lithium cells, J. Power Sources 171 (2007) 870–878.

[102] J.Y. Xiang, J.P. Tu, X.L. Wang, X.H. Huang, Y.F. Yuan, X.H. Xia, Z.Y. Zeng, Electrochemical performances of nanostructured Ni$_3$P–Ni films electrodeposited on nickel foam substrate, J. Power Sources 185 (2008) 519–525.

[103] J.Y. Xiang, X.L. Wang, J. Zhong, D. Zhang, J.P. Tu, Enhanced rate capability of multi-layered ordered porous nickel phosphide film as anode for lithium ion batteries, J. Power Sources 196 (2011) 379–385.

[104] Y. Lu, J.P. Tu, Q.Q. Xiong, Y.Q. Qiao, X.L. Wang, C.D. Gu, S.X. Mao, Synthesis of dinickel phosphide (Ni$_2$P) for fast lithium-ion transportation: a new class of nanowires with exceptionally improved electrochemical performance as a negative electrode, RSC Adv. 2 (2012) 3430–3436.

[105] Y. Lu, J.-P. Tu, Q.-Q. Xiong, H. Zhang, C.-D. Gu, X.-L. Wang, S.X. Mao, Large-scale synthesis of porous Ni$_2$P nanosheets for lithium secondary batteries, CrystEngComm 14 (2012) 8633–8641.

[106] Y.Y. Feng, H.J. Zhang, Y.P. Mu, W.X. Li, J.L. Sun, K. Wu, Y. Wang, Monodisperse sandwich-like coupled quasi-graphene sheets encapsulating Ni$_2$P nanoparticles for enhanced lithium-ion batteries, Chem. Eur. J. 21 (2015) 9229–9235.

[107] C. Wu, P. Kopold, P.A.V. Aken, J. Maier, Y. Yu, High performance graphene/Ni$_2$P hybrid anodes for lithium and sodium storage through 3D yolk-shell-like nanostructural design, Adv. Mater. 29 (2017) 1604015.

[108] Y.J. Bai, H.J. Zhang, X. Li, L. Liu, H.T. Xu, H.J. Qiu, Y. Wang, Novel peapod-like Ni$_2$P nanoparticles with improved electrochemical properties for hydrogen evolution and lithium storage, Nanoscale 7 (2015) 1446–1453.

[109] Y.J. Bai, H.J. Zhang, L. Fang, L. Liu, H.J. Qiu, Y. Wang, Novel peapod array of Ni$_2$P@graphitized carbon fiber composites growing on Ti substrate: a superior material for Li-ion batteries and the hydrogen evolution reaction, J. Mater. Chem. A 3 (2015) 5434–5441.

[110] Z.-Z. Luo, Y. Zhang, C.H. Zhang, H.T. Tan, Z. Li, A. Abutaha, X.-L. Wu, Q.H. Xiong, K.A. Khor, K. Hippalgaonkar, J.W. Xu, H.H. Hng, Q.Y. Yan, Multifunctional 0D-2D Ni$_2$P nanocrystals-black phosphorus heterostructure, Adv. Energy Mater. 7 (2017) 1601285.

[111] Y. Lu, J.P. Tu, J.Y. Xiang, J. Zhang, Y.J. Mai, S.X. Mao, Improved electrochemical performance of self-assembled hierarchical nanostructured nickel phosphide as a negative electrode for lithium ion batteries, J. Phys. Chem. C 115 (2011) 23760–23767.

[112] S. Carenco, C. Surcin, M. Morcrette, D. Larcher, N. Mézailles, C. Boissière, C. Sanchez, Improving the Li-electrochemical properties of monodisperse Ni$_2$P nanoparticles by self-generated carbon coating, Chem. Mater. 24 (2012) 688–697.

[113] Y. Lu, X. Ge, X.Y. Zhao, T.Q. Wang, S. Huang, C.D. Gu, J.P. Tu, S.X. Mao, Graphene-wrapped Ni$_2$P materials: a 3D porous architecture with improved electrochemical performance, J. Solid State Electrochem. 18 (2014) 2245–2253.

[114] Y. Lu, X.L. Wang, Y.J. Mai, J.Y. Xiang, H. Zhang, L. Li, C.D. Gu, J.P. Tu, S.X. Mao, Ni$_2$P/graphene sheets as anode materials with enhanced electrochemical properties versus lithium, J. Phys. Chem. C 116 (2012) 22217–22225.

[115] W.M. Du, S.H. Wei, K.K. Zhou, J.J. Guo, H. Pang, X.F. Qian, One-step synthesis and graphene-modification to achieve nickel phosphide nanoparticles with electrochemical properties suitable for supercapacitors, Mater. Res. Bull. 61 (2015) 333–339.

[116] Y. Lu, J.P. Tu, Q.Q. Xiong, Y.Q. Qiao, J. Zhang, C.D. Gu, X.L. Wang, S.X. Mao, Carbon-decorated single-crystalline Ni$_2$P nanotubes derived from Ni nanowire templates: a high-performance material for Li-ion batteries, Chem. Eur. J. 18 (2012) 6031–6038.

[117] Y. Lu, J.-P. Tu, Q.-Q. Xiong, J.-Y. Xiang, Y.-J. Mai, J. Zhang, Y.-Q. Qiao, X.-L. Wang, C.-D. Gu, S.X. Mao, Controllable synthesis of a monophase nickel phosphide/carbon (Ni$_5$P$_4$/C) composite electrode via wet-chemistry and a solid-state reaction for the anode in lithium secondary batteries, Adv. Funct. Mater. 22 (2012) 3927–3935.

[118] J. Jiang, C. Wang, W. Li, Q. Yang, One-pot synthesis of carbon-coated Ni$_5$P$_4$ nanoparticles and CoP nanorods for high-rate and high-stability lithium-ion batteries, J. Mater. Chem. A 3 (2015) 23345–23351.

[119] C.D. Wang, T. Ding, Y. Sun, X.L. Zhou, Y. Liu, Q. Yang, Ni$_{12}$P$_5$ nanoparticles decorated on carbon nanotubes with enhanced electrocatalytic and lithium storage properties, Nanoscale 7 (2015) 19241–19249.

[120] H.J. Zhang, Y.Y. Feng, Y. Zhang, L. Fang, W.X. Li, Q. Liu, K. Wu, Y. Wang, Peapod-like Composite with nickel phosphide nanoparticles encapsulated in carbon fibers as enhanced anode for Li-ion batteries, ChemSusChem 7 (2014) 2000–2006.

[121] H. Zhang, Y. Lu, C.-D. Gu, X.-L. Wang, J.-P. Tu, Ionothermal synthesis and lithium storage performance of core/shell structured amorphous@crystalline Ni–P nanoparticles, CrytEngComm 14 (2012) 7942–7950.

[122] M.E. Schlesinger, The thermodynamic properties of phosphorus and solid binary phosphides, Chem. Rev. 102 (2002) 4267–4302.

[123] H. Pfeiffer, F. Tancret, M.-P. Bochat, L. Monconduit, F. Favier, T. Brousse, Air stable copper phosphide (Cu$_3$P): a possible negative electrode material for lithium batteries, Electrochem. 6 (2004) 263–267.

[124] M.-P. Bichat, T. Politova, H. Pfeiffer, F. Tancret, L. Monconduit, J.-L. Pascal, T. Brousse, F. Favier, Cu$_3$P as anode material for lithium ion battery: powder morphology and electrochemical performances, J. Power Sources 136 (2004) 80–87.

[125] B. Mauvernay, M.-L. Doublet, L. Monconduit, Redox mechanism in the binary transition metal phosphide Cu$_3$P, J. Phys. Chem. Solids 67 (2006) 1252–1257.

[126] F. Poli, A. Wong, J.W. Kshetrimayum, L. Monconduit, M. Letellier, In situ NMR insights into the electrochemical reaction of Cu$_3$P electrodes in lithium Batteries, Chem. Mater. 28 (2016) 1787–1793.

[127] M.S. Chandrasekar, S. Mitra, Thin copper phosphide films as conversion anode for lithium-ion battery applications, Electrochim. Acta 92 (2013) 47–54.

[128] H. Pfeiffer, F. Tancret, T. Brousse, Synthesis, characterization and electrochemical properties of copper phosphide (Cu$_3$P) thick films prepared by solid-state reaction at low temperature: a probable anode for lithium ion batteries, Electrochim. Acta 50 (2005) 4763–4770.

[129] S.L. Liu, S. Li, J.P. Wang, Q.Q. Shi, M.M. Li, Surfactant-assisted synthesis and electrochemical performances of Cu$_3$P dendrites, Mater. Res. Bull. 47 (2012) 3352–3356.

[130] M.P. Fan, Y. Chen, Y.H. Xie, T.Z. Yang, X.W. Shen, N. Xu, H.Y. Yu, C.L. Yan, Half-cell and full-cell applications of highly stable and binder-free sodium ion batteries based on Cu$_3$P nanowire anodes, Adv. Funct. Mater. 26 (2016) 5019–5027.

[131] C. Villevieille, F. Robert, P.L. Taberna, L. Bazin, P. Simon, L. Monconduit, The good reactivity of lithium with nanostructured copper phosphide, J. Mater. Chem. 18 (2008) 5956–5960.

[132] S.B. Ni, J.J. Ma, X.H. Lv, X.L. Yang, L.L. Zhang, The fine electrochemical performance of porous Cu$_3$P/Cu and the high energy density of Cu$_3$P as anode for Li-ion batteries, J. Mater. Chem. A 2 (2014) 20506–20509.

[133] M.C. Stan, R. Klöpsch, A. Bhaskar, J. Li, S. Passerini, M. Winter, Cu$_3$P binary phosphide: synthesis via a wet mechanochemical method and electrochemical behavior as negative electrode material for lithium-ion batteries, Adv. Energy Mater. 3 (2013) 231–238.

[134] S.L. Liu, X.D. He, J.P. Zhu, L.Q. Xu, J.B. Tong, Cu$_3$P RGO nanocomposite as a new anode for lithium-ion batteries, Sci. Rep. 6 (2016) 35189.

[135] A.J. Zhou, B. Yang, W.H. Wang, X.Y. Dai, M.J. Zhao, J. Xue, M.G. Han, C. Fan, J.Z. Li, Enhanced reversibility and electrochemical performances of mechanically alloyed Cu$_3$P achieved by Fe addition, RSC Adv. 6 (2016) 26800–26808.

[136] K. Wang, J. Yang, J.Y. Xie, B.F. Wang, Z.S. Wen, Electrochemical reactions of lithium with CuP$_2$ and Li$_{1.75}$Cu$_{1.25}$P$_2$ synthesized by ball milling, Electrochem. Commun. 5 (2003) 480–483.

[137] G.-A. Li, C.-Y. Wang, W.-C. Chang, H.-Y. Tuan, Phosphorus-rich copper phosphide nanowires for field-effect transistors and lithium-ion batteries, ACS Nano 10 (2016) 8632–8644.

[138] F.P. Zhao, N. Han, W.J. Huang, J.J. Li, H.L. Ye, F.J. Chen, Y.G. Li, Nanostructured CuP$_2$/C composites as high-performance anode materials for sodium ion batteries, J. Mater. Chem. A 3 (2015) 21754–21759.

[139] S.-O. Kim, A. Manthiram, The facile synthesis and enhanced sodium-storage performance of a chemically bonded CuP$_2$/C hybrid anode, Chem. Commun. 52 (2016) 4337–4340.

[140] S.-O. Kim, A. Manthiram, Phosphorus-rich CuP$_2$ embedded in carbon matrix as a high-performance anode for lithium-ion batteries, ACS Appl. Mater. Interfaces 9 (2017) 16221–16227.

[141] M.E. Schlesinger, Cheminform 34 (2003) (4267-4231).

[142] D.C.C. Silva, O. Crosnier, G. Ouvrard, J. Greedan, A.S. Sefat, L.F. Nazar, Reversible lithium uptake by FeP$_2$, Electrochem. Solid-State Lett. 6 (2003) A162–A165.

[143] S. Boyanov, J. Bernardi, F. Gillot, L. Dupont, M. Womes, J.-M. Tarascon, L. Monconduit, M.- L. Doublet, FeP: another attractive anode for the Li-ion battery enlisting a reversible two-step insertion/conversion process, Chem. Mater. 18 (2006) 3531–3538.

[144] S. Boyanov, D. Zitoun, M. Ménétrier, J.C. Jumas, M. Womes, L. Monconduit, Comparison of the electrochemical lithiation/delitiation mechanisms of FeP$_x$ (x = 1, 2, 4) based electrodes in Li-ion batteries, J. Phys. Chem. C 113 (2009) 21441–21452.

[145] J.W. Hall, N. Membreno, J. Wu, H. Celio, R.A. Jones, K.J. Stevenson, Low-temperature synthesis of amorphous FeP$_2$ and its use as anodes for Li ion batteries, J. Am. Chem. Soc. 134 (2012) 5532–5535.

[146] J. Jiang, W.L. Wang, C.D. Wang, L. Zhang, K.B. Tang, J. Zuo, Q. Yang, Electrochemical performance of iron diphosphide/carbon tube nanohybrids in lithium-ion batteries, Electrochim. Acta 170 (2015) 140–145.

[147] Q.-R. Yang, W.-J. Li, S.-L. Chou, J.-Z. Wang, H.-K. Liu, Ball-milled FeP/graphite as a low-cost anode material for the sodium-ion battery, RSC Adv. 5 (2015) 80536–80541.

[148] F. Han, C.Z. Zhang, J.X. Yang, G.Z. Ma, K.J. He, X.K. Li, Well-dispersed and porous FeP@C nanoplates with stable and ultrafast lithium storage performance through conversion reaction mechanism, J. Mater. Chem. A 4 (2016) 12781–12789.

[149] J. Jiang, W.L. Wang, J.W. Liang, J. Zuo, Q. Yang, Synthesis of nanorod-FeP@C composites with hysteretic lithiation in lithium-ion batteries, Dolton Trans. 44 (2015) 10297–10303.

[150] J. Yang, Y. Ouyang, H.J. Zhang, H.T. Xu, Y. Zhang, Y. Wang, Novel Fe$_2$P/ graphitized carbon yolk/shell octahedra for high-efficiency hydrogen production and lithium storage, J. Mater. Chem. A 4 (2016) 9923–9930.

[151] M.S. Chandrasekar, S. Mitra, Electrodeposition of iron phosphide on copper substrate as conversion negative electrode for lithium-ion battery application, Ionics 20 (2014) 137–140.

[152] I.-T. Park, H.-C. Shin, Amorphous FeP$_y$ (0.1 < y < 0.7) thin film anode for rechargeable lithium battery, Electrochem. Commun. 33 (2013) 102–106.

[153] G.X. Wang, R.B. Zhang, T.C. Jiang, N.A. Chernova, Z.X. Dong, M.S. Whittingham, Facile synthesis and electrochemical performance of the nanoscaled FePy anode, J. Power Sources 270 (2014) 248–256.

[154] Y. Zhang, H.J. Zhang, Y.Y. Feng, L. Liu, Y. Wang, Unique Fe$_2$P nanoparticles enveloped in sandwichlike graphited carbon sheets as excellent hydrogen evolution reaction catalyst and lithium-ion battery anode, ACS Appl. Mater. Interfaces 7 (2015) 26684–26690.

[155] W.-J. Li, S.-L. Chou, J.-Z. Wang, H.-K. Liu, S.-X. Dou, A new, cheap, and productive FeP anode material for sodium-ion batteries, Chem. Commun. 51 (2015) 3682–3685.

[156] F. Han, C.Y.J. Tan, Z. Gao, Improving the specific capacity and cyclability of sodium-ion batteries by engineering a dual-carbon phase-modified amorphous and mesoporous iron phosphide, ChemElectroChem **3** (2016) 1054–1062.

[157] Z. Yang, L. Liu, X. Wang, S. Yang, X. Su, Stability and electronic structure of the Co-P compounds from first-principle calculations, J. Alloy. Compd. 509 (2011) 165–171.

[158] R. Alcántaraa, J.L. Tiradoa, J.C. Jumasb, L. Monconduitb, J. Olivier-Fourcade, Electrochemical reaction of lithium with CoP$_3$, J. Power Sources 109 (2002) 308–312.

[159] V. Pralong, D.C.S. Souza, K.T. Leung, L.F. Nazar, Reversible lithium uptake by CoP$_3$ at low potential: role of the anion, Electrochem. Commun. 4 (2002) 516–520.

[160] Z.H. Zhang, J. Yang, Y. Nuli, B.F. Wang, J.Q. Xu, CoP$_x$ synthesis and lithiation by ball-milling for anode materials of lithium ion cells, Solid State Ion. 176 (2005) 693–697.

[161] Y.-H. Cui, M.-Z. Xue, Z.-W. Fu, X.-L. Wang, X.-J. Liu, Nanocrystalline CoP thin film as a new anode material for lithium ion battery, J. Alloy. Compd. 555 (2013) 283–290.

[162] M.C. López, G.F. Ortiz, J.L. Tirado, A functionalized Co$_2$P negative electrode for batteries demanding high Li-potential reaction, J. Electrochem. Soc. 159 (2012) A1253–A1261.

[163] D. Yang, J.X. Zhu, X.H. Rui, H.T. Tan, R. Cai, H.E. Hoster, D.Y.W. Yu, H.H. Hng, Q.Y. Yan, Synthesis of cobalt phosphides and their application as anodes for lithium ion batteries, ACS Appl. Mater. Interfaces 5 (2013) 1093–1099.

[164] X.J. Xu, J. Liu, R.Z. Hu, J.W. Liu, L.Z. Ouyang, M. Zhu, Self-supported CoP nanorod arrays grafted on stainless steel as an advanced integrated anode for stable and long-life lithium-ion batteries, Chem. Eur. J. 23 (2017) 5198–5204.

[165] B. Wang, Q. Ru, Q. Guo, X.Q. Chen, Z. Wang, X.H. Hou, S.J. Hu, Fabrication of one-dimensional mesoporous CoP nanorods as anode materials for lithium-ion batteries, Eur. J. Inorg. Chem. (2017) 3729–3735.

[166] J. Yang, Y. Zhang, C.C. Sun, H.Z. Liu, L.Q. Liu, W.L. Si, W. Huang, Q.Y. Yan, X.C. Dong, Graphene and cobalt phosphide nanowire composite as an anode material for high performance lithium-ion batteries, Nano Res. 9 (2016) 612–621.

[167] K.J. Zhu, J. Liu, S. Li, L.L. Liu, L.Y. Yang, S.L. Liu, H. Wang, T. Xie, Ultrafine cobalt phosphide nanoparticles embedded in nitrogen-doped carbon matrix as a superior anode material for lithium ion batteries, Adv. Mater. Interfaces (2017) 1700377.

[168] Q.H. Xie, D.Q. Zeng, P.Y. Gong, J. Huang, Y.T. Ma, L.S. Wang, D.-L. Peng, One-pot fabrication of graphene sheets decorated Co$_2$P-Co hollow nanospheres for advanced lithium ion battery anodes, Electrochim. Acta. 232 (2017) 465–473.

[169] W.-J. Li, Q.-R. Yang, S.-L. Chou, J.-Z. Wang, H.-K. Liu, Cobalt phosphide as a new anode material for sodium storage, J. Power Source 294 (2015) 627–632.

[170] X.L. Ge, Z.Q. Li, L.W. Yin, Metal-organic frameworks derived porous core/ shellCoP@C polyhedrons anchored on 3D reduced graphene oxide networks as anode for sodium-ion battery, Nano Energy 32 (2017) 117–124.

[171] M.-P. Bichat, J.-L. Pascal, F. Gillot, F. Favier, Electrochemical lithium insertion in Zn$_3$P$_2$ zinc phosphide, Chem. Mater. 17 (2005) 6761–6771.

[172] M.P. Bichat, L. Monconduit, J.L. Pascal, F. Favier, Anode materials for lithium ion batteries in the Li-Zn-P system, Ionics 11 (2005) 66–75.

[173] M.V.V.M. Satya Kishore, U.V. Varadaraju, Electrochemical reaction of lithium with Zn$_3$P$_2$, J. Power Sources 144 (2005) 204–207.

[174] H. Hwang, M.G. Kim, Y. Kim, S.W. Martin, J. Cho, The electrochemical lithium reactions of monoclinic ZnP$_2$ material, J. Mater. Chem. 17 (2007) 3161–3166.

[175] C.-M. Park, H.-J. Sohn, Tetragonal zinc diphosphide and its nanocomposite as an anode for lithium secondary batteries, Chem. Mater. 20 (2008) 6319–6324.

[176] W.W. Li, H.Q. Li, Z.J. Lu, L. Gan, L.B. Ke, T.Y. Zhai, H.S. Zhou, Layered phosphorus-like GeP$_5$: a promising anode candidate with high initial coulombic efficiency and large capacity for lithium ion batteries, Energy Environ. Sci. 8 (2015) 3629–3636.

[177] W.W. Li, L.B. Ke, Y.Q. Wei, S.H. Guo, L. Gan, H.Q. Li, T.Y. Zhai, H.S. Zhou, Highly reversible sodium storage in a GeP$_5$/C composite anode with large capacity and low voltage, J. Mater. Chem. A 5 (2017) 4413–4420.

[178] W. Qi, H.H. Zhao, Y. Wu, H. Zeng, T. Tao, C. Chen, C.J. Kuang, S.X. Zhou, Y.H. Huang, Facile synthesis of layer structured GeP$_3$/C with stable chemical bonding for enhanced lithium-ion storage, Sci. Rep. 7 (2017) 43582.

[179] M.G. Kim, S.H. Lee, J.P. Cho, Highly reversible Li-ion intercalating MoP$_2$ nanoparticle cluster anode for lithium rechargeable batteries, J. Electrochem. Soc. 156 (2009) A89–A94.

[180] Z.D. Huang, H.S. Hou, C. Wang, S.M. Li, Y. Zhang, X.B. Ji, Molybdenum phosphide: a conversion-type anode for ultralong-life sodium-ion batteries, Chem. Mater. 29 (2017) 7313–7322.

[181] G. Park, S. Sim, J. Lee, S.-M. Lee, Effect of silicon doping on the electrochemical properties of MoP$_2$ nano-cluster anode for lithium ion, J. Alloy. Compd. 639 (2015) 296–300.

[182] X. Wang, P.P. Sun, J.W. Qin, J.Q. Wang, Y. Xiao, M.H. Cao, A three-dimensional porous MoP@C hybrid as a high-capacity, long-cycle life anode material for lithium-ion batteries, Nanoscale 8 (2016) 10330–10338.

[183] D. Duveau, S. Sananes Israel, J. Fullenwarth, F. Cuninc, L. Monconduit, Pioneer study of SiP$_2$ as negative electrode for Li- and Na-ion batteries, J. Mater. Chem. A

4 (2016) 3228–3232.

[184] Y.Y. Lu, P.F. Zhou, K.X. Lei, Q. Zhao, Z.L. Tao, J. Chen, Selenium phosphide (Se₄P₄) as a new and promising anode material for sodium-ion batteries, Adv. Energy Mater. (2017) 1601973.

[185] H. Hwang, M.G. Kim, J. Cho, Li reaction behavior of GaP nanoparticles prepared by a sodium naphthalenide reduction method, J. Phys. Chem. C 111 (2007) 1186–1193.

[186] Y.-H. Cui, M.-Z. Xue, Xi-L. Wang, K. Hu, Z.-W. Fu, InP as new anode material for lithium ion batteries, Electrochem. Commun. 11 (2009) 1045–1047.

[187] M.-D. Gerngross, E.Q. González, J. Carstensen, H. Föll, Single-crystalline porous indium phosphide as anode material for Li-ion batteries, J. Electrochem. Soc. 159 (2012) A1941–A1948.

[188] M.D. Gerngross, E.Q. González, J. Carstensen, H. Föll, Characterization of three-dimensional single-crystalline porous InP anodes for Li-ion batteries, ECS Trans. 50 (2013) 139–150.

[189] Z.Q. Li, L.Y. Zhang, X.L. Ge, C.X. Li, S.H. Dong, C.X. Wang, L.W. Yin, Core-shell structured CoP/FeP porous microcubes interconnected by reduced graphene oxide as high performance anodes for sodium ion batteries, Nano Energy 32 (2017) 494–502.

[190] J.B. Zhou, X.Y. Liu, W.L. Cai, Y.C. Zhu, J.W. Liang, K.L. Zhang, Y. Lan, Z.H. Jiang, G.M. Wang, Y.T. Qian, Wet-chemical synthesis of hollow red-phosphorus nanospheres with porous shells as Anodes for high performance lithium-ion and sodium-ion batteries, Adv. Mater. (2017) 1700214.

[191] S. Boyanov, F. Gillot, L. Monconduit, The electrochemical reactivity of the NiP₃ skutterudite-type phase with lithium, Ionics 14 (2008) 125–130.